REPORT DOCUMENTATION PAGE

1a. REPORT SECURITY CLASSIFICATION Unclassified	1b. RESTRICTIVE MARKINGS

DTIC ELECTE JUL 2 0 1989 D

AD-A210 366

2a. SECURITY CLASSIFICATION AUTHORITY	3. DISTRIBUTION/AVAILABILITY OF REPORT
	Approved for public release; distribution unlimited.

5. MONITORING ORGANIZATION REPORT NUMBER(S)
AFOSR-TR. 89-0995

6a. NAME OF PERFORMING ORGANIZATION CeramPhysics, Inc.	6b. OFFICE SYMBOL (If applicable)	7a. NAME OF MONITORING ORGANIZATION AFOSR

6c. ADDRESS (City, State, and ZIP Code) 921 Eastwind Dr., Suite 110 Westerville, OH 43081	7b. ADDRESS (City, State, and ZIP Code) Building 410 Bolling AFB, DC 20332-6448

8a. NAME OF FUNDING/SPONSORING ORGANIZATION AFOSR	8b. OFFICE SYMBOL (If applicable)	9. PROCUREMENT INSTRUMENT IDENTIFICATION NUMBER F49620-86-C-0029

8c. ADDRESS (City, State, and ZIP Code) Building 410 Bolling AFB, DC 20332-6448	10. SOURCE OF FUNDING NUMBERS			

	PROGRAM ELEMENT NO.	PROJECT NO.	TASK NO.	WORK UNIT ACCESSION NO.
	61102F	2305	A1	

11. TITLE (Include Security Classification)

Capacitive Energy Storage at Cryogenic Temperatures

12. PERSONAL AUTHOR(S) C.F. Clark

13a. TYPE OF REPORT Final	13b. TIME COVERED FROM 1/1/86 TO 12/31/88	14. DATE OF REPORT (Year, Month, Day) 1989, Feb. 14	15. PAGE COUNT 145

16. SUPPLEMENTARY NOTATION

17.	COSATI CODES		18. SUBJECT TERMS (Continue on reverse if necessary and identify by block number)
FIELD	GROUP	SUB-GROUP	

19. ABSTRACT (Continue on reverse if necessary and identify by block number)

Ceramic multilayer capacitors have been developed with large dielectric constants, (8000 at zero field) and large breakdown strengths at 77 K for use in capacitive energy storage. Energy storage densities as large as 5.8 J/cm^3 (=95 J/in^3=0.89 J/gm) have been achieved. A bank of ten capacitors has withstood over 100,000 duty cycles at 77 K of a slow 3-sec charge to 400 volts and then a rapid discharge. The emphasis in this research has been on optimizing processing parameters to improve breakdown strength. These processing paramenters have been quantified to the extent that large numbers of reliable, uniform capacitors can be produced.

20. DISTRIBUTION/AVAILABILITY OF ABSTRACT ☒ UNCLASSIFIED/UNLIMITED ☐ SAME AS RPT. ☐ DTIC USERS	21. ABSTRACT SECURITY CLASSIFICATION UNCLASSIFIED
22a. NAME OF RESPONSIBLE INDIVIDUAL B.L. Smith	22b. TELEPHONE (Include Area Code) 202/767/4908	22c. OFFICE SYMBOL NP
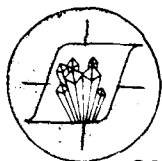
DD FORM 1473, 84 MAR   83 APR edition may be used until exhausted.
All other editions are obsolete.

Final Technical Report

AFOSR SBIR Phase II Contract

F49620-86-C-0029

Capacitive Energy Storage
at Cryogenic Temperatures

by

C. F. Clark C7C
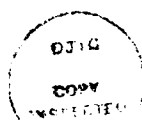CeramPhysics, Inc.
Westerville, OH 43081

February 14, 1989

Table of Contents

I. SUMMARY

The primary goal of this Phase II program was to improve
the dielectric breakdown strength of ceramic multilayer
capacitors (MLC's) in order to improve capacitive energy storage
at liquid-nitrogen temperatures. A secondary goal was to explore
the reproducibility of a field-enforced state-switching effect
discovered in the Phase I program. The ceramic composition
involved in these programs is designated as CPN17 and has a
dielectric constant in the range 8,000-10,000 at 77 K.

Several variations in conventional ceramic-processing
parameters were studied, leading to systematic improvements in
the breakdown strength at 77 K (160 to 250 to 400 kV/cm).
Individual energy-storage values of 5.8 J/cm^3 at 77 K have been
experimentally achieved in these MLC's (= 95 J/in^3 = 0 89 J/g).

A storage bank of 10 MLC's was duty-cycled to 10^5 cycles at
77 K (3 s charge time to 400 V followed by instantaneous
discharge), and no failures were observed under these conditions.
Energy losses during cycling were immeasurably small (monitored
by measuring the nitrogen boil-off rate), and no changes in the
average temperature of the bank during cycling were measured. An
interesting electrocaloric effect in CPN17 was measured during
cycling.

The thermal properties of the CPN17 MLC were thoroughly
characterized at low temperatures, including measurements of both
the transverse and longitudinal thermal conductances and the
transient heat flow at the MLC-nitrogen interface. These data
were used in finite-element-analyses of the thermal balances
between the MLC and the nitrogen bath during cycling.

The state-switching effect seen in the Phase I program could
not be duplicated in this Phase II program.

A number of ceramic-processing parameters have been
identified which affect the dielectric breakdown strength at 77
K, and these parameters have been optimized to the extent
possible. However, it is clear that a point of diminishing
returns has been reached, and further advances in this technology

will come from a radical departure from conventional processing. Modern processing which involves ultrafine monosized powders coupled with rate-controlled-sintering technology is recommended.

II. Background and Review of Phase I

Storing energy in capacitor banks at room temperature is commonly used in applications where size or weight has not been a major concern. However, capacitive energy storage at cryogenic temperatures offers considerable advantages: (1) Dielectric breakdown strengths in ceramic capacitors are enhanced; (2) Deleterious effects due to electronic conduction and/or aging in ferroelectric ceramics may be frozen out; (3) Electrical resistivities of metal components are decreased by an order of magnitude compared to room temperature; and (4) A judicious choice of ceramic compositions can lead to electrocaloric cooling effects on discharge (E → O) which can partially offset irreversible heating effects. Finally, both liquid nitrogen (77.4 K) and liquid oxygen (90.2 K) are inexpensive cryogens with large latent heats, and the latter cryogen is available on spacecraft.

There are few published studies of capacitive energy storage at cryogenic temperatures. A General Electric study[1] in the late 60's reported energy densities $\approx$ 0.6 J/cm^3 at 77 K, and a Corning Glass Works study[2] reported densities up to ~ 5 J/cm^3 at 77 K.

From basic research at CeramPhysics in the cadmium-lead-niobate-tantalate family of ferroelectric ceramics, a composition range was discovered which has a very large maximum in the dielectric constant ($\approx$ 8000) at liquid-nitrogen temperatures, and the paraelectric → ferroelectric transition temperature can be compositionally varied from 50 to 150 K. Early estimates of the energy density values possible with these ceramics suggested 20 - 25 J/cm^3, and these materials sinter in a range favorable for making multilayer capacitors (MLC's) using state-of-the-art, tape-casting manufacturing methods.

A Phase I, SBIR program at CeramPhysics was funded by the Air Force Office of Scientific Research at Bolling AFB to pursue solid-state research on these ceramics aimed at capacitive energy storage at cryogenic temperatures.[3] The results of this program are summarized below.

A ceramic composition was selected (so-called CPN17) which had a maximum at 71 K in the zero-field dielectric constant (ε_o), as shown in Fig. II-1, and this insured that the material was in the cubic pyrochlore phase at 77 K.

Prototype MLC's of CPN17 were fabricated for testing at cryogenic temperatures. These MLC's were approximately $1 \times 1 \times 0.2$ cm^3 devices containing 46 active dielectric layers with Pt/Pd/Au embedded electrodes. The dielectric efficiency of these MLC's was $\simeq$ 60%, and two batches of MLC's were fabricated. The first batch had fired dielectric thicknesses of 45 μm (1.75 mil), and the second, minor batch, 28 μm (1.10 mil). The purpose of making a second batch of prototype MLC's was to examine briefly if the dielectric breakdown strength could be improved by starting with finer particle size ceramic powders.

These relatively small, ceramic MLC's had capacitances $\simeq$ 4.3 μF at 77 K, and this necessitated a range-extension of the General Radio Bridge. In addition, a bridge-protection circuit was built for making high-voltage measurements.
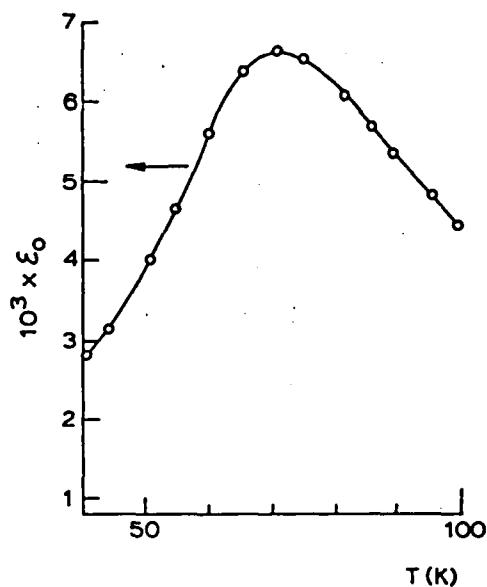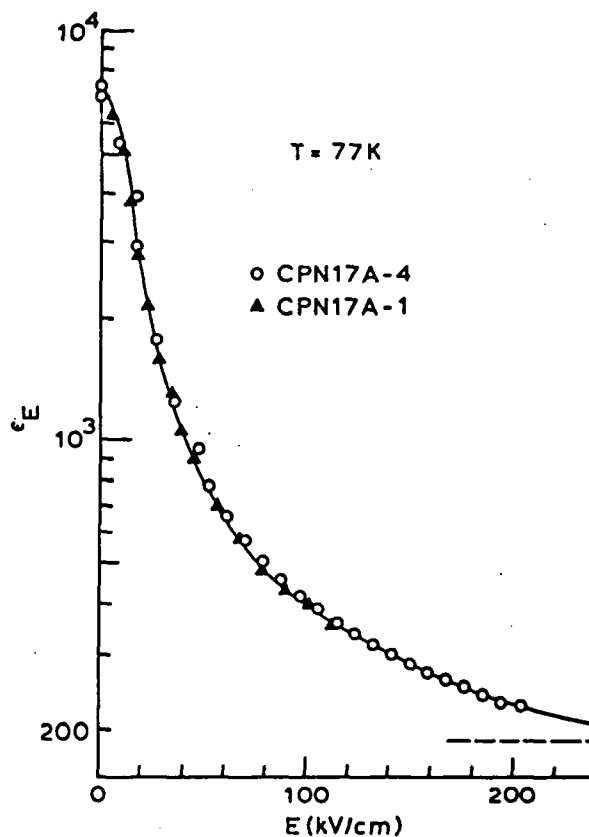
Figure II-1. Dielectric constant data for CPN17.

Figure II-2 Field-dependent tric data at 77 K.

Examples of ε_E-data measured on MLC's from the first batch are shown in Fig. II-2. Not only is there excellent reproducibility, but it was consistently found that ε_O repeats very well after E-field cycling -- i.e., hysteretic effects are <u>absent</u> in CPN17. The average breakdown strength of the first batch of prototype MLC's was ~ 150 kV/cm (380 V/mil) at 77 K, a value disappointingly low.

Measurements on the second batch of MLC's revealed an improved breakdown strength, avg. ~ 260 kV/cm (660 V/mil), and ε_E-data were measured on these MLC's. Here, one MLC withstood 3000 V (1074 kV/cm), and the ε_E-data up to this very large field strength are shown in Fig. II-3. An unusual behavior is seen: ε_E drops with E to point A, but at a field E $\simeq$ 300 kV/cm ε_E "jumps" onto the curve B-C and appears stable. On decreasing the field from point C to E = 0, ε_O repeats very well, indicating the absence of hysteretic effects. The value of ε_O in Fig. II-3 (~ 3600) is smaller than ε_O in Fig. II-2, and this may be due to the finer grain size in the second batch of MLC's.

Several attempts were made to reproduce the data in Fig. II-3, but all the MLC's failed before the "switch" field, E $\simeq$ 300 kV/cm, could be achieved (including the MLC in Fig. II-3 upon re-measuring). However, all these measured data repeated the curve up to point A very well.

A 3 µF capacitor from Maxwell Laboratories was measured on the system up to 3000 V, and there were no anomalies in the measured capacitance data (note from Fig. II-3 that the capacitance of the
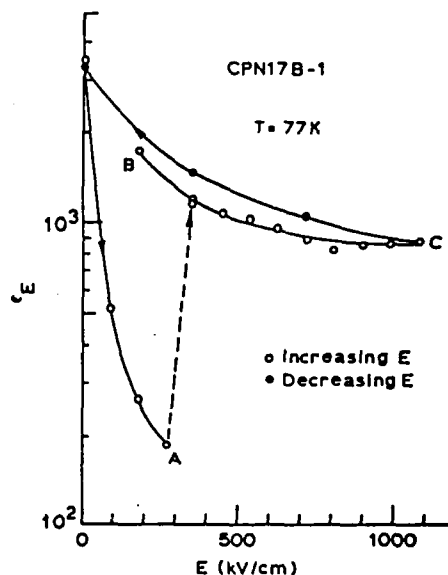

Figure II-3. Field-dependent dielectric data at 77 K up to 1074 kV/cm.

MLC jumps by an order of magnitude above 300 kV/cm). It was concluded that the effect in Fig. II-3 is real and is due to a field-enforced switching of the CPN17 into another, highly-polarizable state that is non-hysteretic.

Stored-energy densities at 77 K were calculated according to the Helmholtz density for reversible ε_E-behavior,

$$\Delta F = \frac{1}{8\pi} \int_0^{E_C} \varepsilon dE^2, \qquad (II-1)$$

where E_C is an upper field strength. Two approaches were taken: (1) The ε_E-data in Fig. II-2 for the first-batch MLC's appear to saturate at $\simeq 200$, as shown by the dashed line; therefore, these data were integrated numerically according to Eq. (II-1) up to 200 kV/cm, above which ε_E was set equal to 195; and (2) The "induced-state" ε_E-data in Fig. II-3 were numerically integrated to point C. These data are summarized in Table II-1.

Table II-1
Energy Storage Estimates
CPN17 MLC's at 77 K

E_C,kV/cm	ΔF, J/cm^3	ΔF, J/g
214(a)	0.81	0.13
400	1.8	0.28
600	3.4	0.55
900	7.2	1.2
1080 (Fig. II-2)	10.5	1.7
1080(b)(Fig. II-3)	51-58	8.2-9.3

(a) Limit of Fig. II-2 data

(b) Limit of Fig. II-3 data

The range of ΔF-values in Table II-1 for the induced-state case reflects the spread in the upper curves in Fig. II-3.

Specific heat and electrocaloric data were measured on CPN17 MLC's from the first batch. The zero-field specific heat data were measured by the dynamic pulse method,[4] and the electrocaloric temperature changes ΔT_e were measured by cycling the field $0 \rightarrow E \rightarrow 0$ and monitoring the temperature change of the MLC under adiabatic conditions. The results of these measurements are shown in Figs. II-4 and II-5.
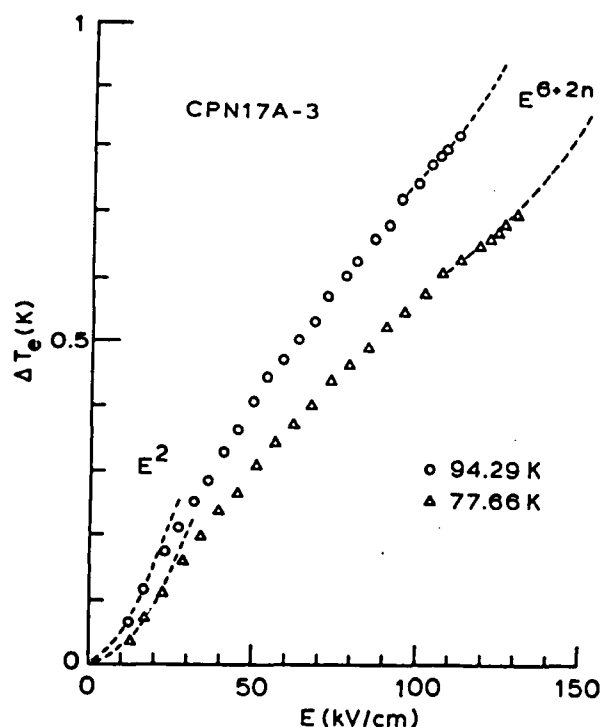

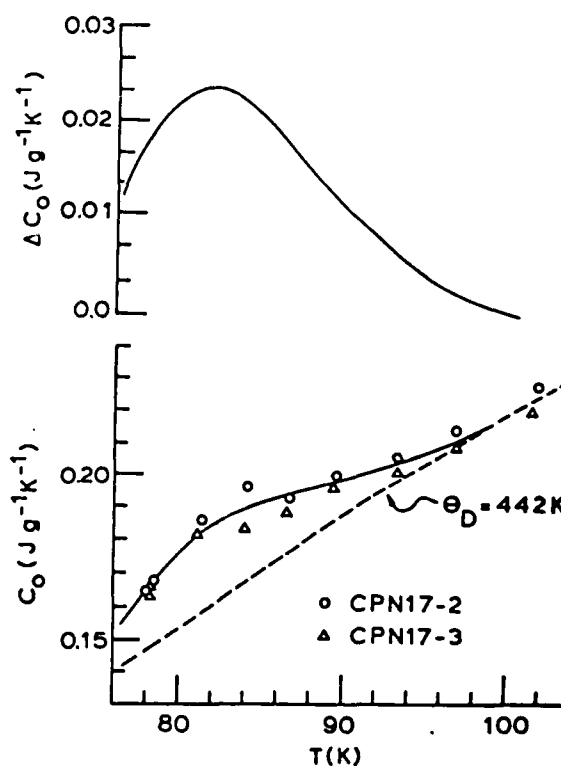Figure II-4. Reversible electrocaloric temperature changes in CPN17.

Figure II-5. Specific heat of the CPN17 ceramic in the MLC's in zero field.

-7-

The expected electrocaloric cooling effects in CPN17 are
demonstrated in Fig. II-4, and it was found in these measurements
that the electrocaloric effects were perfectly <u>reversible</u> as
suggested by the dielectric data. Note that the E-fields in Fig.
II-4 are well below the induced-phase switching field of Fig.
II-3.

The specific heat data in Fig. II-5 show evidence of an
excess specific heat around 84 K and are fitted at the higher
temperatures to a Debye Model (θ_D = 442 K). Some specific heat
data were measured as a function of electric field also, and it
was found that E-field <u>suppresses</u> the specific heat, but the
effect is not large ($\sim$ 5 % at 100 kV/cm).

Finally, <u>all</u> the data measured on the first-batch MLC's
(i.e., ε_0 in Fig. II-1, ε_E in Fig. II-2, ΔT_e in Fig. II-4, and C
in Fig. II-5) were analyzed according to the Ginzburg-Landau
formalism for the free-energy,[5]

$$A = A_0 + \frac{1}{2} \chi P^2 + \frac{1}{4}\xi P^4 + \frac{1}{6}\zeta P^6 + \ldots \qquad (II-2)$$

in combination with the TdS equation for dielectrics,[6]

$$TdS = C_E dT + T(\partial P/\partial T)_E \, dE \qquad (II-3)$$

where P is the polarization. The connecting relationships from
Eq. (II-2) are $E = \partial A/\partial P$ and $4\pi/\varepsilon = \partial^2 A/\partial P^2$, and ξ and ζ were
assumed temperature independent in these analyses.

It was found that all the dielectric and thermal data in the
low field region (i.e., E < 200 kV/cm) could be satisfactorily
explained and correlated according to this thermodynamic
formalism, and the fitted parameters ξ and ζ agreed well with the
values determined for other ferroelectrics.

One of the central results of this thermodynamic analysis is
that the electrocaloric-cooling temperature drops on discharge
are directly related to dielectric properties according to

$$\Delta T_e \propto d\varepsilon_0/dT. \qquad\qquad (II-4)$$

This correlation is important for capacitive energy storage because it indicates how the electrocaloric effects can be maximized (or minimized).

III. THERMAL DUTY-CYCLE STUDIES

The basic concept here is a storage bank of CPN17 multilayer capacitors (MLC's) immersed in liquid nitrogen, and this bank is periodically charged and discharged. Both reversible and irreversible heating and cooling phenomena occur during charging and discharging, and since isothermal starting conditions are important to take advantage of the large dielectric constant, it follows that the duty cycle may be determined by thermal rather than electrical properties. That is, the time between repetitive chargings may depend on the time required for the bank to recover thermally from the heating and cooling effects during one cycle. Since all MLC's in the bank are identical, only one MLC need be studied. Thermal-recovery times are strongly geometry-dependent; thus, the design of the MLC may determine the practical duty cycle of the storage bank.

These elementary considerations led us to initiate thermal studies at the beginning of this program so as to be in a timely position to provide guidelines for MLC designs later in the program. Since these thermal studies were separate from, and ran in parallel with, the MLC-parameter-development research, they will be documented separately in this section to establish these guidelines.

The studies here were evolutionary in nature and involved both experimental and theoretical research. Consequently, in what follows below we will follow the chronological order in which the research was performed.

Anisotropic Thermal Conductances in an MLC

The first step here is to measure accurately the thermal conductances in two directions in the MLC since the embedded metal electrodes enhance the longitudinal heat conduction, as we shall see. Also, the temperature-dependences of the thermal conductivities of the ceramic and of the metal electrodes must be taken into account.

The scheme of the measurements here is best understood with

-10-

reference to Fig. III-1 which is a schematic representation of an MLC. First, it is seen that for heat flow <u>parallel</u> to the electrodes (longitudinal mode) <u>both</u> the ceramic <u>and</u> the metal electrodes contribute to the heat flow. On the other hand, for heat flow <u>perpendicular</u> to the electrodes (transverse mode) the metal electrodes act as isothermal planes but do <u>not</u> contribute to the heat flow. Therefore, our goal here is to measure κ in both the longitudinal and transverse modes using MLC's with different metal electrodes (ternary and pure Pt) and with different geometries (i.e., W, d, t_{cp}, t_m, and t_p in Fig. III-1). In addition, the E-field dependence of κ will be measured in the transverse mode.

<u>Experimental Methods</u>. In all the κ-measurements here, the two-thermometer, linear heat flow method was used. One side of the MLC was indium-soldered to the reservoir in the adiabatic calorimeter, and a heater was attached to the other side of the MLC. With this heater activated, a linear temperature gradient develops across the MLC at steady state, and the thermal conductivity is given by

$$\kappa = i^2 R / \Delta T (A/x) \qquad (III-1)$$

where ΔT is the temperature difference between the two thermometers separated by x, A is the cross-sectional area of the MLC perpendicular to the heat flow, and R is the heater resistance driven by the exciting current i. Note that κ given by Eq. (III-1) is the gross thermal conductivity and may have separate components (see below).

The thermometers used in these measurements were ground Allen-Bradley 1 kΩ BB resistors heat sunk to the MLC and measured in the four-lead, dc potentiometric method. All measurements were made using six-place Keithley Model 181 voltmeters, and the resistor thermometers were calibrated <u>in situ</u> during the course of the runs against a calibrated Pt secondary standard thermometer.

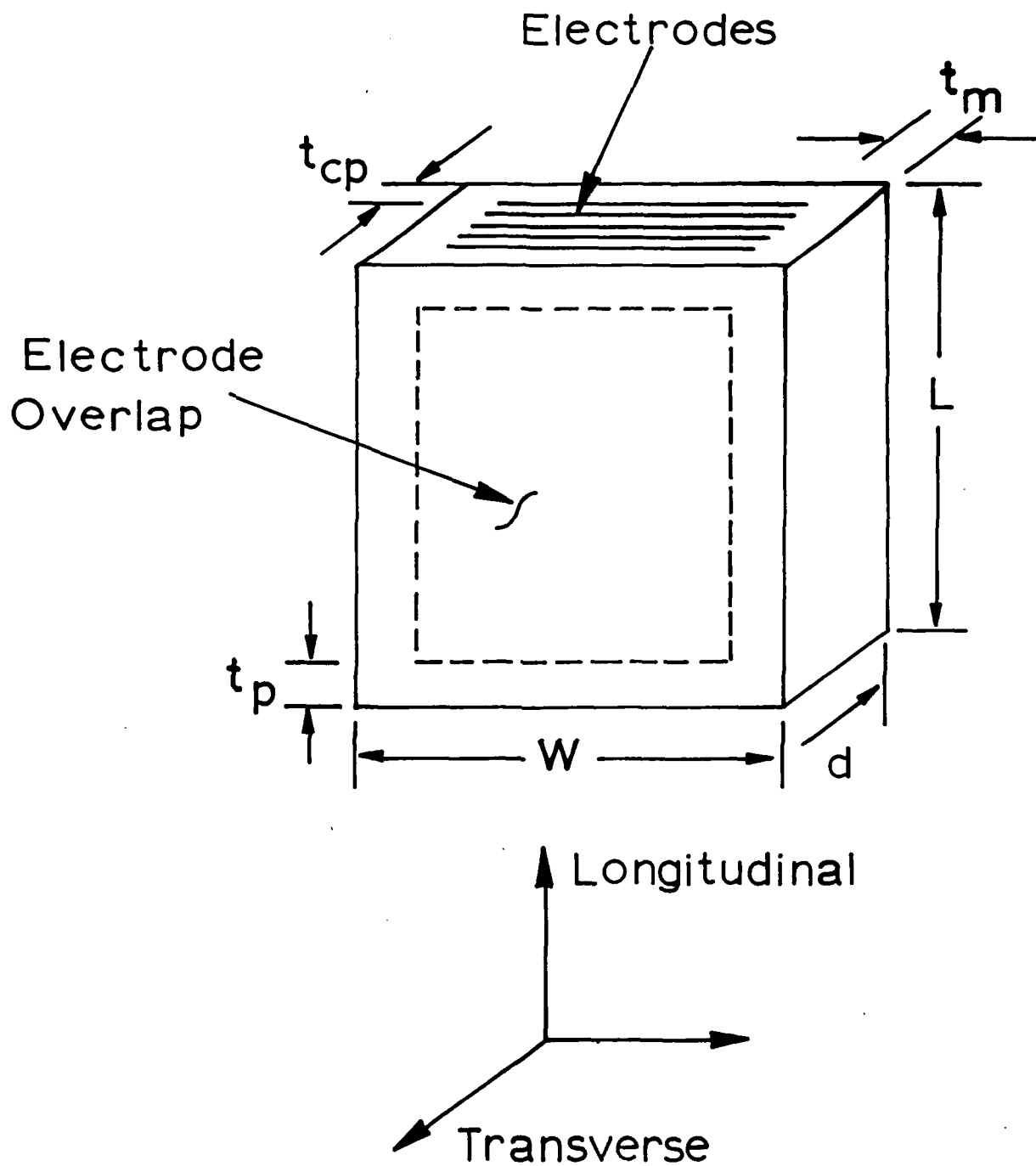Referring to Fig. III-1, to measure an MLC in the longitudi-

-11-

Figure III-1. Schematic drawing of an MLC showing the longitudinal and transverse directions of heat flow.

nal mode, one end of the MLC with exposed electrodes was indium-soldered to the reservoir. For the transverse mode, a major face of the MLC was indium-soldered to the reservoir. All indium-solderings were accomplished by first firing a silver paste on the end or face of the MLC. In the case of the transverse-mode measurements, fine copper wires (3×10^{-3} cm diam) were also indium-soldered at the interface between the major face of the MLC and the reservoir, and the free ends of these wires were bundled and wrapped around a resistor thermometer with varnish. Next, a copper sheet was varnished to the remaining, major face of the MLC, and the second thermometer and the heater were fixtured to this copper sheet.

Measurement of the E-field dependence of κ in the transverse mode proved particularly challenging for a simple reason: The metal strips used to contact the embedded electrodes could act as thermal shunts; that is, referring to Fig. III-1, the heat supplied to one major face could flow laterally along the embedded electrodes to the metal strips and thence to the remaining face. To pursue these measurements, _two_ runs were made on the same MLC involving different configurations of the metal strips; air dry Ag strips were used in both cases, and one case involved thick stips, the second case, thin strips. Also, the MLC chosen had ternary electrodes due to the lower thermal conductance compared to Pt electrodes (see below), and this choice minimizes the thermal-short problem.

In these E-field measurements the capacitance of the MLC mounted in the calorimeter was measured at room temperature to insure that all the metal electrodes were electrically contacted.

The parametric data for the MLC's measured are summarized in Table III-1 (referenced to Fig. III-1); here N refers to the number of embedded metal electrodes.

Table III-1
Parametric Data for MLC's [a]

MLC	Electr. [b]	W	d	N	t_m	L	Mode
III-0190-4	Ternary	0.9987	0.2756	–	0.1019	0.9980	Transv
III-0190-15	Ternary	0.9972	0.2659	35	0.0990	–	Long.
III-0189-15	Pt	1.0053	0.2568	35	0.1000	–	Long.
I-0210-2	Pt	1.0038	0.2207	20	0.0600	–	Long.
I-0211-1	Ternary	1.0003	0.2375	20	0.0888	–	Long.

[a] Refer to Fig. III-1. All dimensions in cm.

[b] Ternary electrodes are Pt-Pd-Au alloys.

    Experimental Results. Gross thermal conductivity data measured in the longitudinal mode on four MLC's are shown in Figs. III-2 and III-3. The I-0210 and -0211 MLC's in Fig. III-2 have thick dielectric layers (i.e., small N) whereas the III-0189 and -0190 MLC's in Fig. III-3 have thin dielectric layers, and note that the two types of electrodes are involved in both figures. As seen, the MLC's with Pt electrodes (I-0210-2 in Fig. III-2 and III-0189-15 in Fig. III-3) have the larger gross κ's compared to the MLC's with ternary electrodes. This is to be expected because alloys have lower thermal conductivities than pure metals, particularly at cryogenic temperatures.

    All longitudinal κ-data in Figs. III-2 and III-3 vary linearly with temperature, 70-110 K, and the least-squares κ-T fits are shown by the solid lines.

    Gross thermal conductivity data measured in the transverse mode on the III-0190 MLC are shown in Fig. III-4. As mentioned above, two runs were made on this MLC, the first run with thick Ag strips, the second with thin Ag strips. As seen in Fig. III-4, the first run resulted in a larger κ due to the thermal-short problem, but the effect is not large (~ 4%). Again, least-square κ-T fits are shown in Fig. III-4.

    Finally, the E-field dependence of κ measured in the transverse mode on the III-0190 MLC in two runs is shown in Fig. III-5 up to 100 kV/cm. The first-run data are ~ 2% larger than the second-run data due to two effects: (1) The thermal-short con-
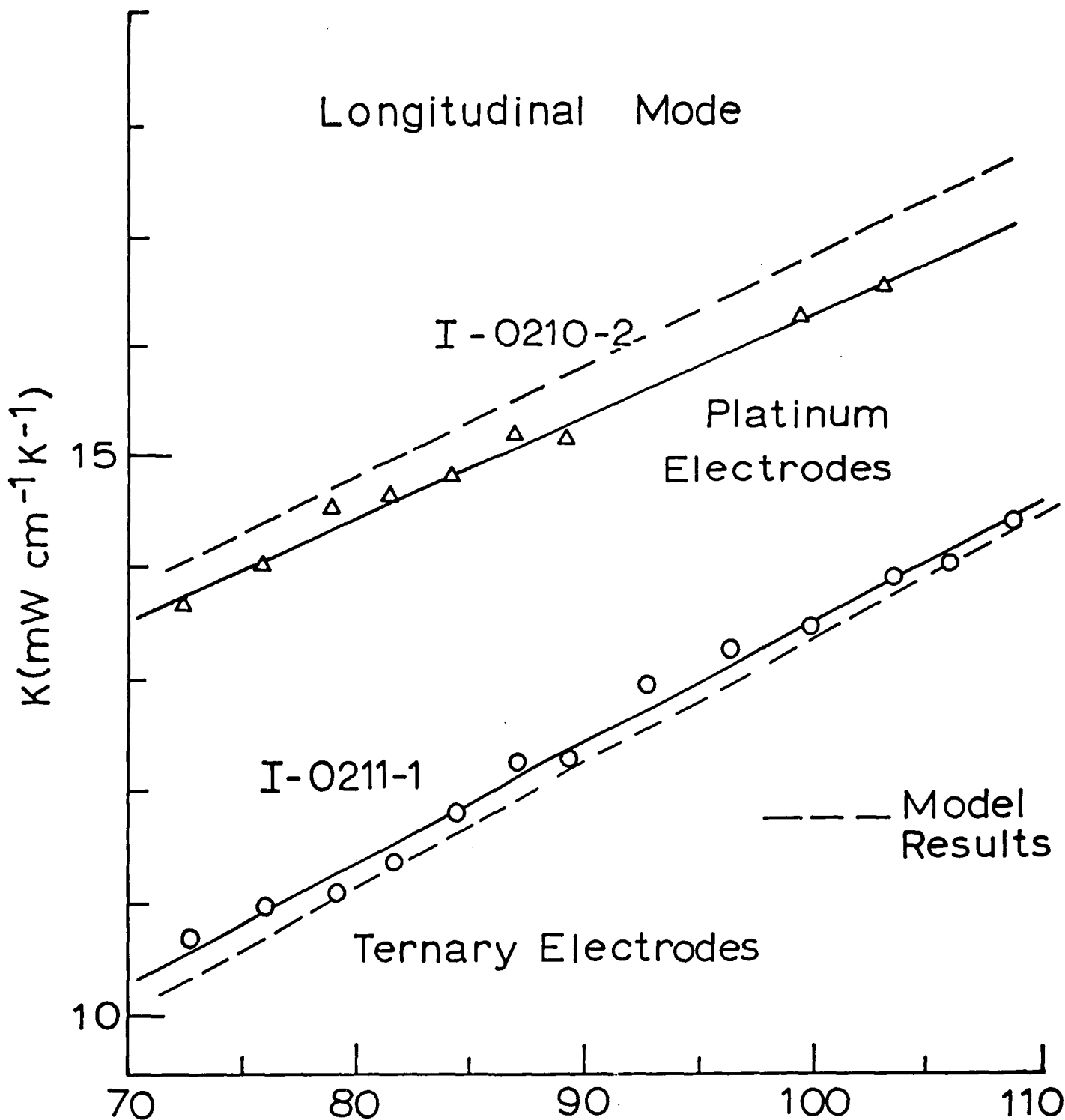
Figure III-2. Longitudinal thermal conductivity data measured on MLC's with thick dielectric layers. Model results are shown by dashed lines.
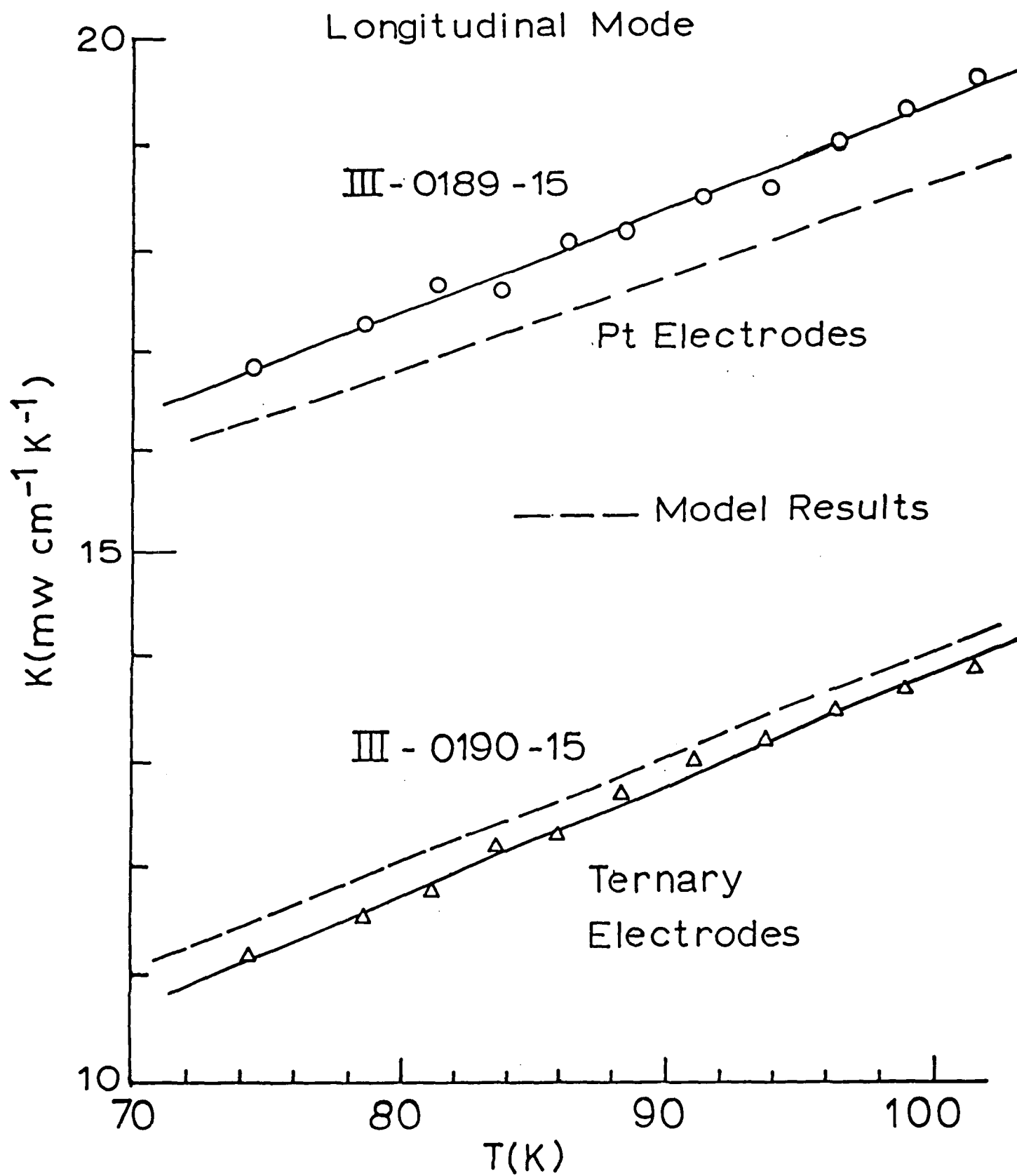
Figure III-3. Longitudinal thermal conductivity data measured on MLC's with thin dielectric layers. Model results are shown by dashed lines.
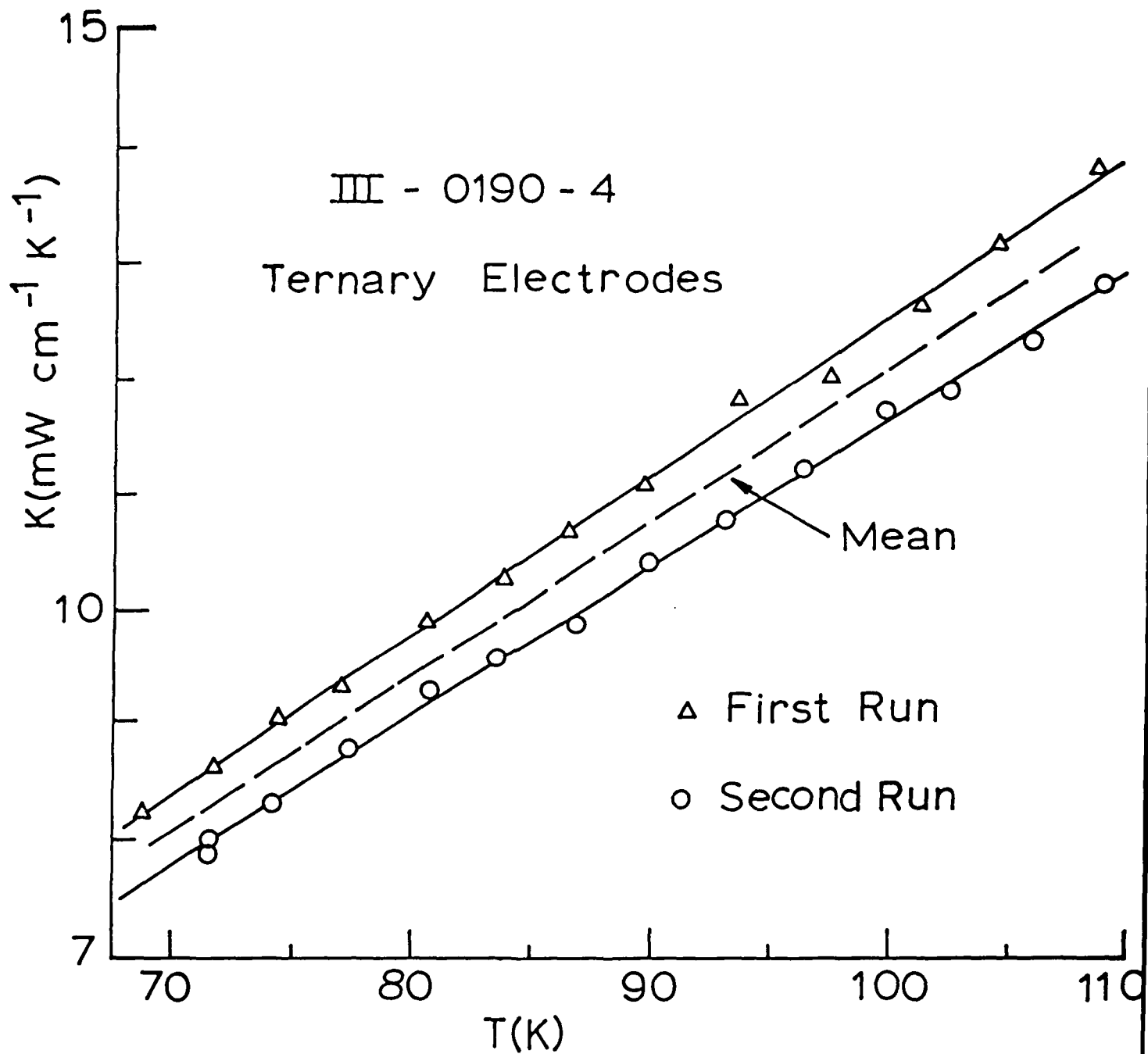
Figure III-4. Transverse thermal conductivity data measured in two runs on the same MLC. Two runs were made to examine possible thermal shorting (see text), and model results are shown by the dashed line.
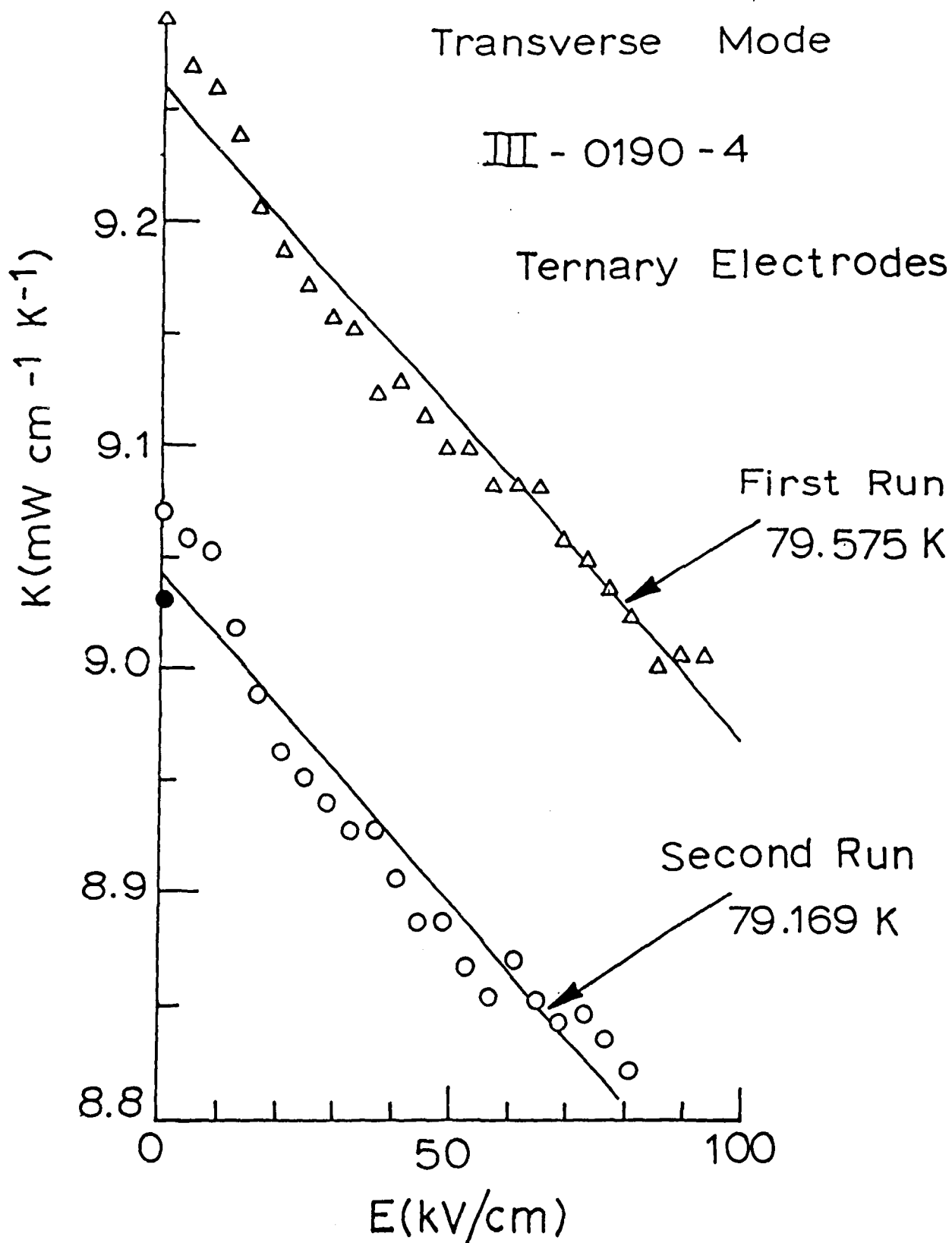
Figure III-5. Electric-field dependence of the transverse thermal conductivity measured in two runs. The lines are least-squares fits, and the solid point at the origin in the second run is the closure point (E → 0).

siderations mentioned above; and (2) The slightly higher average temperature for the first run. Least-squares κ-E fits are shown in Fig. III-5, and the _slopes_ of these fits are essentially identical.

Data Analyses. In this section we will mathematically model the gross thermal conductivity data above in order to separate the κ's of the various components of the MLC. The broad goal here is to provide a data base for modelling the heat flow properties of an MLC.

To analyze thermal conduction in a multi-component system such as an MLC, we make use of the _thermal conductance_ G defined by

$$G = \kappa \ (A/x) \qquad\qquad (III-2)$$

where A is the cross-sectional area perpendicular to the heat flow and x is the distance across which the heat flow is measured (i.e., the separation of the thermometers). Referring to Fig. III-1 for the _longitudinal_ mode, the total conductance G_t is made up of the ceramic conductance, G_c, and the metal electrode conductance, G_e. These heat-flow paths are in parallel for which conductances add, so that

$$G_t = G_c + G_e, \qquad\qquad (III-3)$$

and making use of Eq.(III-2) according to Fig. III-1, we have

$$\kappa_t Dd = \kappa_c Dd + \kappa_e t_e N \ (D-2p) \quad \text{(Longitudinal)}, \qquad (III-4)$$

where t_e is the thickness of a metal electrode. In arriving at Eq.(III-4) we have ignored the total thickness of the electrodes ($Nt_e \sim 4 \times 10^{-3}$ cm) compared to the MLC thickness (d ~ 0.25 cm), and, of course, κ_t, κ_c, and κ_e in Eq.(III-4) refer to the total (gross), ceramic, and electrode thermal conductivities, respectively. Note that the separation x in Eq.(III-2) is common to

all the terms in Eq.(III-3).

In the transverse mode in zero field, the metal electrodes do not contribute so that

$$\kappa_t = \kappa_c \qquad \text{(Transverse)}. \qquad \text{(III-5)}$$

We therefore immediately have κ_c for the ceramic material from the transverse data in Fig. III-4,

$$\kappa_c = 0.1336\ T - 1.2682\ (\text{mW cm}^{-1}\ \text{K}^{-1}) \qquad \text{(III-6)}$$

where we use the average of the two runs in Fig. III-4 as shown by the dashed line.

Turning next to the longitudinal data in Figs. III-2 and III-3, we use Eq.(III-4) with the data in Table III-1 and Eq.(III-6) to solve for the product $\kappa_e t_e$ for ternary and Pt electrodes. This is done at two temperatures, 80 and 100 K, and the curve-fitted κ_t-data in Figs. III-2 and III-3 are used. The results of these analyses are summarized in Table III-2.

Table III-2
Metal-Electrode Conductivities

	$\kappa_e t_e$ (mW K^{-1})	
T(K)	Pt	Ternary
80	$(6.788 \pm 7.21\%) \times 10^{-2}$	$(2.501 \pm 12.13\%) \times 10^{-2}$
100	$(5.933 \pm 11.64\%) \times 10^{-2}$	$(1.810 \pm 11.15\%) \times 10^{-2}$

Finally, assuming linear κ_e-T approximations, we have the final results for the metal elelctrodes,

$$\kappa_e t_e = -4.271 \times 10^{-4}\ T + 0.1020\ \text{(Pt)}$$
$$\kappa_e t_e = -3.457 \times 10^{-4}\ T + 5.2662 \times 10^{-2}\ \text{(Ternary)} \qquad \text{(III-7)}$$

in units of mW K^{-1}.

Equations (III-6) and (III-7) are the central results of this study, and these model results are shown in Figs. III-2 and

III-3 as dashed lines plotted according to Eq.(III-4). As seen, these model results describe the experimental data satisfactorily (± 3.2 % in the worst case).

Turning now to the E-field data in Fig. III-5, we have to distinguish between the active, electroded ceramic material, G_a, and the inactive, unelectroded ceramic, G_i,

$$G_t = G_a + G_i \qquad\qquad (III-8)$$

Solving, we find that

$$\kappa_a = \kappa_i \ (1 + mE/\phi), \quad \phi = (W - 2t_p)(L - 2t_m)/WL \qquad (III-9)$$

where $m = d\kappa_t/dE$ and $t_p = 0.0983$ cm (not given in Table III-1). We have cast Eq.(III-9) in terms of the coefficient m because the κ_t vs. E slopes in Fig. III-5 from the curve fittings of the two runs agree very well, $m = -(3.212\pm1.9\%)\times10^{-4}$. Solving using the data in Table III-1 in Eq.(III-9), we find

$$\kappa_E = \kappa_0 \ (1 - 5.025\times10^{-4} \ E)$$
$$E \text{ in kV/cm.} \qquad\qquad (III-10)$$

Discussion. In the above sections, experimental thermal conductivity data have been reported and analyzed, and the main findings are given in Eqs.(III-6), (III-7), and (III-10). The thermal models agree very well with the measured data, and there is consistency in the data (e.g., for both the Pt and ternary electrodes $d\kappa_e/dT$ is negative).

It is interesting to compare the derivatives $d\kappa_t/dT$ calculated from Eq.(III-4) using Eqs.(III-6) - (III-7) with the experimental values (curve-fitted) from Figs. III-2 and III-3. This comparison is given in Table III-3.

-21-

Table III-3
Comparison of $d\kappa_t/dT$ Data
$d\kappa_t/dT \times 10^2 (\text{mW cm}^{-1} \text{ K}^{-2})$

MLC	Electrode	Experimental	Calculated
I-0210-2	Pt	9.15	9.95
III-0189-15	Pt	9.79	9.27
I-0211-1	Ternary	10.61	10.96
III-0190-15	Ternary	10.25	9.71

The agreement in Table III-3 is satisfactory given the assumptions used in modelling the data.

Although we have always dealt with the product $\kappa_e t_e$ (by necessity because t_e is not known accurately), it is clear from Table III-2 and Eq.(III-7) that the Pt electrodes have a significantly _larger_ thermal conductivity than the ternary electrodes -- by a factor of 2.7 at 80 K, rising to 3.3 at 100 K. This is a particularly significant finding because an MLC with ternary electrodes will dissipate heat increasingly poorly as the temperature rises compared to a Pt-electroded MLC. Clearly, Pt electroding is preferable for this energy-storage technology.

The Pt electrodes make a large contribution to the thermal conductance of an MLC. For example, for the III-0189 MLC in the longitudinal mode at 80 K, the Pt electrodes conduct 46% of the heat.

Finally, the electric-field dependence in Eq.(III-10) is relatively minor -- a 5% effect at 100 kV/cm. Also, data here are needed at much higher E-fields to determine the onset of saturation [e.g., Eq.(III-10) predicts $\kappa_E \rightarrow 0$ at $E = 2\times10^3$ kV/cm].

Longitudinal Heat Flow Computations

The experimental measurements above show that the thermal conductance in an MLC is highly anisotropic due to the highly conductive metal electrodes. We now establish a model for the heat flow in an MLC.

The general picture of an MLC in an energy storage bank is

shown schematically in Fig. III-6. The MLC is electrically connected to busbars of copper or aluminum, as shown, and the two dominant heat-flow directions are longitudinal (parallel to the electrodes and into the busbars) and transverse (through the major faces of the MLC and into the liquid-nitrogen bath).

It is a formidable mathematical problem beyond the resources of this program to consider the general case of combined longitudinal and transverse heat flows. We are led to consider only the longitudinal case for two compelling reasons: (1) We have seen above that the metal electrodes make a substantial contributions to the longitudinal (but not the transverse) heat flow, and this contribution can be made even larger by the expedient of thicker metal electrodes; and (2) Even though the tranverse flow involves the thinner d-dimension in Fig. III-6, nonetheless we have to assume that a thermal boundary resistance exists at the solid-liquid interface that may effectively insulate these MLC faces. Moreover, it is safe to assume that a negligible boundary resistance exists at the solid-solid inter- face at the busbar attachment. Therefore, we initially pursue just the case of longitudinal heat flow.

We begin with the exploded view of an MLC shown in Fig. III-7 and consisting of blocks 1,2, and 3. The entire MLC is constructed from the remaining three quadrants. Block 1 is the heart of the MLC where all ceramic layers (except for the cover plates) are electroded. Block 2 is the "pullback" region where approximately half of the electrodes are exposed for termination [e.g., all the (+) or all the (-) electrodes]. Finally, block 3 is the "margin" ceramic containing no electrodes. All electro- caloric phenomena (e.g., polarization heating, depolarization cooling, joule heating, etc.) occur in block 1. The thermal problem reduces to considering how a heating event in block 1 communicates to the surrounding liquid nitrogen bath through the busbars. Specifically, how long does it take for the center of block 1 (i.e., the geometric center) to decay back to the bath temperature following such an event?

Since the metal electrodes have such large thermal conduc-
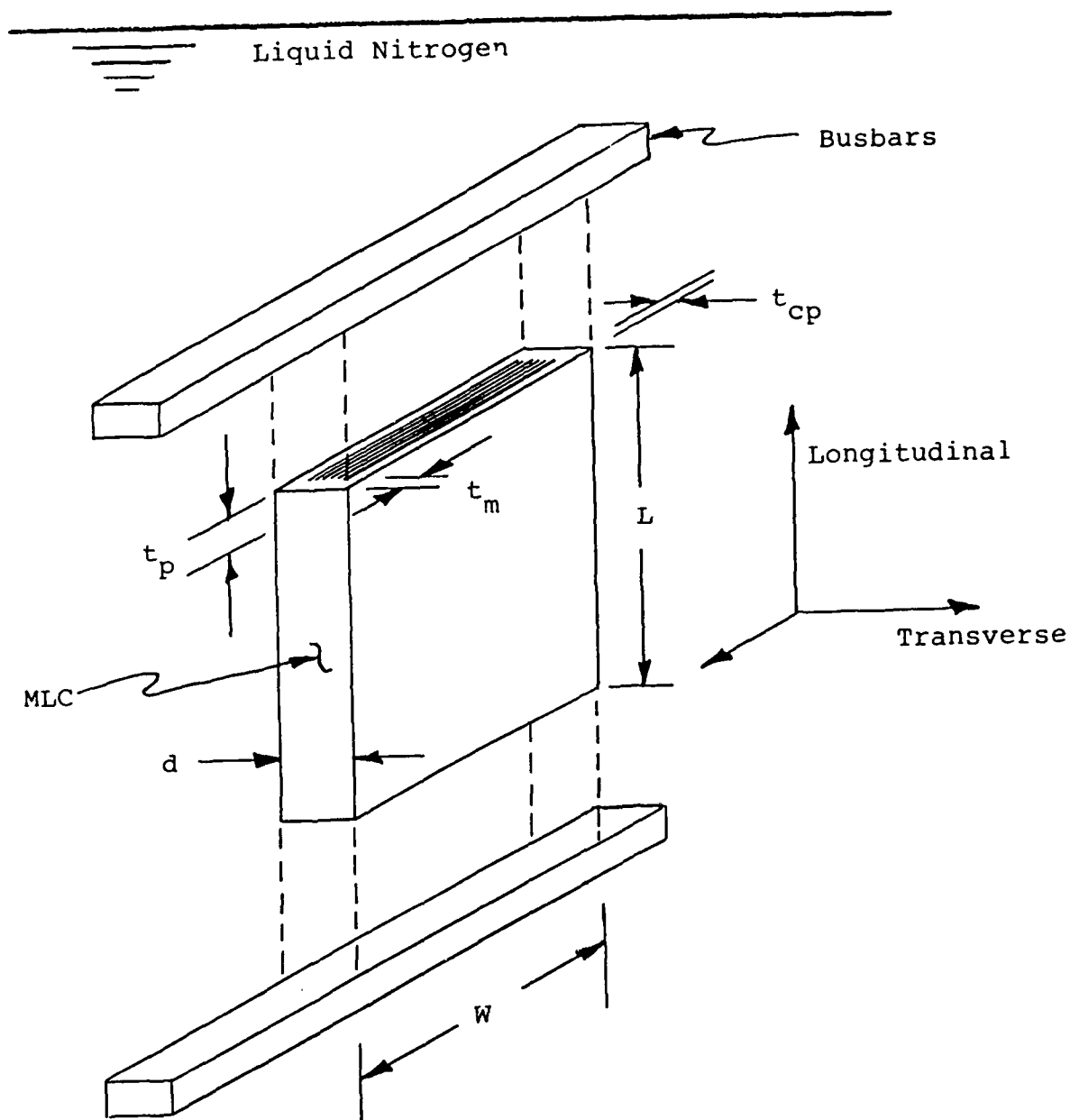
Figure III-6. Basic concept of an MLC of an energy-storage bank immersed in liquid nitrogen. Busbars of copper or aluminum connect to the exposed electrodes, and the dimensional parameters of the MLC are shown.
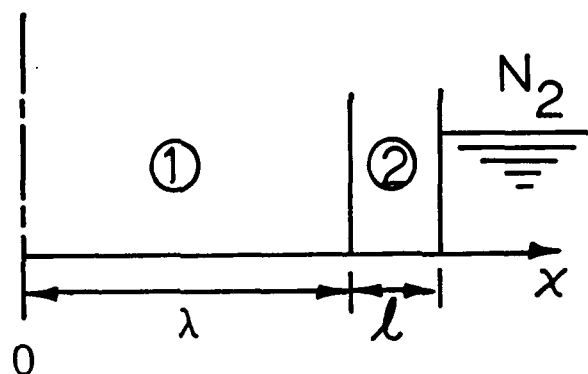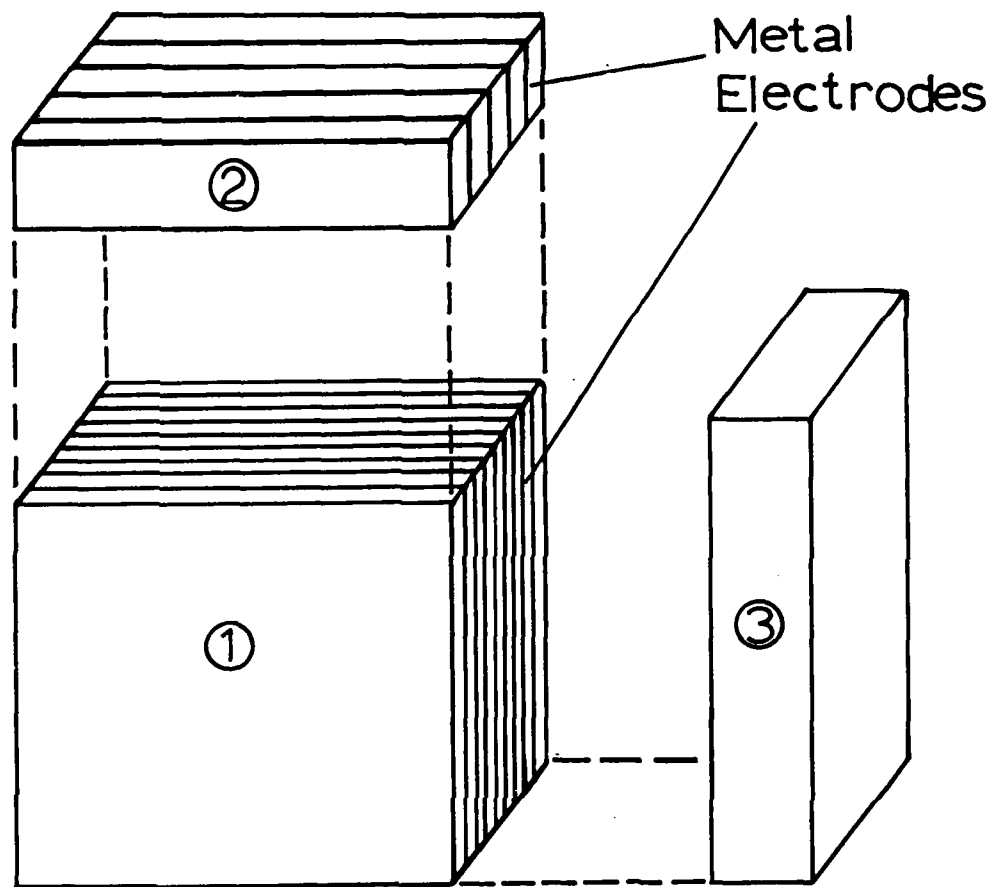
-24-

Figure III-7. Schematic drawing of the three basic blocks of an MLC. The longitudinal heat-flow problem involves blocks 1 and 2 and the one-dimensional case shown at the bottom.

tances compared to the ceramic, only the electroded blocks 1 and 2 need be considered, to a first approximation.

Therefore, the heat-flow problem reduces to the <u>one-dimensional</u> case through blocks 1 and 2, as shown at the bottom of Fig. III-7. Specifically, we consider the case of block 1 of half-length λ bonded to block 2 of width ℓ where the surface of block 2 is maintained at liquid nitrogen temperature via the bus-bars. Comparing Figs. III-6 and -7, it is apparent that $\lambda = \frac{1}{2}L - t_p$ and $\ell = t_p$ (the reason for using λ and ℓ here will become clear when we consider the transverse case below).

The one-dimensional problem in blocks 1 and 2 is described by the respective heat equations,

$$\rho_1 C_1 (\partial T_1 / \partial t) = \kappa_1 \, \partial^2 T_1 / \partial x^2 + U \qquad \text{(III-11)}$$

$$\rho_2 C_2 (\partial T_2 / \partial t) = \kappa_2 \, \partial^2 T_2 / \partial x^2 \qquad \text{(III-12)}$$

where U is the power density dissipated in block 1, ρ is density, C is specific heat, and κ is thermal conductivity. The boundary conditions are that at time t=0 both blocks are at liquid-nitrogen temperature, 77.4 K. The power density U is applied to block 1 for a "pulse time" τ, following which blocks 1 and 2 decay in temperature back to 77.4 K. A very general approach is taken here; U can be thought of as the sum of <u>all</u> electrothermal processes, and τ, as the charge + discharge time.

The computational problem here is to examine the cooldown of the MLC following the pulse, and the clearest way to do this is to examine the <u>centerline</u> temperature at x=0 in Fig. III-7 since this is the <u>last</u> point in the MLC to reach the bath temperature.

The closed-form mathematical solution to Eqs.(III-11) and (III-12) is given in the Appendix, and a computer code was written based on this solution, as also discussed in the Appendix.

Block #1 contains N_1 metal electrodes, and Block #2, N_2 electrodes. Correspondingly, the blocks have thermal conductivities κ_1 and κ_2, respectively. We will develop explicit expressions for κ_1 and κ_2.

Since the electrodes and the ceramic material form <u>parallel</u> conduction paths in both blocks, the thermal conductances <u>add</u>, so that

$$\kappa_1 Wd = \kappa_c Wd + \kappa_e t_e N_1 W$$

$$\kappa_2 Wd = \kappa_c Wd + \kappa_e t_e N_2 W \tag{III-13}$$

using the dimensions given in Fig. III-6. Here the subscripts "c" and "e" refer to the ceramic and electrode, respectively, and t_e is the electrode thickness. For a large number of electrodes, $N_2 = \frac{1}{2}N_1$, and Eqs.(III-13) become

$$\kappa_1 = \kappa_c + \kappa_e t_e (N_1/d)$$

$$\kappa_2 = \kappa_c + \frac{1}{2}\kappa_e t_e (N_1/d). \tag{III-14}$$

Finally, we note that N_1/d is the number of electrodes per cm in block #1, and $N_1/d = 1/t_c$ where t_c is ceramic layer thickness (i.e., dielectric thickness). Therefore, we have the convenient result that

$$\kappa_1 = \kappa_c + \kappa_e (t_e/t_c)$$

$$\kappa_2 = \kappa_c + \frac{1}{2}\kappa_e (t_e/t_c). \tag{III-15}$$

Thus far, the <u>temperature</u> dependences of κ_c, κ_e, and C have been ignored in Eqs.(III-11)-(III-15). These dependences are not large [Fig. III-3 and Eqs.(III-6) and (III-7)], and we take the following appraoch: From the <u>adiabatic</u> <u>relation</u> (i.e., no heat escapes),

$$\tau U = C\Delta T, \tag{III-16}$$

we find that for a $\Delta T = 20$ K temperature rise (77.4 $\rightarrow$ 97.4 K),

$$\tau U = 21.48 \text{ J cm}^{-3} \qquad \text{(III-17)}$$

using the data in Fig. III-3 for the specific heat. Since we anticipate stored energy densities up to ~ 50 J cm^{-3}, the τU-value in Eq.(III-17) is seen as a probable upper limit of the sum of electrothermal processes during charging/discharging. Moreover, as an upper limit, $\Delta T = 20$ K is a reasonable temperature rise and is well within the limits of the experimental data.

Consequently, for modeling purposes we select thermal-properties data at 87 K, the mid-temperature:

$$
\begin{aligned}
\kappa_c &= 10.36 \text{ mW cm}^{-1} \text{ K}^{-1} \\
\kappa_e t_e &= 0.0648 \text{ mW K}^{-1} \text{ (Pt electrodes)} \qquad \text{(III-18)} \\
&= 0.0226 \text{ mW K}^{-1} \text{ (Ternary electrodes)} \\
c &= 0.173 \text{ J g}^{-1} \text{ K}^{-1} \\
\rho &= 6.2 \text{ g cm}^{-3}
\end{aligned}
$$

from Fig. II-5 and Eqs.(III-6) and (III-7).

The parameters to study in the computer modeling of longitudinal heat flow are the following from Figs. III-6 and III-7:

1. λ, the half-length of the active ceramic block #1, where $\lambda = \frac{1}{2}L - t_p$.
2. $\ell = t_p$, the pullback thickness of block #2,
3. Platinum versus ternary electrodes,
4. Single versus double, triple, etc. metal electrodes [note that the $\kappa_e t_e$-data in Eq.(III-18) refer to single metal electrodes; to double t_e, for example, we simply double $\kappa_e t_e$),

and 5. t_c, the dielectric layer thickness.

For comparison purposes, we arbitrarily select a "standard case" as follows:

1. $\lambda = 0.50$ cm, $\ell = t_p = 0.2$ cm, $L = 1.40$ cm
2. Single Platinum electrodes   (III-19)
3. $\tau = 0.02$ s ($U = 1074$ J cm^{-3} s^{-1})
4. $t_c = 0.00254$ cm.

MLC Dimensions. The first computer studies involved varying the MLC dimensions L and t_p for the standard case, Eq.(III-19).

The variation of the centerline temperature with time for various L-values between 0.90 and 3.40 cm is shown in Fig. III-8, and these plots reveal several significant findings. First, for $\tau = 20$ ms, the centerline heats rapidly to the adiabatic limit, 97 K (i.e., edge effects are not seen). Most significantly, the duty cycle increases dramatically as L increases. For example, the L = 0.90 cm case has re-cooled in ~ 15 sec, whereas the L = 3.40 cm case has only cooled to ~ 87 K after 40 s. These results have serious, practical ramifications because an L = 0.90 cm MLC is a very small capacitor, whereas one intuitively suspects that much larger MLC's would be more appropriate for this energy-storage concept. Moreover, the dielectric efficiency suffers at small sizes; for example, for L = 0.90 and $t_p = 0.20$, the efficiency is only ~ 50%.

The variation of the centerline temperature with time for various pullback t_p-values between 0.1 and 0.3 cm is shown in Fig. III-9. Here it is seen that the pullback has a substantial effect on the cooldown of the centerline temperature, and one contributing reason for this is that the pullback region has only one-half the number of metal electrodes. For example, the centerline cooldown to 80 K requires 11 and 21 s for the $t_p = 0.10$ and $t_p = 0.30$ cm cases, respectively.

The conclusion here is that the pullback t_p should be made as small as possible for improving the heat dissipation.

Metal Electrodes. As found experimentally the Pt electrodes have a thermal conductivity about three times larger than the ternary electrodes at liquid nitrogen temperatures [e.g., Eq.(III-18)]. In Fig. III-10 is shown the cooldown of the
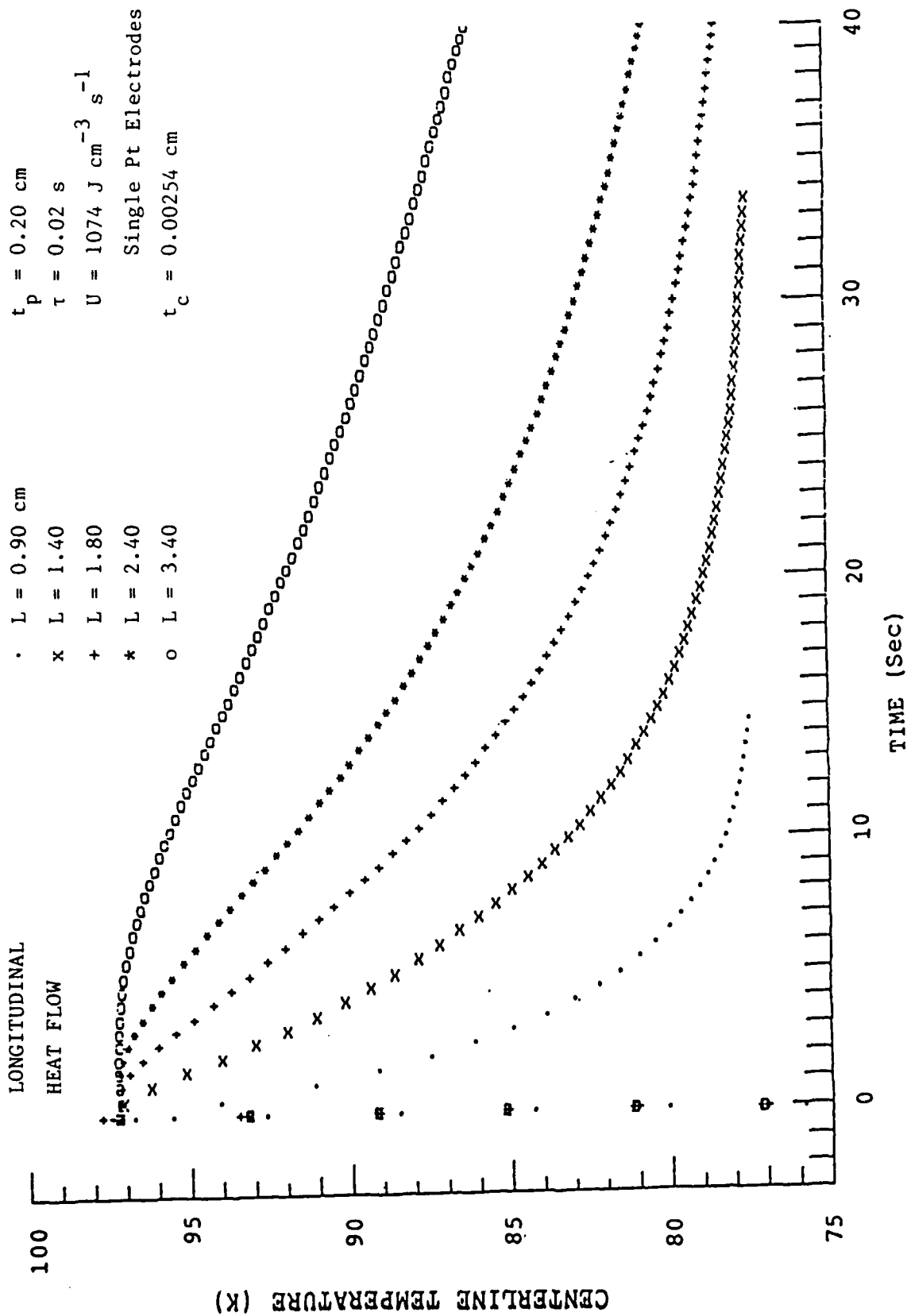
Figure III-8. Variation of the centerline-cooldown temperature with time for various MLC lengths L in the longitudinal heat-flow mode. (see Fig. III-6).

LONGITUDINAL

HEAT FLOW

- L = 0.90 cm
- x L = 1.40
- + L = 1.80
- * L = 2.40
- o L = 3.40

$t_p = 0.20$ cm

$\tau = 0.02$ s

$U = 1074$ J cm^{-3} s^{-1}

Single Pt Electrodes

$t_c = 0.00254$ cm

CENTERLINE TEMPERATURE (K)

TIME (Sec)
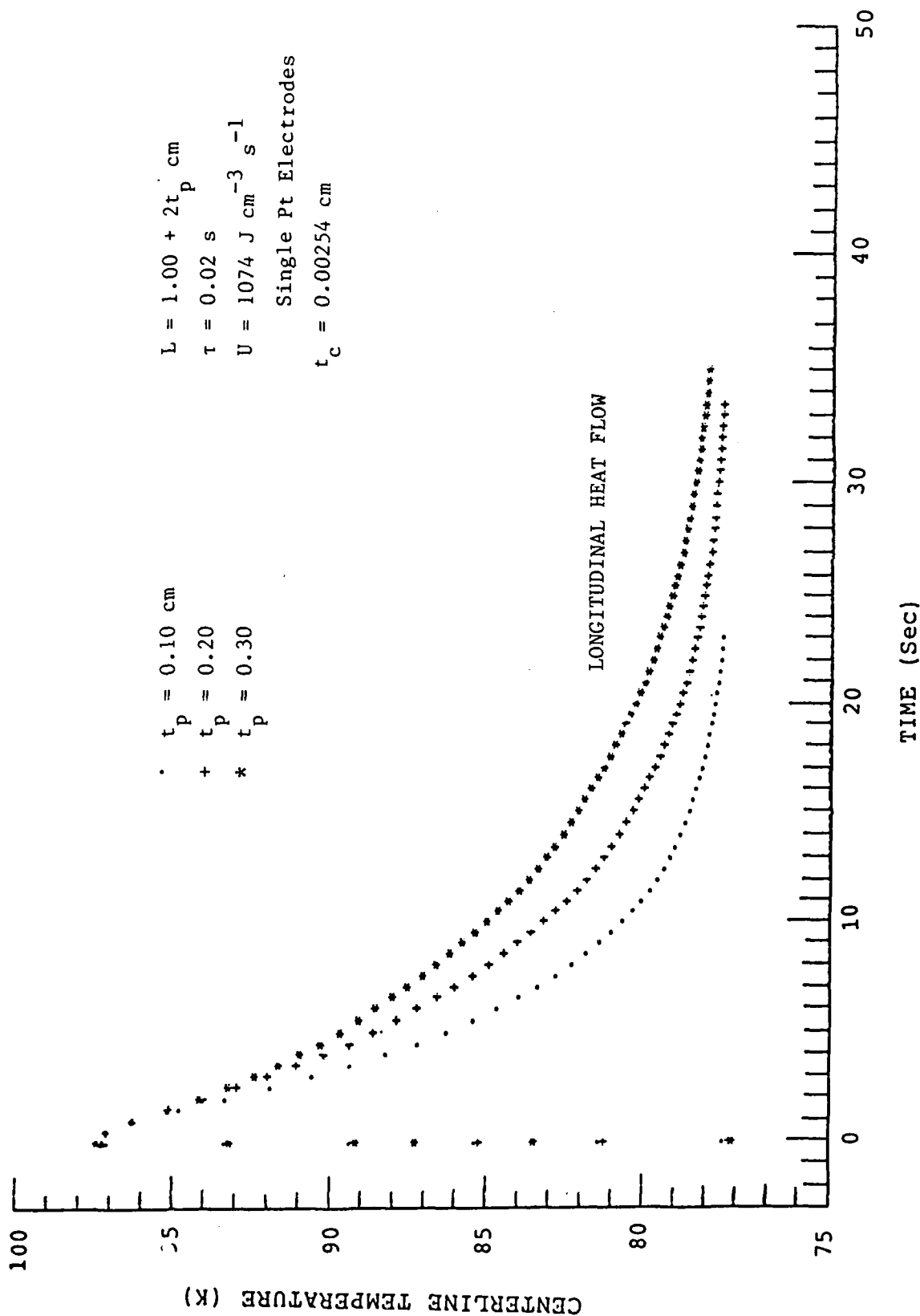
Figure III-9. Variation of the centerline-cooldown temperature with time for various pullbacks t_p for the longitudinal heat-flow mode (note that λ in Fig. III-7 is held constant, and L varies because t_p varies, see Fig. III-6).

Figure III-10. Cooldown time of the centerline temperature for ternary and platinum electrodes for the longitudinal heat-flow mode (single layer). The faster cooldown for the Pt electrode case is due to the larger thermal conductivity.

centerline temperature for these two types of electrodes, and the superiority of the Pt electrodes is clearly evident. For example, the cooldown to 80 K requires 15 and 27 s for the Pt and ternary electrodes, respectively.

Going further, it is possible to increase the thickness of the metal electrodes on silk-screening [i.e., t_e in Eq.(III-18)], and this improves the heat dissipation in both block #1 and #2. This effect is shown in Fig. III-11 where a significant improvement results on going from a single to a quadruple thickness -- i.e., the cooldown to 80 K drops from 16 to 6 s, respectively.

Dielectric Layer Thickness. The dielectric layer thickness, t_c, enters Eq.(III-15) in such a way as to increase the thermal conductivities and thereby shorten the cooldown time. This comes about physically as follows: The number of metal electrodes per unit thickness varies as t_c^{-1}, so the thinner the dielectric layers, the larger the number of metal electrodes and hence the faster the cooldown. This effect is shown in Fig. III-12 for t_c-values between 0.00254 (1 mil) and 0.0127 (5 mil) cm, and the respective cooldowns to 80 K are 16 and 32 s.

Conclusions. The initial studies above immediately establish several important guidelines for the thermal design of energy-storage MLC's according to the longitudinal-heat-flow mathematical model:
1. L and t_p should be minimized.
2. Thick Pt electrodes should be used.
3. Dielectric layers should be as thin as possible.

Duty Cycle Studies

The modelling studies above have revolved around the "standard" case given in Eq.(III-19) for comparison purposes. These studies have revealed that centerline cooldown times are ~ 10 s under the best conditions.

We now consider the effects of U and τ on the thermal duty cycle, and for these studies we select the "best" case from the

Figure III-11. Cooldown time for the centerline temperature for various thicknesses of Pt electrodes for the longitudinal heat-flow mode.
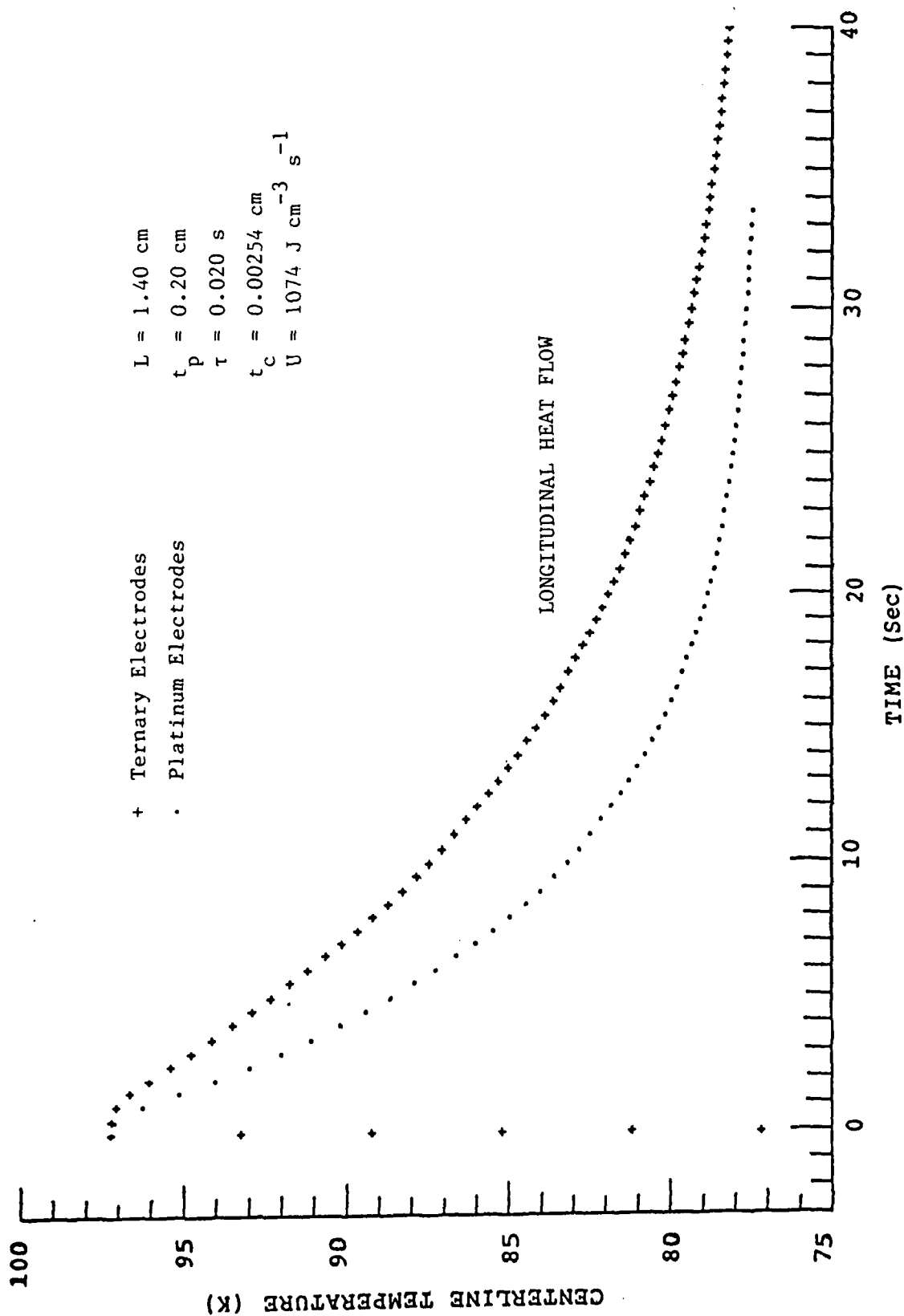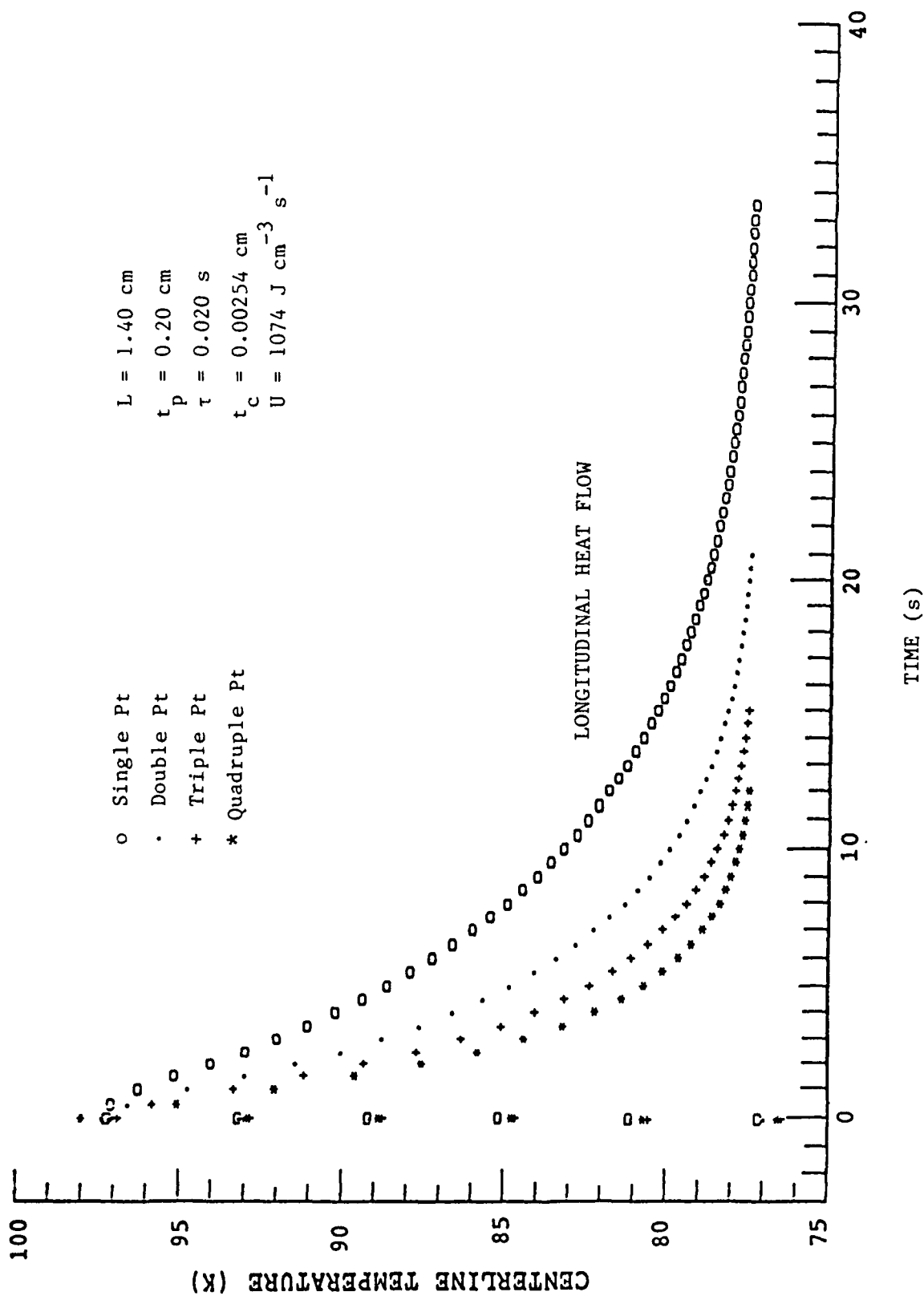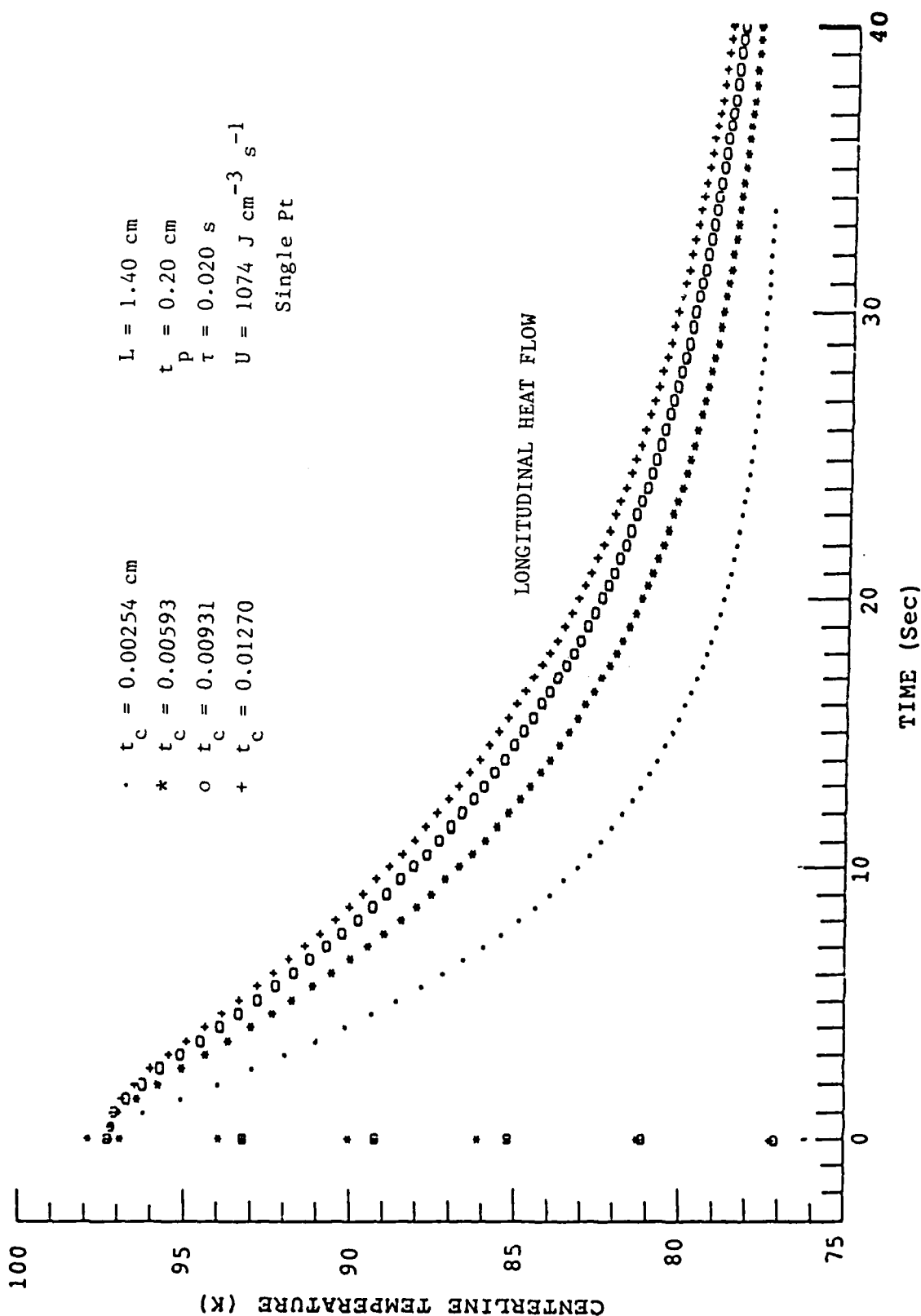
Figure III-12. Cooldown time for the centerline temperature for various dielectric thicknesses, t_c, for the longitudinal heat-flow mode.

above studies that appears practical:

1. $L = 1.20$ cm, $t_p = 0.10$ cm
2. Triple Pt metal electrodes   (III-20)
3. $t_c = 0.00254$ cm.

The first item to study here is the effect of $U\tau$ on the centerline cooldown, since in the studies above we used $U\tau = 21.48$ J cm^{-3} and $\tau = 0.02$ s corresponding to an adiabatic $\Delta T = 20$ K. One can identify two limiting cases here: On the one hand, at large $U\tau$ values there is a large thermal driving force to restore the centerline temperature; on the other hand, small $U\tau$ values lead to small temperature rises but also correspondingly low driving forces. These opposing trends are seen in Fig. III-13 where $U\tau$ is varied from 6 to 21.48 J cm^{-3}, keeping $\tau = 0.02$ s, corresponding to instantaneous (adiabatic) temperature rises from 5.6 to 20 K, respectively. These Fig. III-13 results reveal the significant finding that irregardless of the value of $U\tau$, the thermal duty cycle is about the same for the parameters given in Eq.(III-20), when $\tau = 0.02$ s.

Given this finding for essentially instantaneous heating ($\tau = 0.02$ s), the next question to address is whether increasing τ would reduce the duty cycle. The reasoning here is that edge effects will be felt during longer τ's, thus reducing the centerline temperature at the end of τ. This case was examined by setting $U\tau = 21.48$ J cm^{-3} and varying τ between 0.2 and 5 s. These results are shown in Fig. III-14 and reveal that for $\tau > 0.2$ s the edge effects, while real, are not large enough to substantially improve the duty cycle. In fact, the opposite is observed in Fig. III-14.

Finally, in Fig. III-15 are summarized data for the duty cycle as a function of τ for the parameter case in Eq.(III-20). Here $U\tau = 21.48$ J cm^{-3} is held constant. As seen, the duty cycle remains about constant at 10-12 s for τ up to 1 s; then, the duty cycle increases dramatically for $\tau > 1$ s. Moreover, based on the results shown in Fig. III-13, the Fig. III-15 results will be
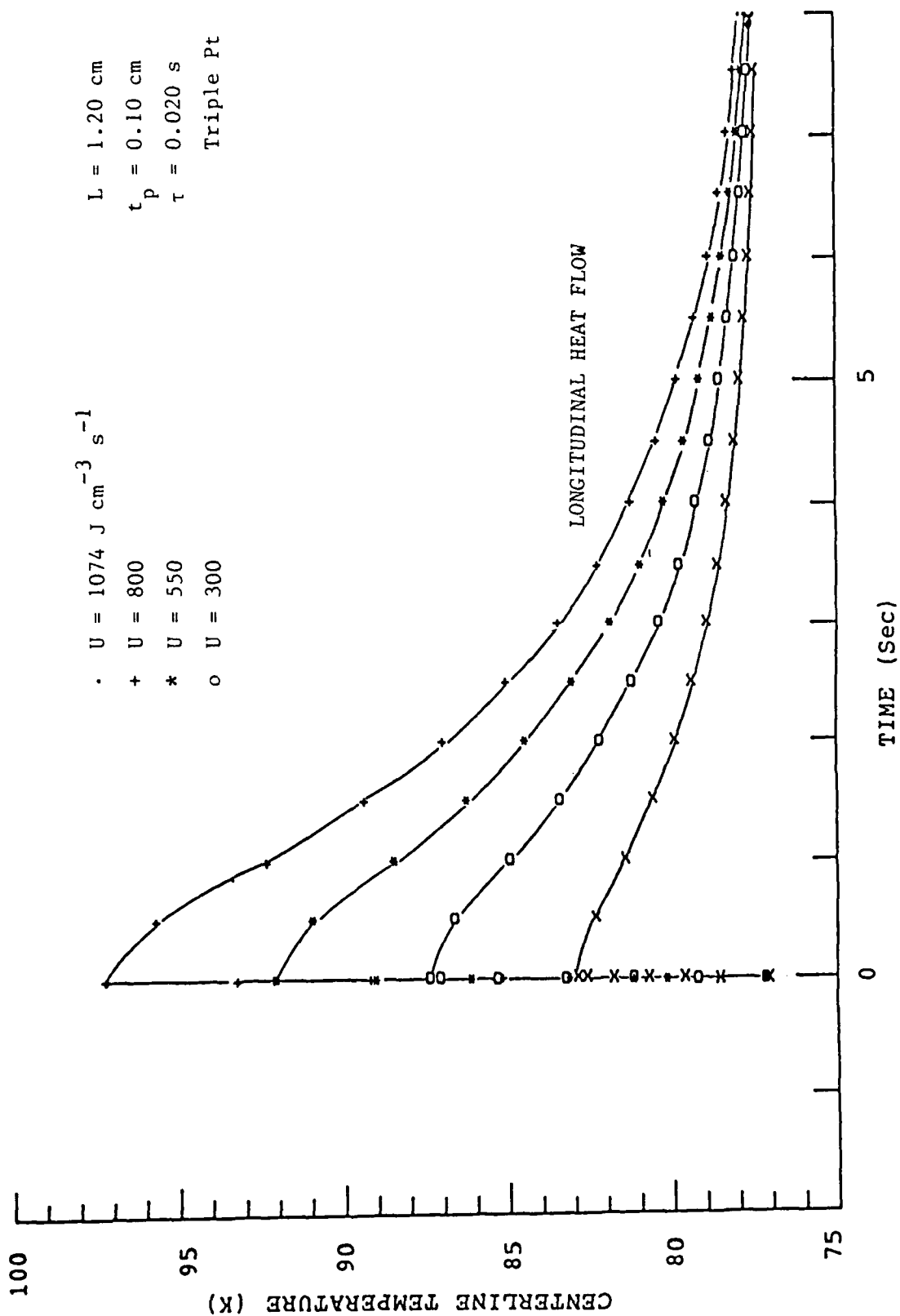
Figure III-13. Centerline cooldown time for various power density values, U, for the longitudinal heat-flow mode.
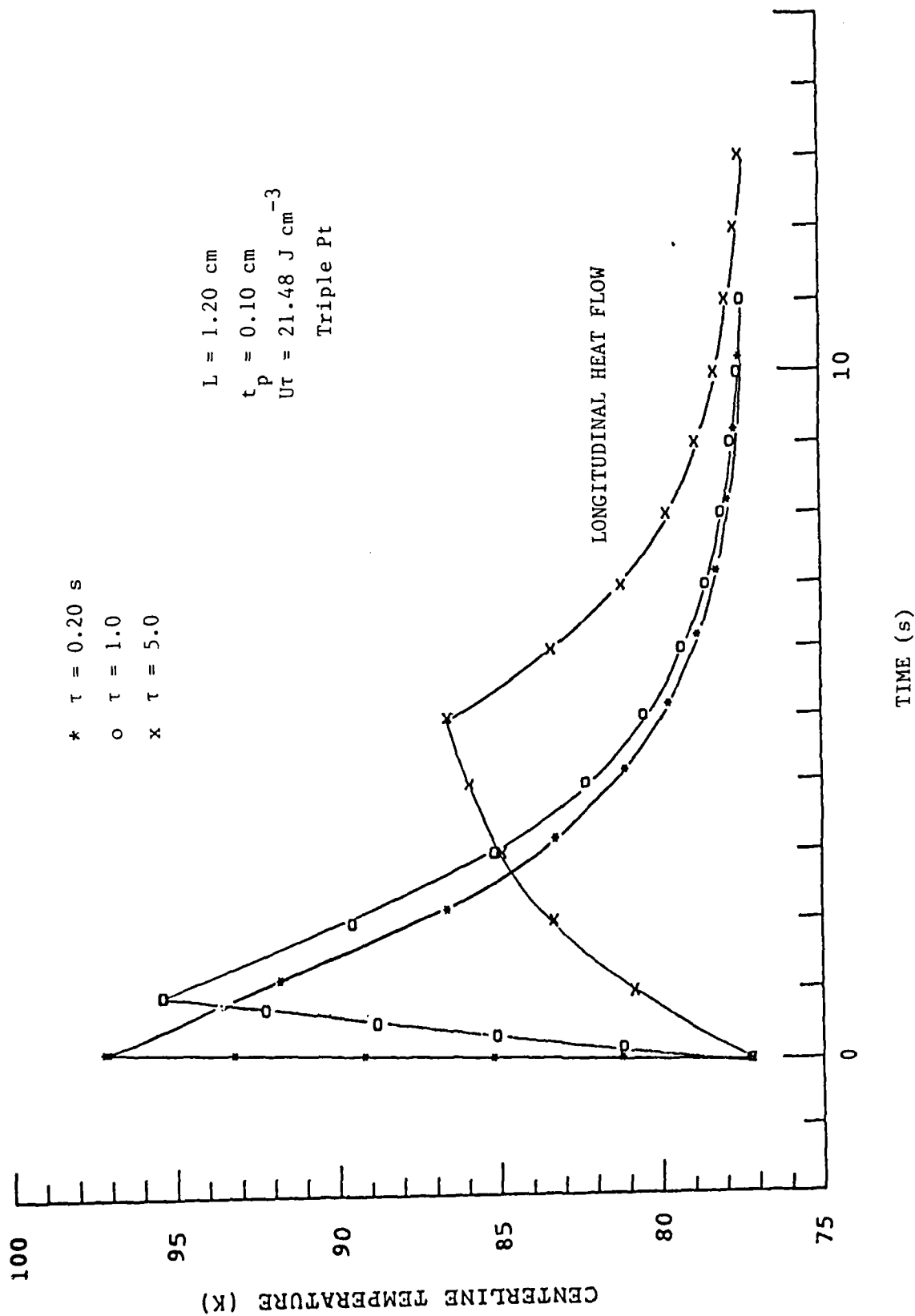
Figure III-14. Centerline cooldown time for long pulse times, τ, holding the product Uτ constant, for the longitudinal heat-flow mode.

LONGITUDINAL HEAT FLOW

L = 1.20 cm
t_p = 0.10 cm
$U\tau$ = 21.48 J cm^{-3}

Triple Pt

TAU (Sec)
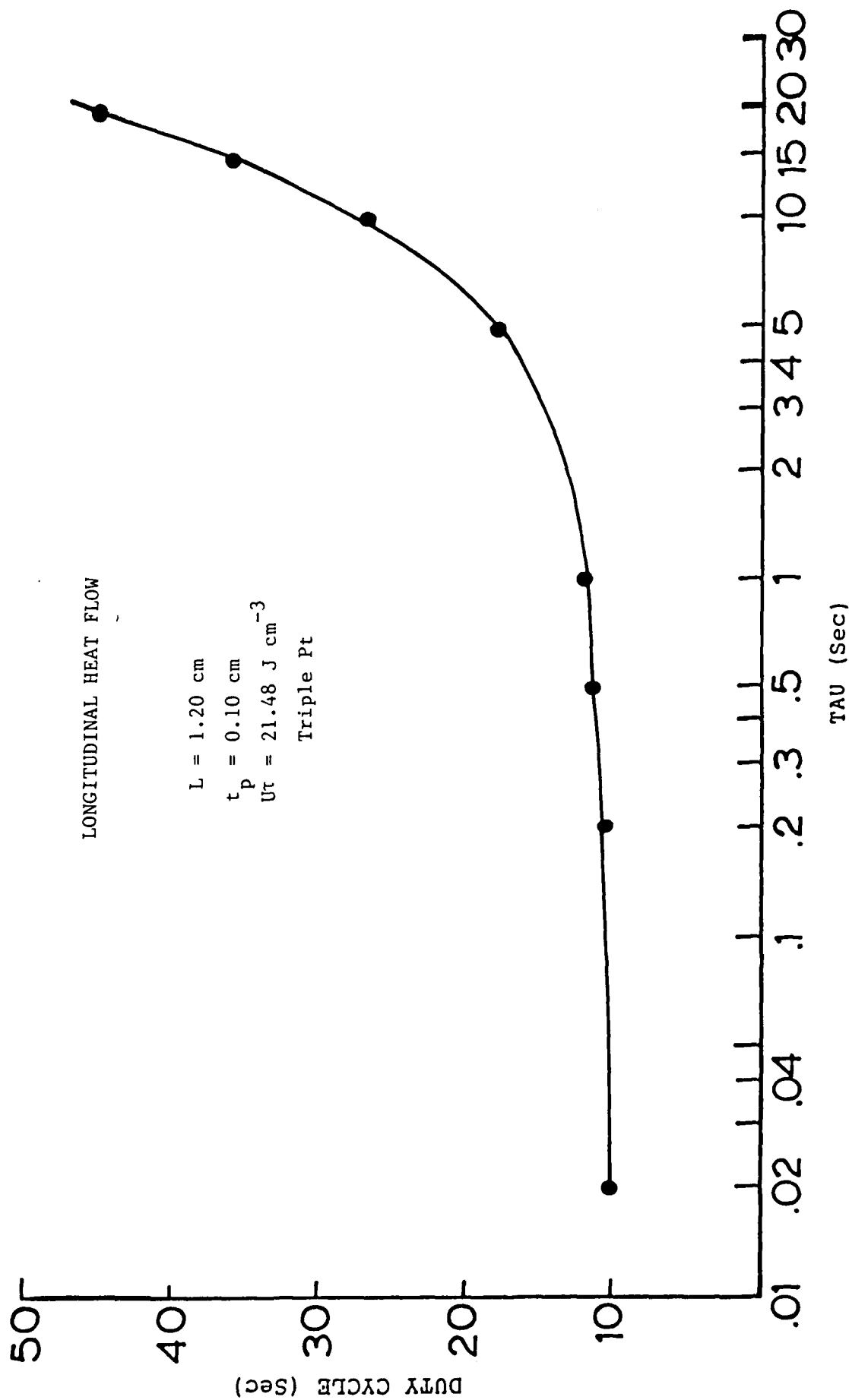
DUTY CYCLE (Sec)

Figure III-15. Summary plot of thermal duty cycle versus pulse time τ for the optimum MLC parameters to promote longitudinal heat flow.

relatively _insensitive_ to U.

Conclusions. These thermal-modeling studies based on _longitudinal_ heat flow parallel to the electrodes (Fig. III-6) have revealed some very significant results regarding the thermal duty cycle and thermal design. The model ignores the _transverse_ heat flow, and we shall return to this point below.

The above studies show that even small energy losses within a capacitor are unacceptable if the duty cycle is repeated at short enough times. Based on the above results, it would be concluded that an MLC should be short and thick and the dielectric layer as thin as possible to provide maximum cooling. However these conclusions assume that energy losses in directions other than parallel to the electrodes are negligible which is not correct (see below). Experimentally, the story is not nearly so grim. As shown later, in this report, thousands of duty cycles six seconds in duration produced no measurable heat rise.

Transverse Heat Flow - Experimental

Given the disappointingly long thermal duty cycles for longitudinal heat flow ($\geq$ 10 s) under _optimum_ conditions, the transverse heat flow has to be examined. In particular, the suspected, large thermal boundary resistance between CPN17 and liquid nitrogen has to be measured carefully.

The measurement of thermal boundary resistance is one of the most difficult low-temperature measurements for two reasons: (1) One side of the solid has to be in a high vacuum, the other side exposed to the liquid, and this places severe demands on the low-temperature seal; and (2) The temperature of the _surface_ of the solid in contact with the liquid has to be measured.

The experimental arrangement adopted here is illustrated schematically in Fig. III-16, and this arrangement successfully solved the two experimental problems mentioned above.

First, one end of a thin-walled, stainless-steel tube was flared into a square cross-section slightly larger than the test MLC, and the MLC was sealed into the tube with an Indium seal.

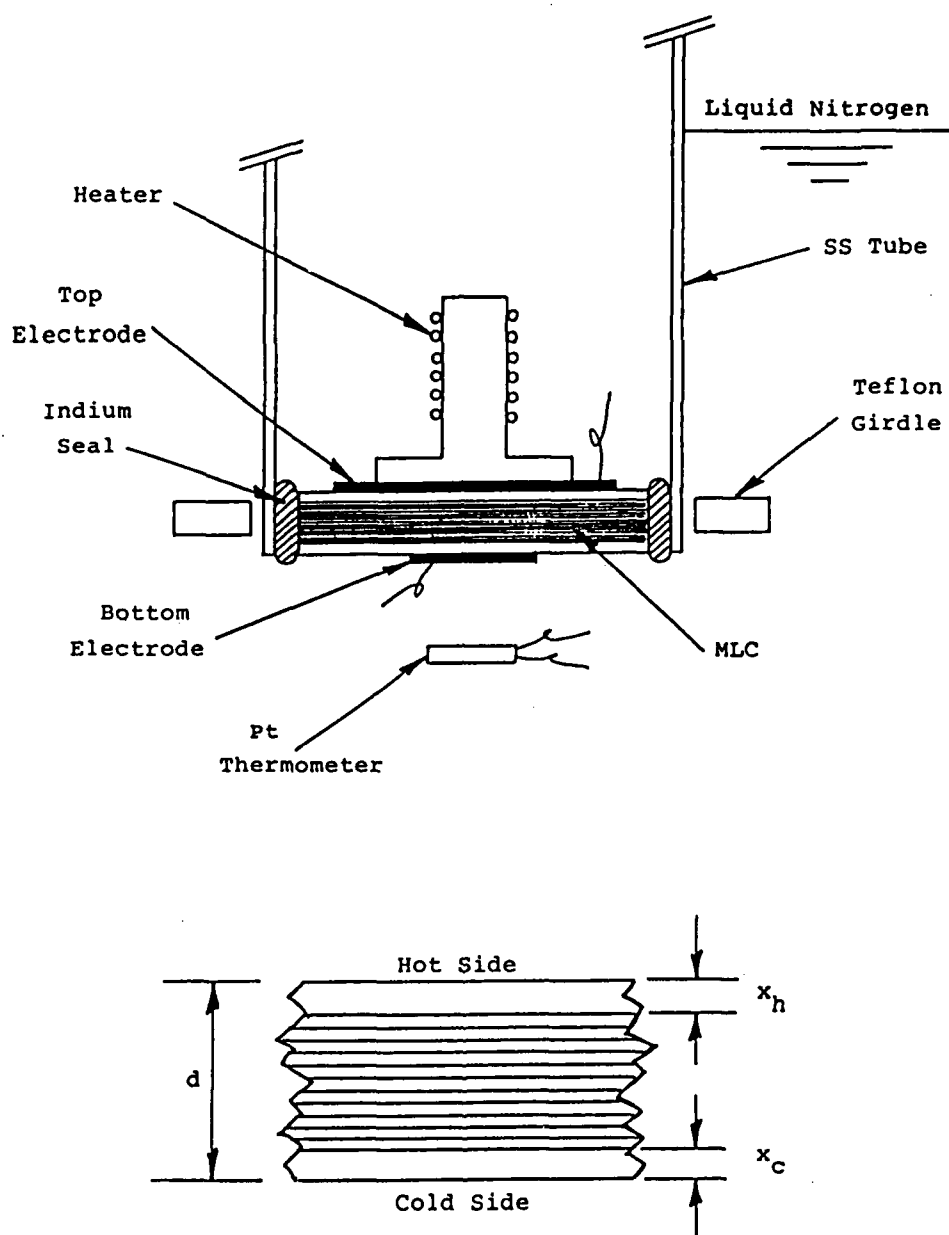Figure III-16. Schematic drawing of the transverse heat flow experimental arrangement. The upper drawing shows the placement of the MLC in a SS tube, and the lower drawing illustrates the in situ capacitance thermometry employed.

To achieve this, the periphery of the MLC was coated with a fired-on Ag layer, the inside of the tube was tinned, and the assembly was In-soldered in place using a ruby flux, as shown in Fig. III-16. It proved helpful to round the corners of the MLC slightly, and an In-2% Ag alloy gave the best results. A Teflon girdle was placed around the outside of the squared tube, as shown, and at low temperatures this girdle put the indium seal in compression due to the large thermal contraction of Teflon. This Teflon girdle was also used to anchor the leads for the Pt thermometer shown in Fig. III-16, and this in turn served to position this thermometer in the liquid nitrogen about 2 cm from the solid-liquid interface.

The other end of the stainless-steel tube was soldered to a copper tee which allowed the fixture to be evacuated and which also accommodated electrical feedthroughs.

Second, the surface temperature was measured by a simple but elegant technique. Namely, since the CPN17 ceramic has a strong $\varepsilon(T)$ dependence, the cover plates of the MLC form two capacitance thermometers. Note that in the step above of firing Ag on the periphery of the MLC, all the embedded electrodes are shorted together, but this in fact is desirable in order to form the two capacitance thermometers. Thus, referring to Fig. III-16, a measurement of the capacitance between the Top Electrode and the tube measures the "hot" thermometer, between the Bottom Electrode and the tube, the "cold" thermometer. Three-terminal, coaxial, capacitance measurements were made in these experiments, corrected for the lead capacitances.

Strictly speaking, these capacitance measurements correspond to temperatures at the midpoints of the cover plates. However, as shown in the lower drawing of Fig. III-16, knowing the MLC dimensions L, x_h, and x_c easily allows the extrapolation of the surface temperatures using the measured, linear temperature gradient at steady state. The experimental quantities of interest here are the temperature difference between the "cold" MLC surface and the liquid-nitrogen temperature, ΔT, and the heat flux, $\dot{Q}/A$, where $\dot{Q}$ is the heater power and A is the MLC surface

area (see below). Note here that the Pt thermometer measures the liquid-nitrogen temperature well removed from the solid-liquid interface (to account for diurnal changes), and the capacitances of <u>both</u> cover plates are needed to extrapolate the "cold" surface temperature.

The Top and Bottom Electrodes in Fig. III-16 were also formed using fired-on Ag paste, and the heater post was In-soldered to the Top Electrode. For the Bottom Electrode, <u>two</u> cases were investigated -- a very small area (0.073 cm^2) and a very large area (0.49 cm^2) Bottom Electrode. The reason for this was to see if the heat transfer between the MLC and the liquid nitrogen was influenced by the Ag coating.

The experimental procedure here was as follows, referring to Fig. III-16: First, the assembly was evacuated at room temperature and leak-checked. Next, the end of the tube containing the MLC was immersed in liquid nitrogen, and, after stability was achieved, the two capacitance thermometers and the Pt thermometer were measured -- this step calibrated the capacitance thermometers (see below). Then, each datum consisted of activating the heater and measuring the three thermometers at steady state. The apparatus was pumped on continuously with the leak detector during the measurements.

The Heater in Fig. III-16 was a 60-Ω wrap of 0.36 Ω/cm manganin wire, 0.13-mm diam, and with the Hewlett-Packard power supplies available a maximum power of about 15 W could be reached. Copper lead wires, heat sunk at 77 K, were used to connect the heater so that all the heat generated in the heater was dissipated through the MLC. The power $\dot{Q}$ was determined by measuring the heater current and the voltage drop across the heater.

The MLC chosen for these measurements was a 46-layer device, $1.001 \times 0.996 \times 0.2692$ cm^3 in outside dimensions. The MLC was checked for consistency by measuring the capacitance at 77 and 300 K and found to be an excellent unit. The cover-plate thicknesses, x_h and x_c in Fig. III-16, were 0.0384 and 0.0389 cm, respec-

tively.

After the heat-flow measurements were completed, the capacitances of the top and bottom cover plates were carefully measured as a function of temperature to provide calibration curves. These calibration curves were run last for two reasons: (1) The heat-flow measurements had to be completed first in order to determine the temperature ranges over which to calibrate the cover plates; and (2) There was always the risk of damaging the MLC during testing, in which case a new unit would have to be used. These capacitance-temperature calibration curves for the two cover plates are shown in Fig. III-17, and we note that the "cold" thermometer had to be calibrated to 101 K, the "hot" thermometer to 300 K.

The in-situ calibrations were performed as follows: At the beginning of the run under zero-power conditions, the cover-plate capacitances and the Pt thermometer were measured, as mentioned above. Next, these fixed-point capacitances were scaled to the respective curves in Fig. III-17 at this fixed point by multiplicative factors. In this fashion, run-to-run variations in the electrode areas were accounted for exactly. All data reductions were performed on a DEC 350 computer.

From the experimental arrangement in Fig. III-16, it is clear that a portion of the heater power flows laterally out of the periphery of the MLC, through the Indium seal and the tube wall, and into the liquid nitrogen bath. This correction was handled as follows. First, the transverse thermal conductivity measured on two CPN17 MLC's is shown in Fig. III-4, and note that in the transverse mode the thermal conductivity is independent of the metal electrodes. The scheme here is to arrive at a correction factor based on these data.

The defining relation here is

$$\dot{Q} = (A/x) \int_{T_c}^{T_h} K dT \tag{III-21}$$

where T_h and T_c are the "hot" and "cold" cover plate temperatures, and, from Fig. III-16, $x = d - (x_c + x_h)/2$, in the experiments
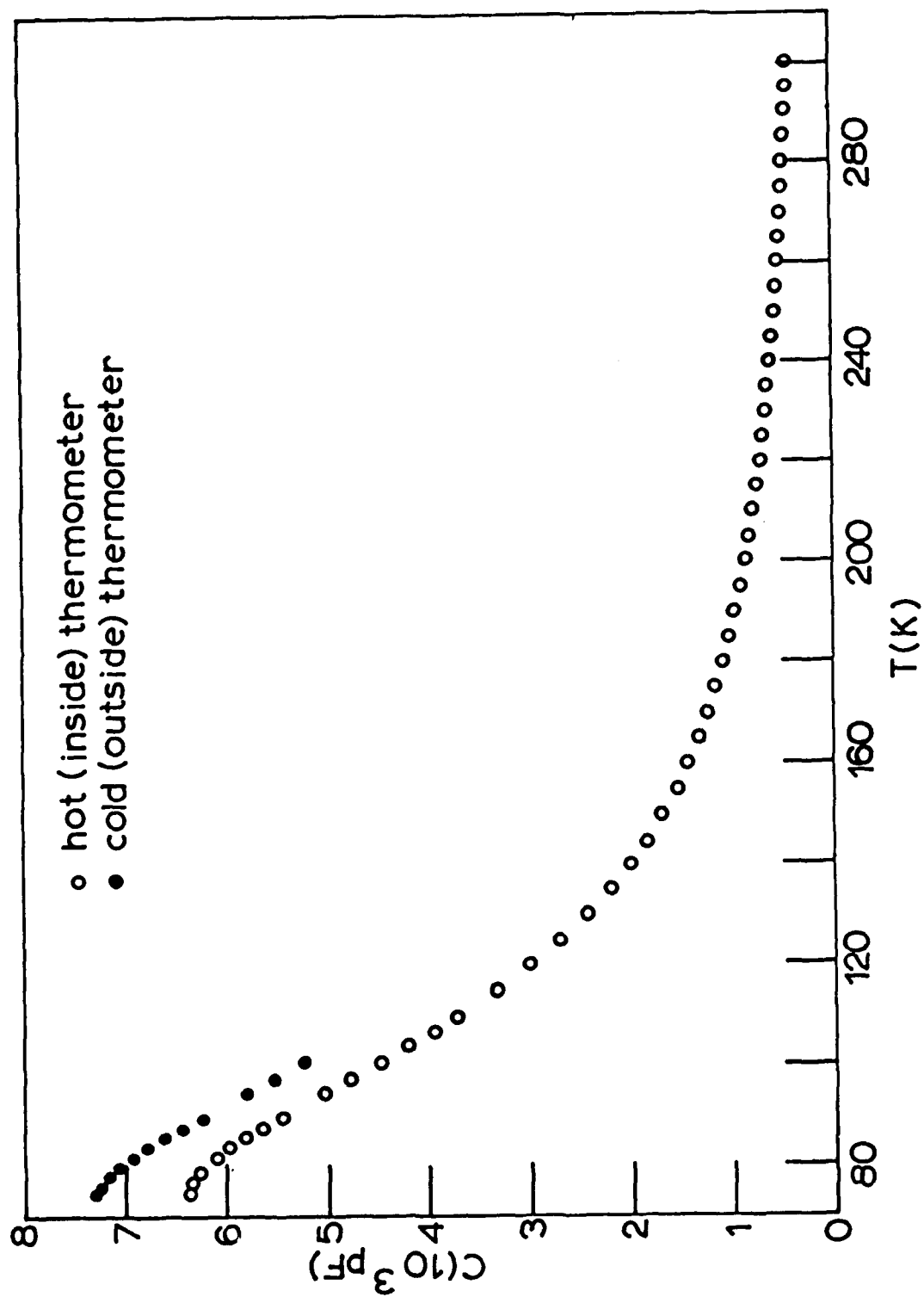
Figure III-17. Calibration curves for the capacitances of the two cover plates of the MLC used for temperature measurements.

o hot (inside) thermometer
● cold (outside) thermometer

$C(10^3 pF)$

$T(K)$

here. The area A in Eq.(III-21) is the _effective_ area of the MCL cold surface through which heat flows, and we write

$$A_{eff} = fA_{act} \qquad\qquad (III-22)$$

where A_{act} is the actual surface area. The factor f in Eq.(III-21) corrects for the heat lost laterally in the experiment, and we expect $f > 1$. To see this another way, we could equivalently correct the _power_ by writing $\dot{Q}/f$ -- less power flows out of A_{act} because of the lateral heat loss.

The (mean) data in Fig. III-4 follow the relation

$$K = mT + b \quad (mW\ cm^{-1}\ K^{-1})$$
$$m = 0.1336,\ b = -1.2682, \qquad\qquad (III-23)$$

and we find from Eqs.(III-21) and (III-22) that

$$f = \dot{Q}[d-(x_c+x_h)/2]/A_{act}[m(T_h^2-T_c^2)+b(T_h-T_c)]. \qquad (III-23)$$

To apply Eq.(III-24) in our experiments here, data for $\dot{Q}$, T_h, and T_c at the lowest _power_ levels are used because the data in Fig. III-4 were measured under very low powers ($\sim$ 2-10 mW). Note here that T_h and T_c in Eq.(III-24) are cover plate temperatures, not surface temperatures.

The assumption here is that the correction factor f determined at low power levels is applicable at _all_ power levels. This assumption, while necessary, is also plausible.

As mentioned above, two runs were made with a small area (0.073 cm^2) and a large area (0.49 cm^2) silvered Bottom Electrode. The respective f-factors for these runs were 1.28 and 1.35, and these factors are slightly different due to slight differences in the In seal between the two runs (note that the assembly in Fig. III-16 was taken apart between the two runs, then reassembled).

The results of these two runs are shown in Fig. III-18 where ΔT is plotted vs. $\dot{Q}/fA$, the actual heat flux through the MLC face
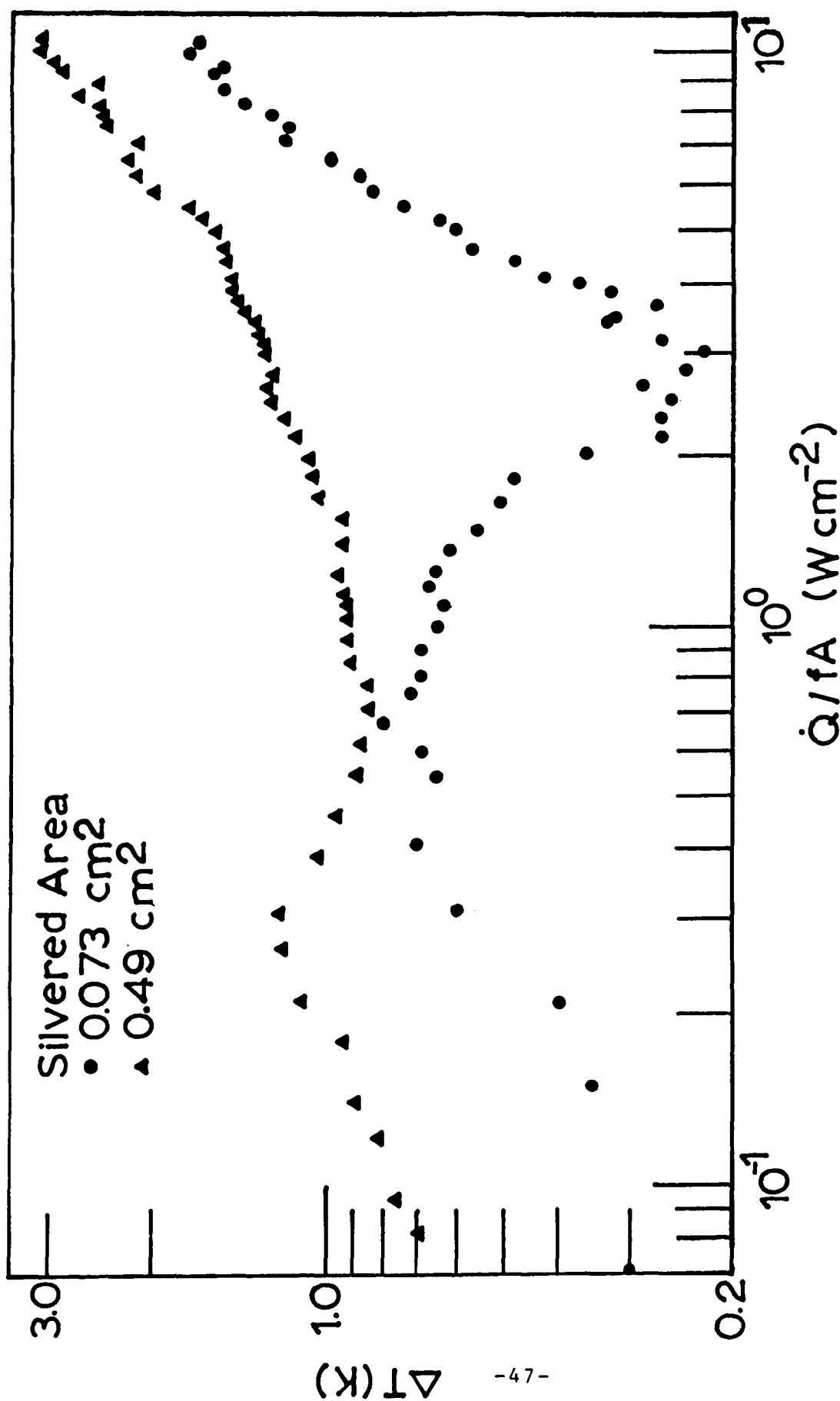
Figure III-18. Results of transverse heat flow experiments between CPN17 and liquid nitrogen. Here, ΔT is the difference in temperature between the ceramic surface and the nitrogen bath for a heat flux $\dot{Q}/fA$.

-47-

into the liquid nitrogen.

The Fig. III-18 data show several interesting features. First, and most importantly, the interfacial ΔT's are very small, $<\sim 3$ K at 10 W cm^{-2}. This result, which was unexpected, depends critically on the calibrations in Fig. III-17 and on the MLC dimensions given above. Additional calibration curves were measured which resulted in somewhat lower ΔT's than those shown in Fig. III-18, so we have high confidence in these results. Note here that ΔT involves the extrapolated surface temperature, and from Fig. III-17, T_c and T_h can be ~ 10 and ~ 200 K hotter than the surface temperature.

The primary finding here is that the thermal boundary resistance between the CPN17 MLC and liquid nitrogen is a surprisingly small effect which can be safely ignored in computer modelling studies.

The structure seen in Fig. III-18 behaves differently for the small and large silvered areas but has a straightforward explanation. For the small area, ΔT has a deep minimum at $\dot{Q}/fA \simeq 3$ W cm^{-2}, then rises steeply. The explanation here is that this small area acts like a "hot spot" for concentrating the heat flow into the liquid nitrogen, and nucleate boiling occurs at this spot which greatly enhances the heat transfer and thereby diminishes ΔT. This result, which is independent of the thermometer calibrations, has some practical applications; namely, fi.'ng small silver dots on the MLC faces for a storage bank will improve the heat transfer.

The data in Fig. III-18 for the large silvered area do not show the minimum in ΔT for a simple reason: nucleate boiling was not achieved.

In conclusion, it has been shown experimentally here that the solid-liquid interfacial ΔT is $\lesssim 3$ K ($\lesssim 1$ K if silver dots are used), and this means that the thermal boundary resistance can be safely ignored in modelling the transverse heat flow from the MLC to the liquid-nitrogen bath. This in turn greatly simplifies the transverse modelling problem, which we consider next.

Transverse Heat Flow - Computer Modelling

As discussed above and presented in the Appendix, the problem of heat flow in two regions with thermal conductivities κ_1 and κ_2 has been solved mathematically and a computer code written. The model here is shown in Fig. III-7, and for longitudinal heat flow, $\lambda = \frac{1}{2}L - t_p$ from Fig. III-6. For transverse heat flow, $\lambda = \frac{1}{2}d - t_{cp}$.

The transverse heat-flow problem is a two region problem because heat is generated in the electroded central region of the MLC (region 1) and flows through the cover plate (region 2) into the liquid nitrogen. Note that if a non-negligible thermal boundary resistance were involved, then a three-region problem would be involved.

Referring to Fig. III-6, there is a practical relation between d and t_{cp}. Namely, the cover plate is usually 2-3 tape thicknesses, and the electroded region is constructed from the same tapes. Therefore, taking a typical MLC with about 50 active layers, we have $\frac{1}{2}d \sim 28$ layers, so that $\frac{1}{2}d/t_{cp} \sim 28/3$. This relation removes t_{cp} as a variable parameter.

The existing computer code can be used here by simply setting $\kappa_1 = \kappa_2$. In practice, however, it was found that setting $\kappa_1 = \kappa_2$ caused the eigenvalue subroutine to seek solutions on the asymptote, and this problem was circumvented by setting $\kappa_1/\kappa_2 = 0.995$ (note that the experimental thermal conductivity data have an uncertainty $\sim \pm 5\%$).

As in the longitudinal case we select thermal properties at 87 K, from Eq.(III-18),

$$\kappa = 10.36 \text{ mW cm}^{-1} \text{ K}^{-1}$$
$$C = 0.173 \text{ J g}^{-1} \text{ K}^{-1}$$
$$\rho = 6.2 \text{ g cm}^{-3},$$

and for the total heat to be dissipated we again use Eq.(III-17),

$$U\tau = 21.48 \text{ J cm}^{-3}$$

where U is the power density and τ is the charging time. The condition and $\Delta T = 20$ K is selected, as before (hence the thermal properties at 87 K are used). In the computer modelling we are interested in the effects of changes in d, τ, and U, and only the centerline temperature of the MLC (i.e, at $\frac{1}{2}$d) is computed since this is the last point to cool back to the bath temperature.

We first examine the case of varying d for a fast pulse, $\tau =$ 20 ms, and these data are shown in Fig. III-19 for 0.2 < d < 1.0 cm.

The Fig. III-19 data show that the centerline-cooldown time varies as d^2, as might be expected on general grounds. These data also show that for d greater than about 0.6 cm, the cooldown times are about 20 s or longer, equivalent to the longitudinal heat-flow case. We also note in Fig. III-19 that for the rapid τ = 20 ms pulse, the centerline temperature reaches $\Delta T = 20$ K, the adiabatic limit (i.e., edge effects are not felt at the center-line).

The Fig. III-19 data demonstrate rapid centerline-cooldown times for d < 0.4 cm, and these two cases are shown in more detail in Fig. III-20. We note in particular that the centerline cools to 78 K (i.e., 0.6 K above the bath temperature) in about 1.5 and 6.2 s for d = 0.2 and 0.4 cm, respectively, again illus-trating an approximate d^2 dependence.

Also shown in Fig. III-20 are cooldown data for the longi-tudinal case with quadruple Pt electrodes under the same condi-tions, and here the cooldown time to 78 K is about 10 sec. Recall in this regard that Pt electrodes have large thermal conductivities, and quadruple layers represent a rather extreme case of promoting a large longitudinal thermal conductance.

One must also keep in mind the heat flux out of the MLC faces into the liquid nitrogen bath. In our example here, an amount of energy 21.48 LWd is (instanaeously) stored in the MLC and then flows into the bath through the two faces of area LW in a time ΔT. Thus, for the d = 0.2 cm case in Fig. III-20 with Δt $\simeq$ 1.5 s, the heat flux through each of the two faces is $\simeq$ 1.4 W cm^{-2}. This is a relatively modest heat flux and shows that rapid

TRANSVERSE HEAT FLOW

$\tau = 0.02$ s, $U = 1074$ J cm^{-3} s^{-1}

- ·   d = 0.2 cm
- +   d = 0.4 cm
- *   d = 0.6 cm
- o   d = 0.8 cm
- x   d = 1.0 cm

Time (s)

Centerline Temperature (K)
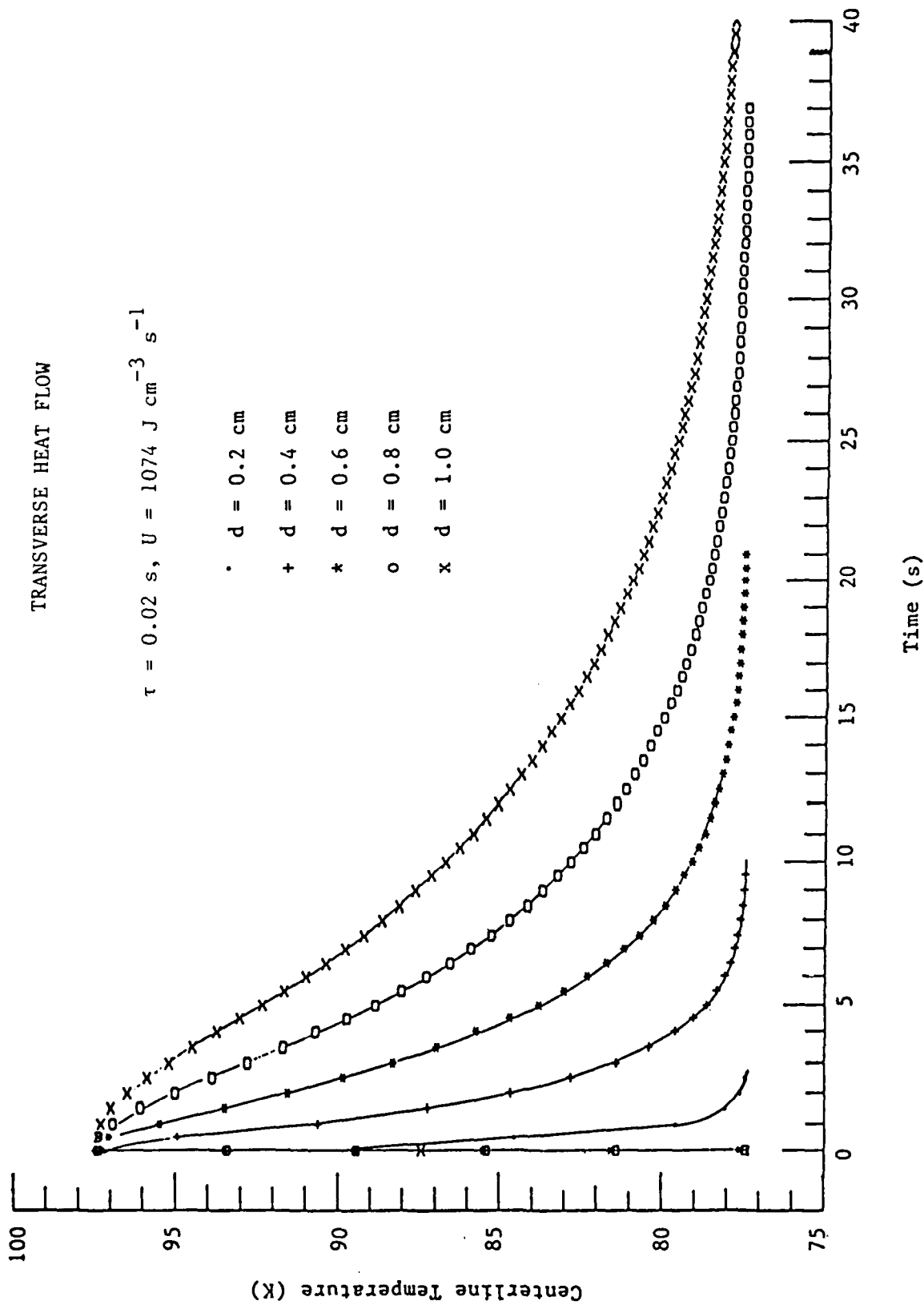
Figure III-19.   Centerline cooldown time for various MLC thicknesses d in the transverse heat-flow mode.
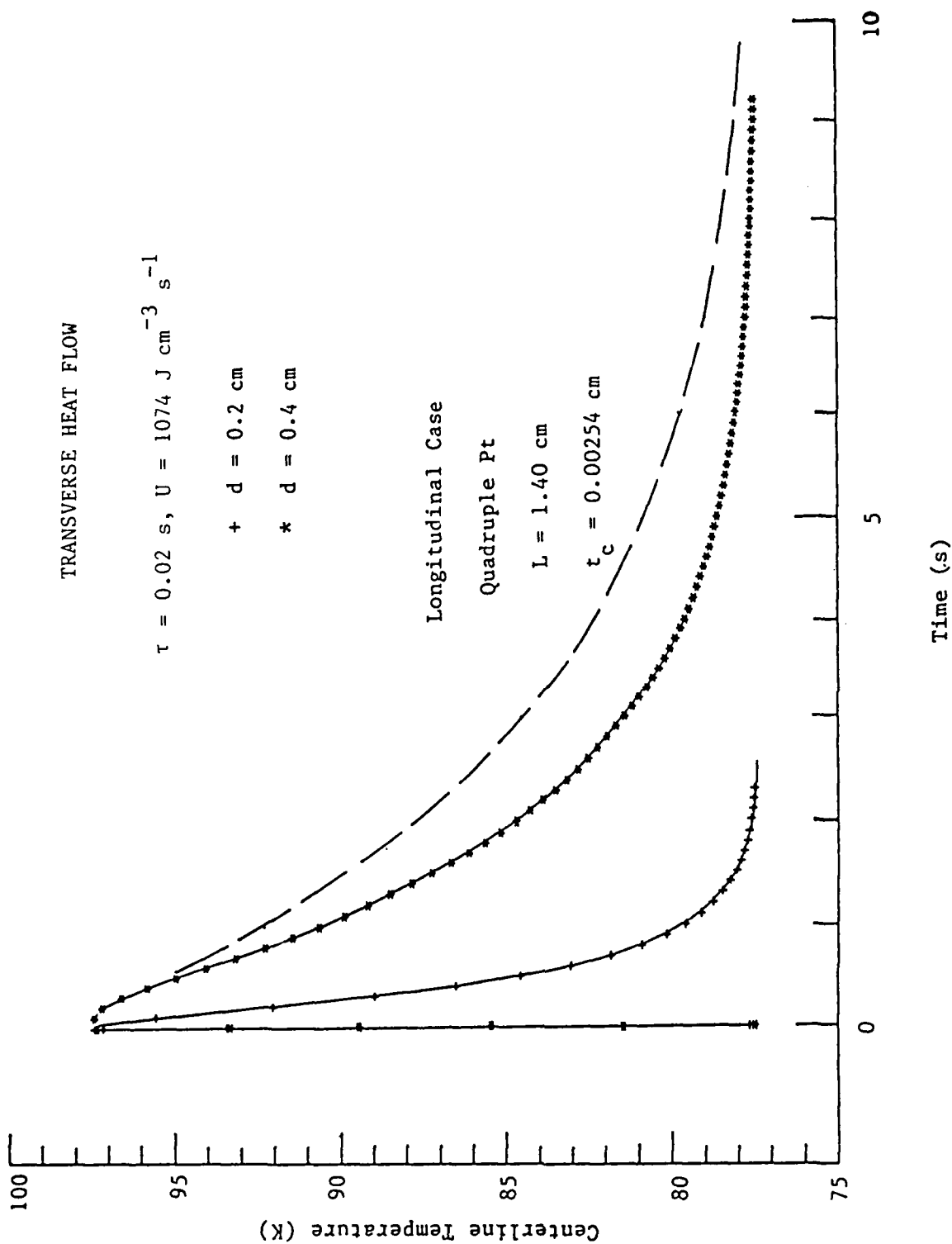
Figure III-20. Expanded curves for d = 0.2 and 0.4 cm, taken from Fig. III-19. Also shown for comparison is the fastest longitudinal case taken from Fig. III-11.

cooldowns (~ s) do not translate into uncomfortably large heat fluxes for the $U\tau$ example here. We shall return to these considerations below.

Next, we examine variations in U and τ, and here we arbitrarily select d = 0.50 cm as our reference case. Computed centerline-cooldown data are shown in Fig. III-21 for variable U and in Fig. III-22 for variable τ but holding τU constant in the latter case.

In Fig. III-21, the product τU varies from 1.07 to 21.48 J cm^{-3} for the fast-pulse condition, and the cooldown time to 78 K varies from 2.0 to 10 s, respectively. At τU = 10.74 J cm^{-3}, the cooldown time is 8.2 s. These findings reveal an interesting

$$\Delta t \propto (\tau U)^{\frac{1}{2}}$$

relation for the fast-pulse condition, and this has important ramifications for the duty cycle which can be taken as Δt, the cooldown time to 78 K.

In Fig. III-22 we examine the case of <u>long</u> pulse times, τ = 0.2, 1.0, and 5.0 s, holding the total energy density constant. Two interesting features are seen in Fig. III-22. First, for τ < 0.2 s, edge effects are not seen at the centerline (i.e., the centerline temperature reaches 97.4 K, ΔT = 20 K). And second, for τ = 5.0 s the centerline heats only to 88 K (i.e., $\Delta T \simeq$ 11 K), and the subsequent cooldown to 78 K following the pulse requires 7.5 s. This is to be compared with 10 s for the rapid, τ < 0.2 s pulse.

Discussion and Conclusions

A systematic examination of the thermal duty cycle of CPN17 MLC's has been presented in this section, and all computer-modelling studies have been based upon experimental measurements also reported in this section.

In these computer modelling studies, we have treated the two cases of longitudinal and transverse heat flows separately but evenhandedly (i.e., same parameter values and ranges).

TRANSVERSE HEAT FLOW

$\tau = 0.02$ s, $d = 0.50$ cm

. $U = 1074$ J cm^{-3} s^{-1}
+ $U = 537$
* $U = 53.7$

Centerline Temperature (K)
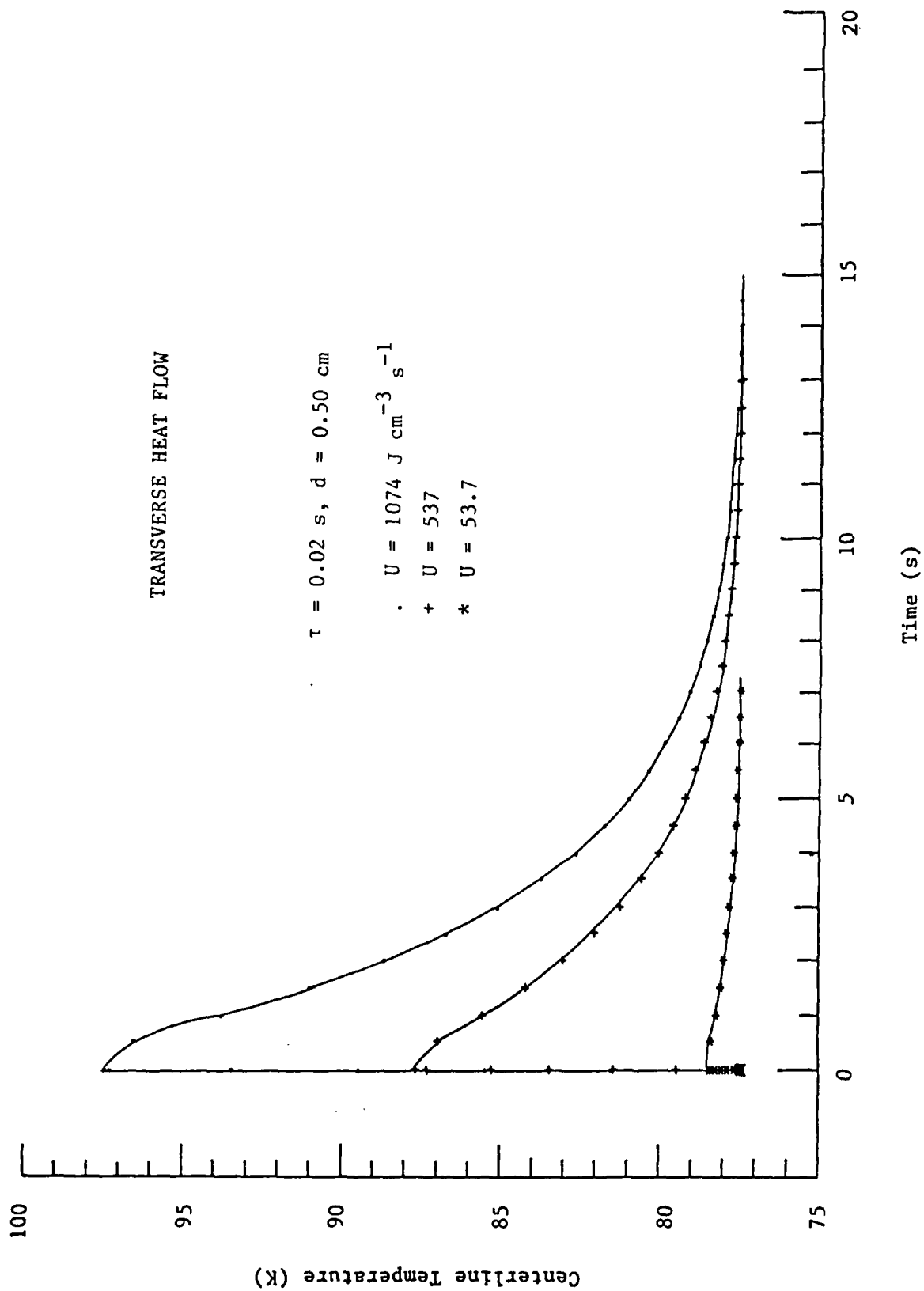
Time (s)

Figure III-21. Centerline cooldown times for various power densities, U, for the transverse heat-flow mode.

TRANSVERSE HEAT FLOW

d = 0.50 cm

$\tau = 0.2$ s, U = 107.4 J cm^{-3} s^{-1}

. $\tau = 0.2$ s, U = 107.4 J cm^{-3} s^{-1}
+ $\tau = 1.0$, U = 21.48
* $\tau = 5.0$, U = 4.30

Time (s)

Centerline Temperature (K)
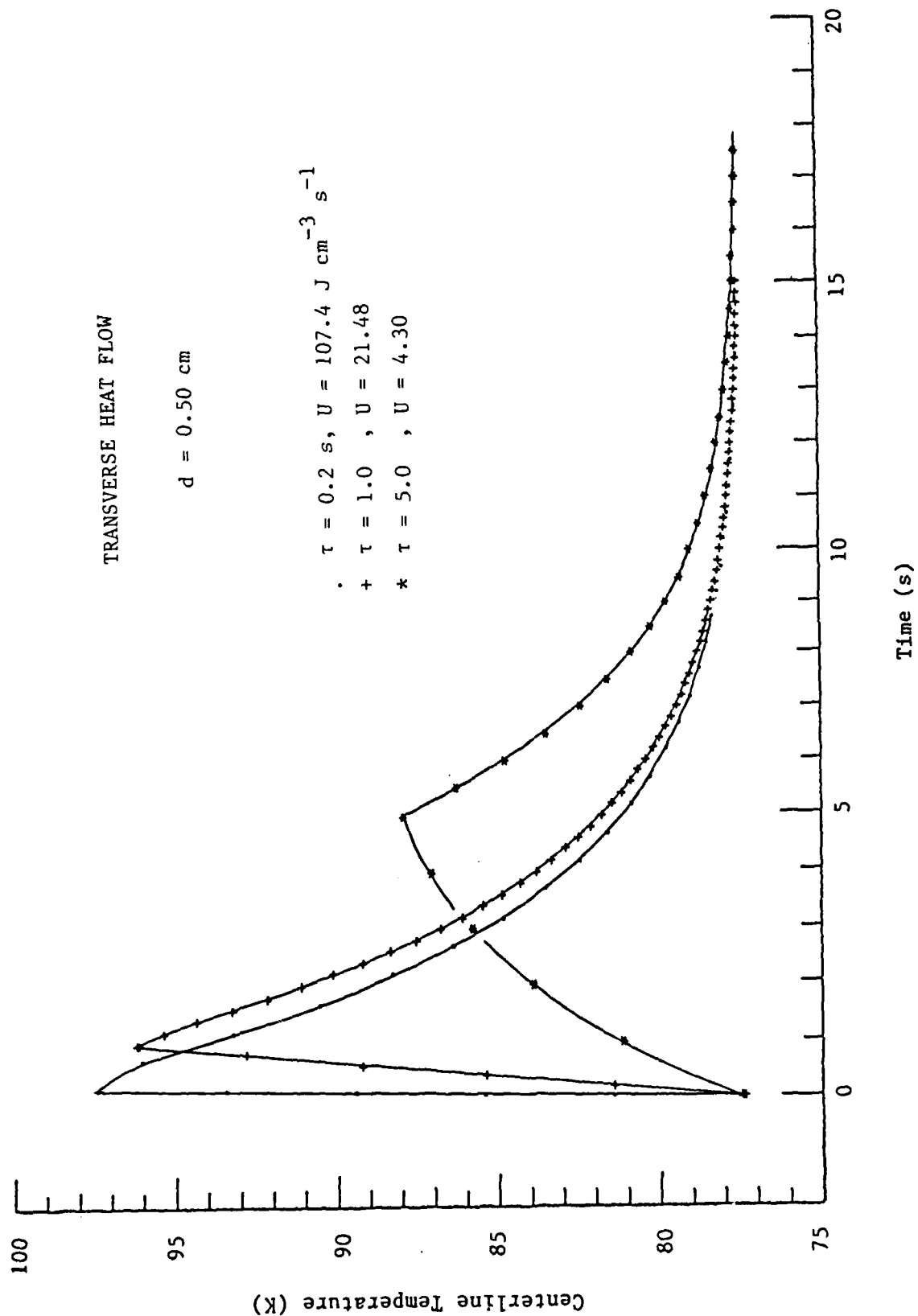
Figure III-22. Centerline cooldown times for various pulse times τ (holding the product τU constant) for the transverse heat-flow mode.

The clear conclusion here is that the <u>transverse</u> case is far more effective in cooling the centerline temperature, and this is best seen in the comparative plots in Fig. III-20.

The duty cycle can be taken as the time required for the centerline temperature to cool down to 78 K, and for the case of $d = 0.2$ cm (~ 79 mil) the duty cycle can be about 1.5 s. This compares with $\Delta t > 10$ s in the most favorable longitudinal case. Thus, the transverse case offers about an order of magnitude improvement in the duty cycle compared to the longitudinal case, and this result depends on the unexpected experimental finding that the solid-liquid thermal resistance is negligible at large heat fluxes.

Two pulse regimes are identified: Fast ($\tau < 0.2$ s) and slow ($\tau > 0.2$ s) pulses. For fast pulses, the centerline temperature heats to the adiabatic limit, and edge effects are not seen. Here, the duty cycle is about 2 s or less. For slow pulses, edge effects influence the centerline temperature and act to reduce the cooldown time. As a general rule of thumb, for slow pulses, $\tau \gtrsim 5$ s, the duty cycle is roughly the same as the pulse time.

The heat flux ϕ from the MLC to the liquid nitrogen bath is an important parameter. Referring to Fig. III-6,

$$\phi \simeq \tau ULWd/LW\Delta t \simeq \tau Ud/\Delta t \propto \tau U/d$$

where we have used the relation $\Delta t \propto d^2$. Thus, large ϕ-values could result from small d-values. However, as we have seen above, even in the fastest Δt-case of $d = 0.2$ cm, the heat flux is modest (~ 1-2 W cm^{-2}).

Finally, we consider the <u>dielectric efficiency</u>, η, given by

$$\eta = (L - 2t_p)(W - 2t_m)(d - 2t_{cp})/LWd \qquad (III-25)$$

from Fig. III-6. For energy-storage purposes, η has to be made as large as possible because the energy-storage rating is based on the gross volume, LWd. Re-arranging Eq.(III-25),

$$\eta = (1 - 2t_p/L)^2 (1 - 2t_{cp}/d), \qquad (III-26)$$

where we have set $L = W$ and $t_p = t_m$. It is much more practical to increase η by increasing L rather than d, since there are limits on d more so than on L, and this hampers the longitudinal heat flow. Thus, it is fortunate that the transverse heat flow dominates. For example, if we assume an MLC with 50 active dielectric layers, each $1\frac{1}{2}$ mil thick, and assume two cover plates on each face, then t_{cp} = 6 mil and d = 69 mil (= 0.175 cm, compare with Fig. III-20). Letting t_p = 20 mil as a reasonable lower limit, the η's calculated from Eq.(6) are given in Table III-1.

Table III-1

Dielectric Efficiencies

L, in.	η, %
0.25	64.9
0.50	77.9
1.0	84.8
1.5	87.2
2.0	88.4
2.5	89.1
∞	92.0

Table III-20 reveals two interesting features: First, for the small L-values needed to promote significant longitudinal heat flow, $\eta \lesssim 78\%$; however, for $L \gtrsim 1.5$ in, $\eta > 87\%$, and a signicant jump in η occurs. Note also that there isn't much point in increasing L beyond about 1.5-2 in (e.g., at L = 2 in., η is 96% of the L = ∞ limit, and at 2.5 in., 97%).

In conclusion, MLC thicknesses d ~ 0.2 cm are not only practical from a fabrication viewpoint but also promote thermal duty cycles ~ 1-2 s. This is a favorable result because it means that the dielectric eficiency need not be compromised.

Although the transverse heat flow dominates, this does not mean that the longitudinal heat flow is insignificant. Rather,

the latter heat flow should be thought of as complementary, and towards this end <u>thick</u> Pt electrodes, <u>small</u> pullbacks, and <u>thin</u> dielectric layers are favored.

IV. Ceramic Processing and Dielectric Testing

The most important aspect of the Phase II contract was attempts to improved the stored energy density as defined by Eq. II-1. In practice, this meant improving the breakdown field, E_b, so that the upper field (E_c) is maximized in the integral of Eq. II-1. Since the stored energy increases as the square of the field, even moderate increases in E_b can lead to significant increases in ΔF.

The philosophy in this research was simple. It was assumed that there was an intrinsic upper limit in field strength where breakdown would occur even if the material were perfect otherwise. It was also assumed that the breakdowns in the MLC's of Phase I were caused for reasons other than reaching this intrinsic limit. The goal then was to approach this limit by investigation of the causes of breakdown. In practice reaching this goal was to be accomplished empirically by making multiple sets of MLC's under various conditions and looking for correlations in the breakdown fields which would provide clues to improve the devices.

American Technical Ceramics was subcontracted to provide expertise and to manufacture MLC's. They in turn subcontracted Biggers Inc. to perform certain processing steps, to perform microstructural evaluations, and to act as a consultant. CeramPhysics, Inc. was to provide overall program co-ordination, perform breakdown studies and dielectric evaluations, and perform duty-cycle tests on a final bank of MLC's.

The simplest way to present the results of the research is in chronological order starting with a detailed review of the breakdown results of Phase I and ending with the results of duty-cycle testing.

A. Phase I Review

Two small groups of MLC's were manufactured during Phase I using the following process. In the first batch, the appropriate

starting chemicals were mixed by wet-milling, and after drying, the powders were calcined at 900°C for 4 hr to form reacted CPN17. The ceramic was then ground to a fine particle size (~ 2 µm), mixed with an organic binder, and cast into a "tape" about 80 µm thick. Sections of this tape, approx. 5 x 5 cm^2, were stacked one on top of another with an electrode pattern silk-screened on each section. The electrode paste contained 40% Pt, 40% Au, and 20% Pd, and three cover sheets were left on the bottom and top of the stack.

The stack was next taken through a slow binder-burnout step at 400°C for 24hr. to remove the organic binders in the tape sections and electrode paste (these binders are designed to burn out cleanly). Finally, the stack was sintered at 1225°C for 1 hr., and in this step the reacted CPN17 powders sinter and fuse together to form a dense, monolithic plate. The individual MLC's are then cut from the plate with a diamond saw. Twelve MLC's of CPN17 were fabricated in this fashion. The MLC dimensions achieved were 0.99 x 0.99 x 0.20 cm^3, and the dielectric thicknesses were 45 µm (.0018 in.).

The densities of these MLC's were somewhat smaller (6.2 - 6.4 gm/cm^3) than the theoretical density of CPN17 (6.5 gm/cm^3), and so it was decided to hot-isostatically-press half of the MLC's to see if the density could be improved. Unfortunately, a sheer stress developed during this HIP process which delaminated the six MLC's thus leaving only six MLC's for testing.

In the second batch, finer starting size ceramic powders were used and the final fired tape thickness were smaller (28 µm = 1.1 mils), but otherwise the processing was identical to the first batch.

The average breakdown field of the first batch was 150 kV/cm and the average for the second batch was 260 kV/cm. This latter value corresponds to a stored-energy density of 0.81 J/cm^3 (0.13 J/gm). One device of the second group went into the "switched state" illustrated in Fig. II-3. This was the first instance that this effect was observed. At E = 0, the dielectric constant at 77 K of devices in the first group was ~ 7000, while in the

second group the dielectric constant was ~ 3600. This is the first instance of a large variation in dielectric constant between different batches. As discussed later in this section, the cause is still unknown, nor are there any recognized correlations between these variations and other measurements (such as stored energy density).

In retrospect, the number of batch processing variables which might affect the results is large, and not enough is known about the process that the subcontractor used in order to properly compare these results to subsequent measurements. Even at worst, these results were encouraging and there was reason to believe the energy storage density could be increased.

B. Preliminary Groups of MLC's

After the Phase I contract was finished, additional samples for testing became available from a totally separate program employing CPN17 MLC's as potential electrocaloric cooling devices. Because these MLC's were made using only a few source powder, electrode, and geometry variations, the results of testing these devices helped guide the subsequent testing in the present Phase II contract. The testing results are summarized below. Biggers, Inc. also performed microstructural evaluations of these devices as part of their Phase II subcontract and a summary of their results is given below.

A large number (~ 300) of CPN17 MLC's were fabricated under various conditions of source powders, electrode composition and geometry. The matrix of part variations is shown in Table IV-1, and Table IV-2 gives the sources and analyses of the raw materials. As seen in Table IV-1 four groups of MLC's were prepared wherein both the source of niobia and the electrode composition were varied. Also, three types of dielectric layers were studied: (1) Single this layers (1x1.7); (2) Double thin layers (2x1.7); and (3) Single thick layers (1x4.2) (in mils). Fabrication was by standard tape casting procedures. The samples were fired in a manually controlled SiC furnace. The parts were

-61-

Table IV-1

Fabrication and Switching Data for CPN 17 Multilayers

Group No.	Set No.	Niobia Source	Electrode Comp.	Electrode Count	Diel. Lay. Per Elec.	State Switching?	Fire t $(10^{-3}$ cm)
I	0210	TWC	Pt	20	1	Yes	2.66
I	0211	TWC	Ter	20	1	Yes	2.85
II	0187	TWC	Pt	20	2	No	4.80
II	0188	TWC	Ter	20	2	No	5.00
III	0189	TWC	Pt	35	1	No	5.74
III	0190	TWC	Ter	35	1	No	6.18
V	0219	CS	Ter	35	1	Yes	2.95
VI	0255	SO	Ter	20	1	No	2.77
VII	0256	CO	Ter	20	1	No	2.38

Table IV-2

Semi-Quantitative Chemical Analysis* of Trace Elements in Raw Materials

Matl.	Supplier	Desig.	Lot No.	PPM Concentration									
				Si	Al	Ca	Mg	Fe	Ti	Nb	Ag
CdO	Baker Chem. Co.	R1234	345331	5	ND	2	1	<10	ND	ND	ND
PbO	Hammond Lead Inc.	1004	unk	5	ND	ND	1	10	ND	50	1
Nb$_2$O$_5$	Teledyne Wah Chang	-	138	500	100	50	40	100	30	-	ND
Nb$_2$O$_5$	Cabot Corp.	Stnd.	P-3765-10	NA	NA	NA	NA	NA	NA	NA	NA

*Emission Spectroscopic Analysis by Dr. N. Suhr, Mineral Constitution Laboratory, The Pennsylvania State University.

sealed in Al_2O_3 crucibles packed in sintered CPN17 source powder. The heating rate was ~ 600°C/hr, and the isothermal hold was at 1200°C for 2 hr, followed by furnace cool down with power off.

The surfaces to be terminated were polished on a lap using 15 μm diamond paste to expose the electrodes. The parts were air dried for 1-2 hrs. before applying a silver termination of DuPont 7095 by hand painting. After drying for 1-2 hrs at 100°C, the parts were ramped to 300°C with a 6 hr hold to remove organics, followed by 10 min at 600°C and furnace cool down.

Zero-field dielectric data for these groups is given in Table IV-3. Note that the peak dielectric constant varies over a wide range (6850-12235), but that even within the groups with the same source powder (Groups I,II,III) there is a wide variation, unlike the two groups in Phase I with different source powders. The cause of the dielectric constant variation is unknown, and it does not correlate again to other measured parameters with the exception of Groups VI and VII which had the highest average breakdown fields.

Table IV-3
Zero-Field Dielectric Data

Group	Set	Device	T_c(K)	ϵ_{max}
I	0210	# 2	72.5±0.3	7525
I	0211	2	75.0±0.3	7740
II	0187	12	73.9±0.3	8090
II	0188	11	73.9±0.3	8300
II	0188#2	12	75.9±0.3	6850
III	0189	11	71.8±0.3	9160
III	0190	11	74.7±0.3	8020
V	0219	11	78.8±0.3	7660
VI	0255	26	73.6±0.05	9865
VII	0256	25	69.2±0.1	12235

The average breakdown field at room temperature and at 77 K for each of the groups is shown in Table IV-4. Note that there is no significant difference between the breakdown field at room

temperature and 77 K indicating that breakdowns are not caused by ionic migration nor stresses from the cooling process.

Table IV-4

Summary of Breakdown Field Strengths (kV/cm)

Group	Set	300 K	77 K*
I	0210	249±40	249±27
	0211	201±25	219±36
II	0187	236±37	195±34
	0188	225±33	215±44
	0188#2	235±24	209±31
III	0189	235±38	188±33
	0190	193±20	178±14
V	0219	214±50	222±28
VI	0255	**	337±32
VII	0256	**	298±41
	Mean =	224±19	231±51

* Liquid nitrogen immersion

** Conductive

Examining both Tables IV-1 and IV-4, there is no correlation between breakdown field electrode type. There is a small, but definite, inverse correlation between layer thickness and breakdown field and there is an apparent strong correlation breakdown starting source powders and E_b. Groups VI and VII used optical grade powders and both had significantly larger breakdown fields and peak dielectric constants at zero field. Unfortunately these groups have other anomalies which make them suspect. In particular, even though these groups were made with the highest purity material, they were conductive at room temperature (but not at 77 K) indicating substantial impurity concentrations. These two groups were also processed together, but at a different time from Groups I thru V. Since Groups VI and VII were made from two different starting powders, the initial obvious correlation between large E_b and source powder may not be the correct correlation. The source of all the

anomalies in these two groups remains intriguing but unidentified.

Biggers, Inc. has performed microstructural studies on some of these groups and several conclusions can be drawn from their studies. First there is no obvious correlation between breakdown field and either average grain size or porosity. The measured values for both of these quantities are shown below in Table IV-5. The studies did identify the presence of acicular (needlelike) grains in some groups and the presence of a possible second phase in all groups. SEM photos of both equiaxed and acicular grains are shown in Fig. IV-1 and the presence or absence of these and the second phase are noted in Table IV-5.

Figure IV-1
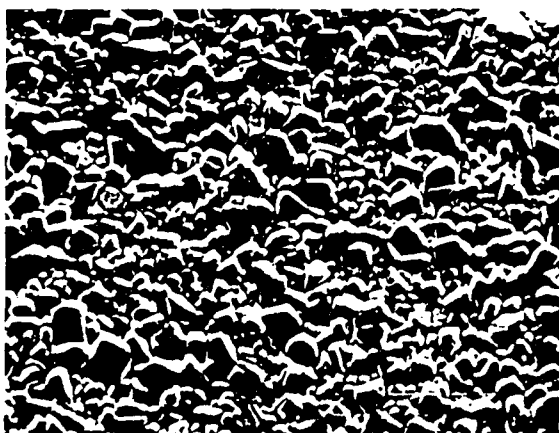
(a)   (b)

Figure 2. (a) Equiaxed grains, Group I-0211, 1000x.
(b) Equiaxed and needle-shaped grains, Group VII, 1000x.

Both of these features are most likely associated with non-stoichiometric processes occurring during sintering. The features do not correlate with E_b, but they do correlate with the presence of state-switching as discussed below.

As breakdown measurements at 77 K were being made on each of the Groups, they were also surveyed for the state-switching phenomenon. Only the thin-layered groups I and V showed the

Table IV-5

Correlation of State Switching and Microstructure

Group-Set	$\bar{D}(\mu m)$[a]	Needles?	Conchoidal Fracture?	Minor Phase[b]	Porosity	State Switching?
I-0210	6.26	No	Yes	0.35%	8.95%	Yes
I-0211	5.88	Yes	No	0.52	10.01	Yes
II-0187	-	-	-	0.86	9.09	No
II-0188	-	-	-	2.57	10.22	No
III-0189	-	-	-	0.90	7.12	No
III-0190	-	-	-	2.61	9.80	No
V-0219	8.70	No	Yes	0.46	13.88	Yes
VI	6.77	Yes	No	4.10	3.74	No
VII	6.92	Yes	Yes	0.89	10.70	No

(a) Average grain size

(b) As volume % of total ceramic

effect. The state-switching phenomenon was repeatedly demonstrated on several MLC's that did not break down dielectrically, and a typical state-switching curve is shown in Fig. IV-2. As seen, ϵ drops with E from ~ 8×10^3 at E = 0 to ~ 200 at E ~ 200 kV/cm. and then ϵ switches onto the upper curve. Once state-switching takes place, the dielectric constant is stable on the upper curve of Fig. IV-2 on field-cycling between E = 0 and 300 kV/cm (or higher) at 77 K.

On comparing Figs. II-3 and IV-2, the present MLC's switch at slightly lower field strengths (~ 210 kV/cm, see below also) than the previous device (~ 250 kV/cm). However, the current devices have $T_c \approx 74$ K compared to $T_c \approx 50$ K for the device in Fig. II-3.

Approximately one-half of the thin-layer MLC's from Groups I and V showed state-switching at ~ 210 kV/cm, and the remaining one-half showed dielectric breakdown at 201-248 kV/cm, all at 77 K. It is highly coincidental that the field strengths here are so close, and we shall return to this point below.

The electric field strengths where state switching was observed are summarized in Table IV-6. The switching field is defined as the median field where ϵ is between the upper and the lower curves (e.g., 217 kV/cm in Fig. IV-2).

As seen in Table IV-6, there is no correlation between the switch fields and the groups of MLC's studied, and there is a wide variation in the switch fields for any one group. This variation is no doubt associated with the extensive porosity. We remark that the state-switching is unmistakable in a capacitance measurement because ϵ jumps by a factor of ~ 20 (e.g., from 200 to 4200 in Fig. IV-2).

The dependence of the dielectric constant on both temperature and electric field was measured on an unswitched device and on a switched device, and these data are shown in Figs. IV-3 and IV-4, respectively. The data in Fig. IV-3 are typical of $\epsilon(T,E,)$ data of unswitched devices and will be discussed more in a later section of this report. The data in Fig. IV-4 is significant because it is the strongest evidence
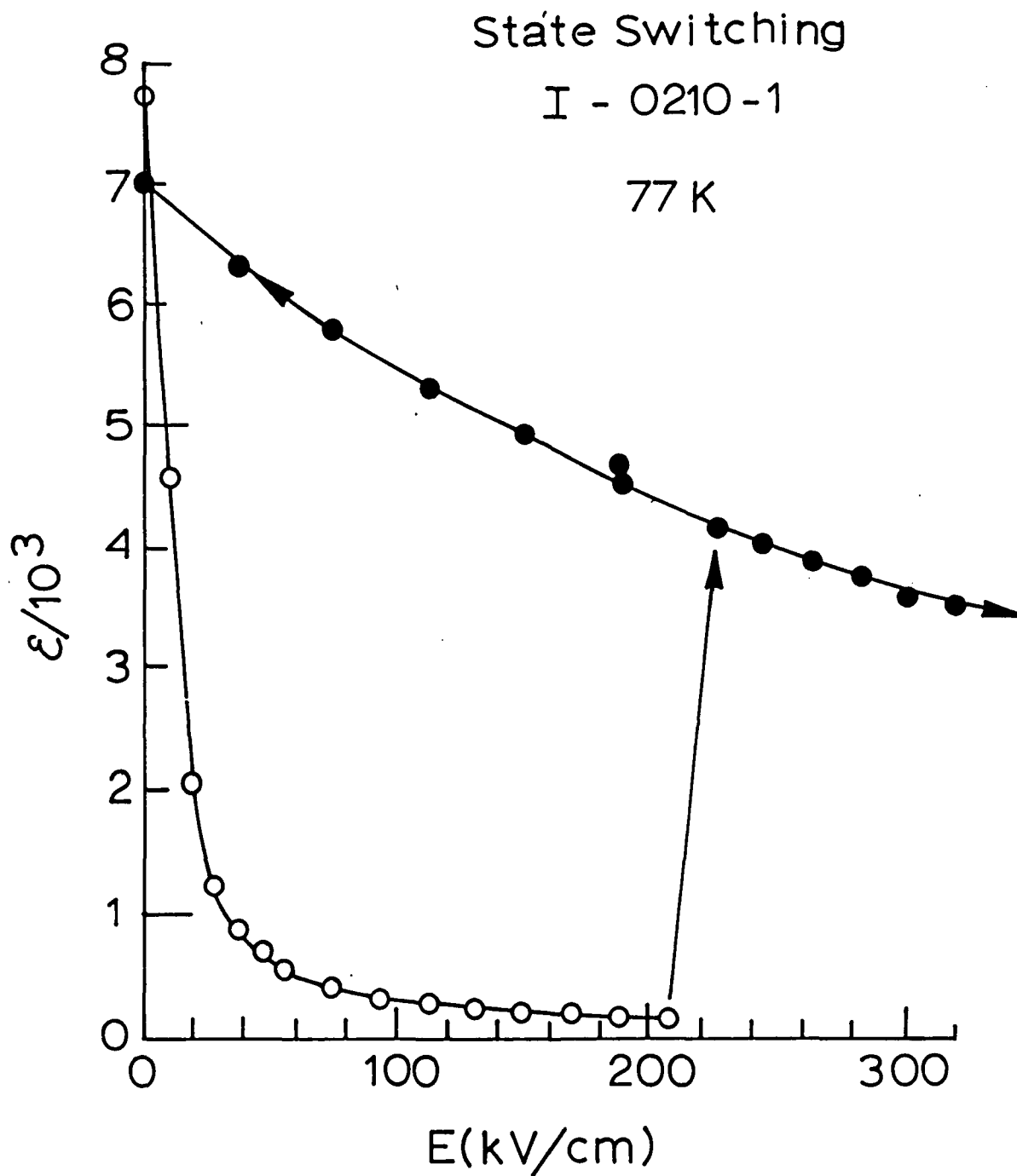
Figure IV-2 State switching characteristic measured
repeatedly on the CPN17 MLC's.

available that the "switched-state" is not due to a partial
breakdown which lowered the applied voltage on the device below
the voltage set on the high-voltage power supply. At the time

Table IV-6

State-Switching Field Strengths at 77 K

MLC	Switch Field, kV/cm
I-0210-1	216
-6	197
-7	240
-16	150
-18	150
I-0211-4	167
-17	167
-22	202
-25	184
V-0219-1	212
-2	246
-11	263
-15	144

Median = 195±39

of these measurements, the voltage across an MLC could not be
measured directly because of the relatively small impedance on
the high voltage scales of the available DVM's. A partial
breakdown is the only instrumental effect which has been proposed
which could account for the switch-state as an artifact rather
than a real event.

The data in Fig. IV-4 was taken by first increasing the
voltage until the device "switched." Then the data was measured
over several hours by stabilizing the temperature at successively
higher temperature points and sweeping through all the field
levels at each point. It is hard to imagine conditions which
would allow a partial breakdown to remain stable for this length
of time and under these conditions.

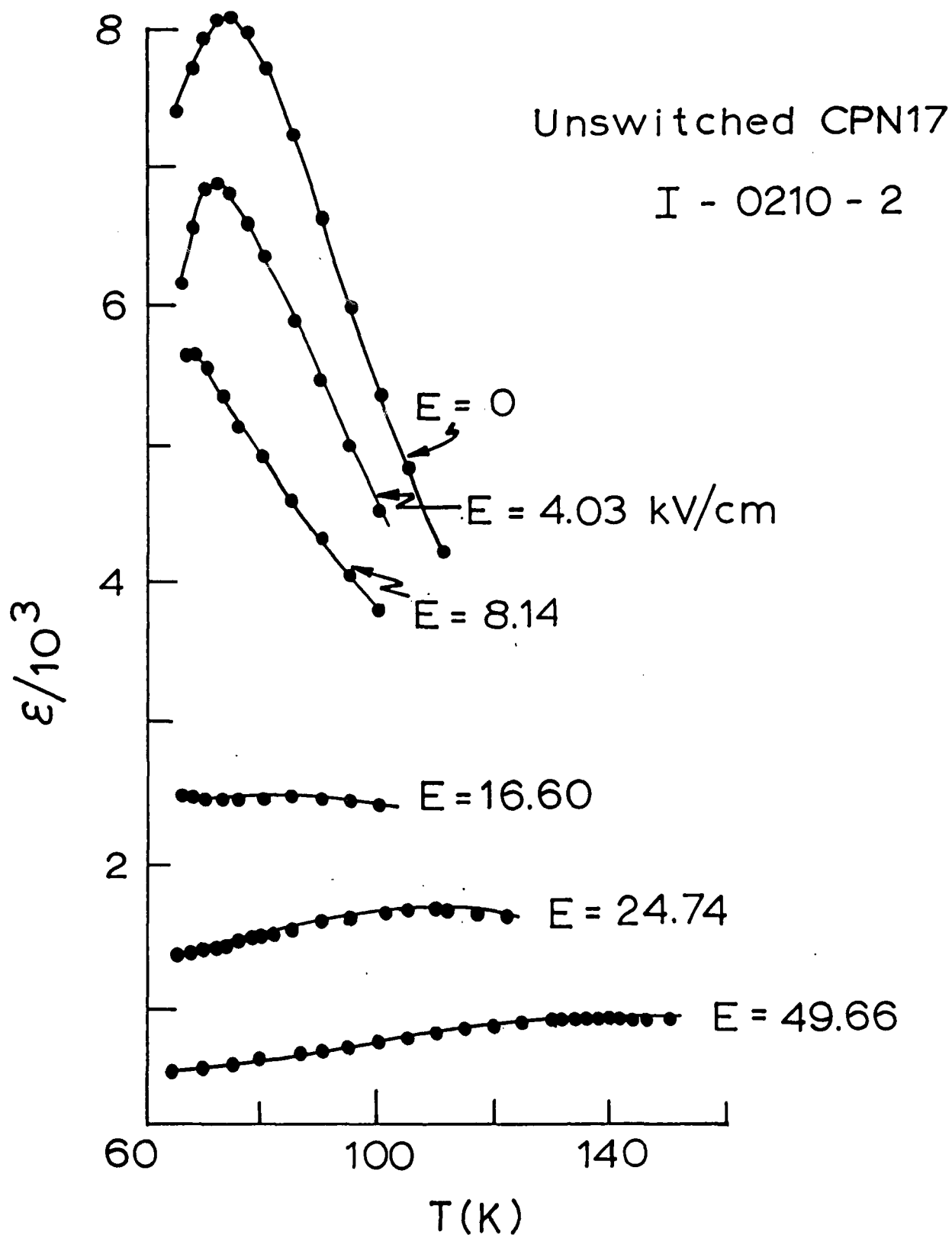There are some strong correlations among these groups

Figure IV-3 Dielectric constant of an unswitched CPN17 MLC as a function of temperature and electric field.
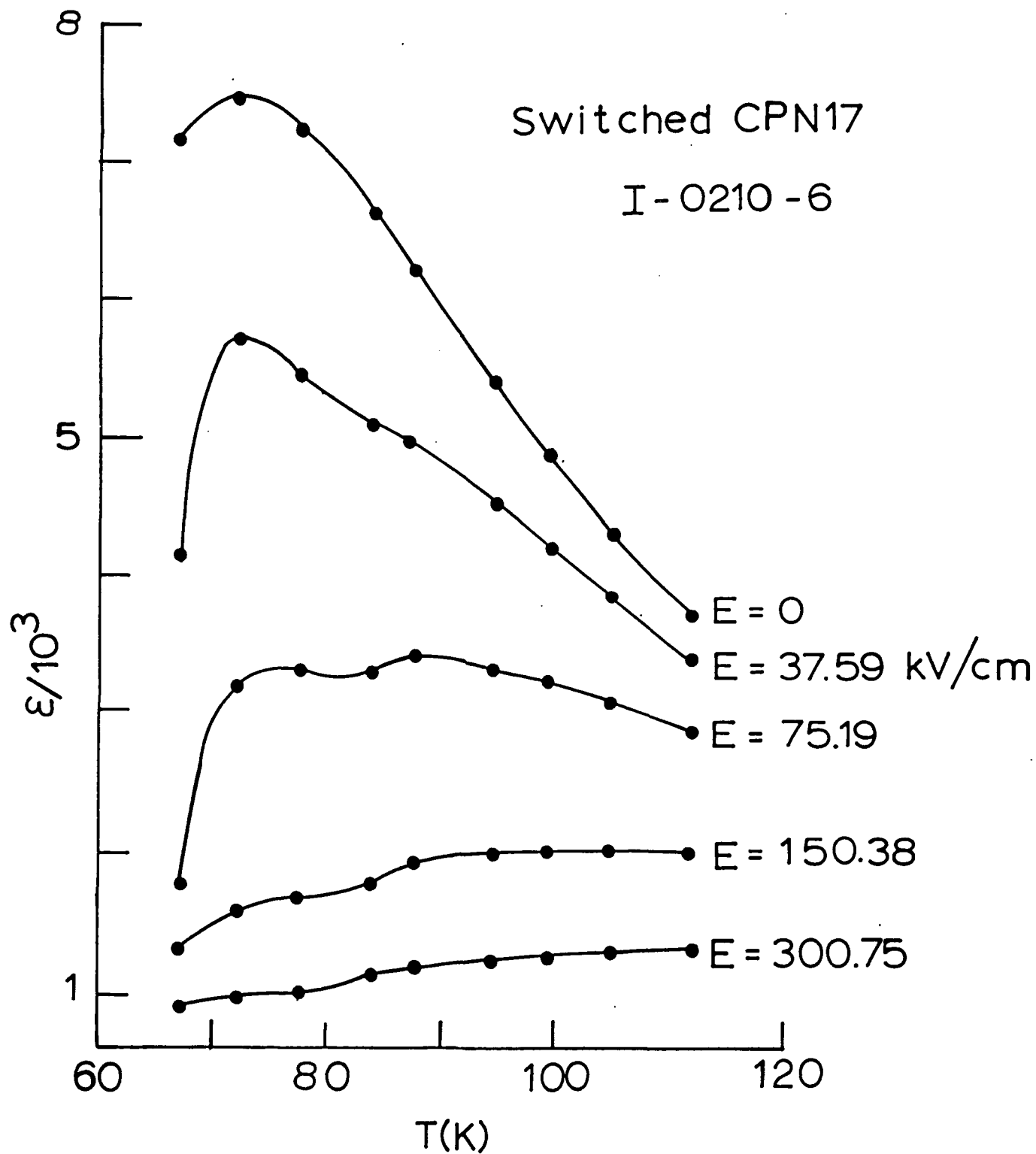
Figure IV-4 Dielectric constant of a switched CPN17 MLC as a function of temperature and electric field.

relating to state-switching. The proximity of the state-switching and breakdown field strengths mentioned above suggests that these two effects are related, and one obvious connection here may be a dimensional change accompanying an induced state change. In this picture, the MLC's that survive a dimensional change exhibit state-switching; those that do not switch fail dielectrically because of the induced stresses caused by clamping in the inactive ceramic.

To pursue this possibility, one looks for correlations with the MLC geometric dimensions, and two dimensional parameters were examined: (1) Ratio of transverse pullback to cover plate thickness ("Pullback/Cover"); and (2) Ratio of active to inactive ceramic areas in the transverse plane ("Area Ratio"). These correlations between Pullback/Cover, Area Ratio, and the occurrence of state-switching are given in Table IV-7.

The data in Table IV-7 reveal some interesting correlations between switching and MLC dimensions: Switching appears to occur if the Pullback/Cover ratio is < 1 and if the Area Ratio is < ~ 0.2. These are not redundant dimensional parameters because the former does not involve the active ceramic material whereas the latter does.

As discussed above, microstructure analyses were made on the MLC's from Groups I through VII. One of the more interesting features to emerge from these analyses was the appearance of needle-shaped grains occurring with equiaxed grains, as illustrated in Fig. IV-1. These SEM photographs were taken on as-fired surfaces. A second unexpected feature in these analyses was the appearance of an unidentified Minor Phase.

The microstructural analyses yield data on the following parameters: average grain size, occurrence of needles and conchoidal fracture, extent of minor phase, and porosity. These data are collected in Table IV-5 and correlated with the occurrence of state-switching.

Judging from Table IV-5 there is no correlation between state-switching and grain size, porosity, or conchoidal fracture. The most interesting correlations in Table IV-5 appear with the

Table IV-7

Correlation of Switching with MLC Dimensions

Group	Set	Pullback/Cover	Area Ratio	State Switching?
I	0210	0.792 ± 0.488	0.211	Yes
I	0211	0.964 ± 0.100	0.186	Yes
II	0187	1.172 ± 0.162	0.310	No
II	0188	1.264 ± 0.249	0.302	No
II	0188#2	1.219 ± 0.480	0.289	No
III	0189	2.886 ± 0.299	0.591	No
III	0190	2.566 ± 0.501	0.550	No
V	0219	1.091 ± 0.021	0.190	Yes
VI		1.258	0.236	No
VII		1.602	0.286	No

occurrence of <u>needles</u> and the extent of the unidentified <u>minor</u> phase.

The correlation between the minor phase and state-switching is particularly striking in Table IV-5: As the extent of the minor phase exceeds ~ 0.5%, state-switching is inhibited. The correlation with the occurrence of needles is not clear cut, but here the minor phase may be associated with needles, as suggested by Biggers, Inc.

There is also a strong but incomplete correlation between dielectric layer thickness and the switched-state as shown in Table IV-1 where the thickness must be less than 30 microns for switching to occur. The exceptions to this correlation are Groups VI and VII. However these two groups did not meet either of the other two geometry correlations and both showed other significant anomalous behavior as discussed above.

All of these correlations contain clues as to the nature of the switched-state, but the clues were not strong enough to reproduce the switched state in MLC's made at a later time. No devices made in Phase II switched, even when more MLC's were made with geometry variations which met the correlation conditions above. If any of the correlations above are meaningful, they are a necessary but not sufficient correlation and the other conditions controlling the "switched-state" are still unknown.

c. <u>Computer Automation of Breakdown and Dielectric Measurements</u>

For all of the measurements above, the dielectric constant as a function of field and temperature was measured by hand, e.g. for a breakdown measurement, a voltage was applied to a sample through the bridge protection circuit described below, after a fixed time the sample capacitance was measured, and the voltage was stepped to the next level. Besides being time-consuming, this method had other drawbacks. Because the DVM's available all had input resistances the order of megohms and the resistors in

bridge protection circuit are nearly the same size, monitoring the sample voltage directly with a DVM actually dropped the voltage significantly. Therefore the voltage was not measured directly, but was assumed to be the voltage indicated on the front panel of the power supply. Another disadvantage was not knowing the breakdown voltage closely because the voltage had to be increased in reasonably large steps for time considerations. For these reasons, an automated measurement system was designed and built.

A block diagram of the system is shown in Fig. IV-5. Not shown on this diagram is a DEC-350 computer which controls the system through an IEEE-488 communications line. There are two basic modes of operation. In the first, the voltage applied to the sample is stepped up in specified steps and the voltage is continuously monitored until either breakdown occurs or until the voltage is steady. In the latter case, the capacitance and final voltage across the device are measured and converted to dielectric constant and electric field, and are graphed on the computer screen. All information is printed out, including the graph at the end of the run. In each run, up to three ranges can be chosen with different voltage steps in each range. The ranges and voltage steps are completely arbitrary and are specified by the experimenter for each device. Since the voltage is continuously monitored, the breakdown voltage can be determined within 1-2 volts.

The second mode uses a single voltage step, but waits only a specified time before the voltage is again stepped. By using small voltage steps and small time intervals, this mode can simulate a fairly uniform, smooth ramp rate. The effective limitations on this rate depend at the upper end on the maximum current output of the power supply (60 milliamps max) and on any time constants in the system. With the bridge protection circuit in Fig. IV-6, the upper effective rate is ~ 5-10 volts/sec. There is no physical limitation on the lower end of ramp rates; it is simply a matter of picking voltage and time steps which approximate a smooth ramp.
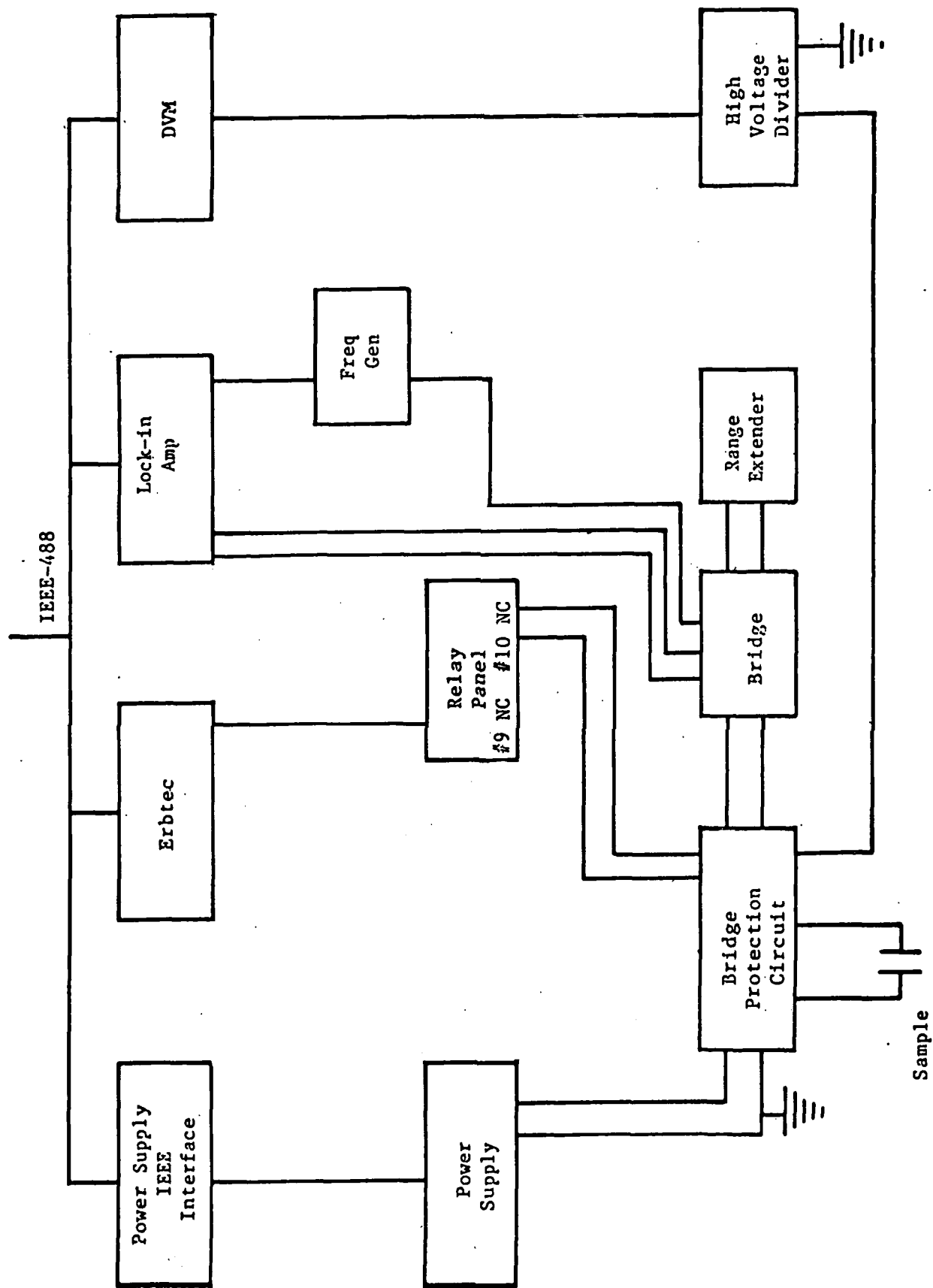
Figure IV-5. Automated Dielectric Constant and Breakdown
Measurement System   -77-

The power supply is a Bertan Model 210-05R (0-5000 Volts) which can be remotely controlled with an analog voltage. This analog signal is provided by a Bertan IEEE interface, Model 200-C488. The voltage across the sample is monitored continuously with a Keithley Model 181 DVM using a 10,000 to 1 voltage divider which allows monitoring of the full voltage range of the power supply while maintaining a large effective input impedance which is especially important considering the large resistors in the bridge protection circuit.

The power supply, capacitance bridge and sample are connected through the bridge protection circuit shown in Fig. IV-6. The large megohm resistors prevent the bridge from "seeing" the power supply. During charging or discharging the switch is closed which prevents any build-up of voltage across the bridge. The 3 μF fixed capacitor (Maxwell Labs, oil-filled) allows a voltage build-up on the sample while preventing current flow through the bridge. During a measurement, the switch is opened. Back-to-back zener diodes on each lead of the bridge provide the primary protection if the sample fails while the switch is open. A fuse provides some current protection redundancy.

The bridge protection switch is controlled through a relay rack which is in turn controlled by an Erbtec Model DIO-64. This instrument is designed as a general purpose computer-controlled set of switches for controlling TTL or relay voltage signals.

The capacitance of the sample is measured by reading the offset signal from the detector output of a General Radio Model 1615-A Capacitance bridge using a Model 1615-P1 Range Extender capacitor (for capacitances in the μF range). The offset signal is measured with a Stanford Research Model SR510 phase-sensitive lock-in amplifier tuned to the pure capacitive signal from the bridge. A table of offset voltage versus capacitance with the bridge at a constant setting has been built into the computer program. The direct capacitance reading is corrected for the presence of the 3 μF capacitor in the bridge protection circuit.

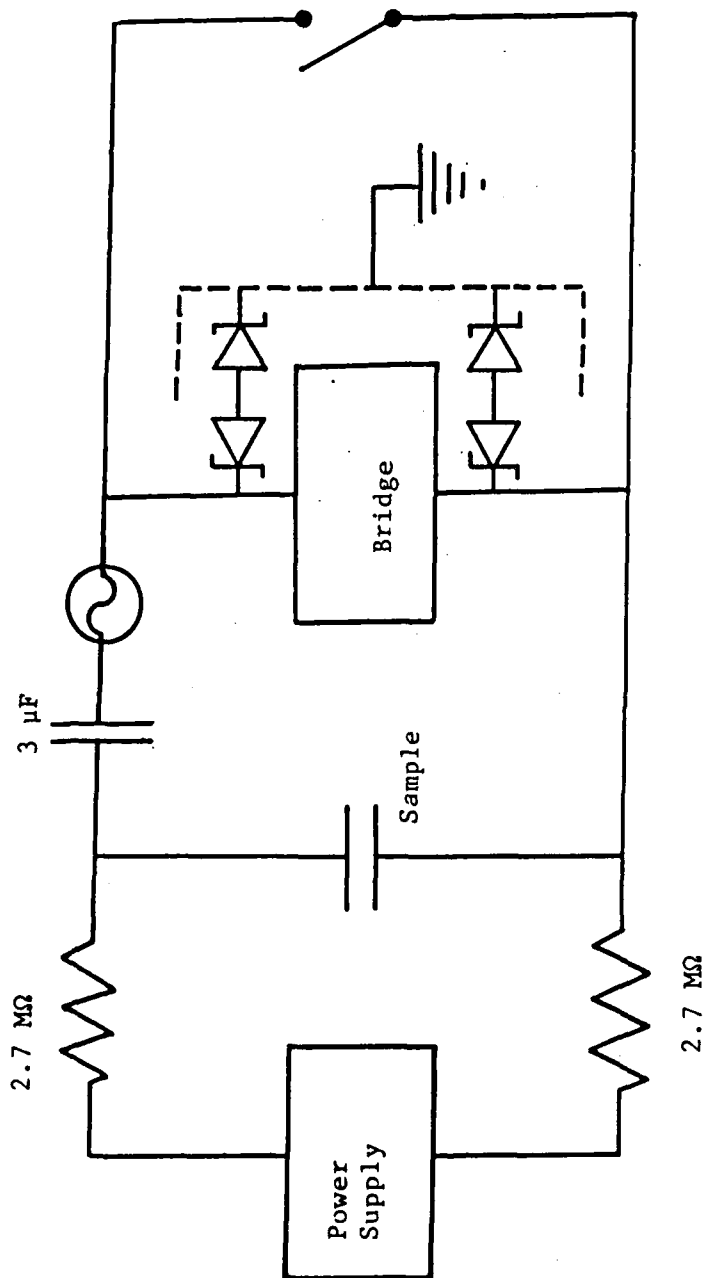The end result is a table of measured capacitances,

Figure IV-6 Bridge Protection Circuit

dielectric constants, voltages and electric fields for each particular device and a graph of dielectric constant versus E-field. If a breakdown occurs, the breakdown (highest voltage) is also printed out. Breakdown is defined as a drop of 10% or more in voltage. The program can alco operate in the step/wait-for-voltage-stability mode and measure only the final breakdown voltage (omitting the dielectric constant measurement). In addition, at each measurement point, the stored energy density is calculated and printed following Eq. II-1 using a trapezoidal numerical approximation for the integration.

D. Initial Phase II Studies

At the beginning of this Phase II contract, very little was known about what mechanisms or effects were causing the breakdown of CPN-17 MLC's. The research proposal was designed to identify as many parameters as possible which might affect breakdown, and by selective variations of these parameters, to maximize the breakdown field. Since there is no literature data on CPN-17, the only guide as to potential parameters which might affect breakdown is experience in ceramic and MLC processing. In writing the research plan in the proposal, there was a heavy reliance on the experience of Dr. Jim Biggers of Pennsylvania State University. It was also recognized at the time of proposal that only a few of the parameter variations would make any difference; it was just not possible to identify these ahead of time.

The preliminary studies described in the previous section did provide some guidelines. Source powders, geometries, microstructure, and porosities were all possible sources of breakdown variations. In addition, electrode geometry and type, composition manipulations (dopants), and process variations were to be considered. Of course, not all of these variations ar independent. For instance porosity can be affected by source

powder, particle size, firing conditions, and HIP'ing among others. Ultimately, the final test of each variation would be breakdown tests at room temperature and 77 K on sets of MLC's. These tests would be correlated with other tests, including microstructural evaluation and insulation resistance (IR) measurements to evaluate results.

The initial tests were designed to evaluate two sets of MLC's. The first set was to be made of $BaTiO_3$-type dielectric composition and was to test multiple layer buildups of dielectric and effects of electrode geometry and materials variations. This material was selected because the materials are cheaper, ATC had experience with the material and because it is a ferroelectric with a peak near 300°C, which made testing easier. The second set was to be T-case CPN-17 MLC's which incorporated a variety of other variations.

The $BaTiO_3$-type dielectric is identified by the ATC code X7R and all the MLC's made from this material were T-case size, which is an ATC designation equivalent to the EIA standard name 1210. There were four types of variations tested: (1) Each dielectric layer was made of either one, two, or three tape layers, (2) Three different electrode materials were tested, Pt, Pd, and 70% Pd/30% Ag, (3) One batch of MLC's with a double thick electrode layer was made, and (4) A batch of MLC's with double width end and side margins were made. All of the variations above were made from a single ceramic batch.

Neither the margin width not the electrode thickness made a difference in the breakdown field. The electrode material tests were inconclusive due to an interaction between the ceramic and the metals. The dielectric thickness did have an effect on the breakdown field strength. In general, the field strength increases as the thickness decreases, agreeing with a correlation noted above in the preliminary set of CPN-17 MLC's. These tests are to be considered of limited value in hindsight because breakdown in the CPN-17 MLC's seems to be primarily dependent on parameters such a processing, which are material dependent.

The set of T-case CPN-17 MLC's were processed and tested in

parallel with the XR7 MLC's. The results of the tests on these MLC's are described below. The processing, processing variations and room temperature testing were performed by Biggers, Inc. The 77 K testing was performed by CPI. In making the CPN-17 MLC's, the microstructural evaluations discussed above forced modifications to the original research plans. In light of these results, it became obvious to Biggers, Inc. staff that the Task 1 work should be modified to stress basic processing studies at the expense of further hot isostatic pressing (which had not proved helpful in Phase I). On this basis, it was decided to modify Task 1-A to incorporate a wider range of raw material candidates and milling schedules with (1) higher raw material reactivities (for finer grained CPN17 powder) and (2) improved slurry chemistry for uniform dispersal of raw materials (to avoid second-phase formation), (3) compare differences between the alcohol-based laboratory milling of early work with the aqueous-based milling which was conducted at ATC, and (4) to compare short and long milling times. These tests were sufficiently varied to prohibit fabrication and testing using MLCs so the various mixes were tested as pellets. Task 1-C was modified only slightly to delete electrode variations in favor of a comparison of termination techniques (prompted by occurrence of extensive termination burnout in Phase I breakdowns) and to include evaluation of insulation resistance (originally specified for Task 1-A).

The testing was started by making multiple pellets (rather than MLC's) of CPN-17 in order to evaluate the optimum ceramic preparation, calcining, and sintering conditions. Raw materials from different manufacturers were selected and characterized for surface area per unit mass, particle size distribution, and impurity concentrations. This latter evaluation was done by emission spectroscopy and all of the powders appeared to be reasonably pure. The optical grade Nb_2O_5, as expected, had lower impurity concentrations than the standard grade.

Milling, calcining, and sintering techniques were all evaluated with the goal of maximizing the fired pellet density.

-82-

In the milling step, Tamol T-901 was selected for the system. Calcining variations were confined to 900°C for 2 hours and 1000°C for 4 hours. A matrix of sintering schedules was examined involving temperature variations from 1110 to 1250°C for times of 30, 60, 120, and 240 minutes. The goal again was to minimize porosity. Selected pellet samples from this last matrix underwent a microstructural analysis to determine grain size and the extent of the second phase found in earlier E-case MLC's. These pellets also underwent a room temperature dielectric evaluation which agreed with measurements on previous CPN-17 samples.

The pellet variations were successful in reducing porosity. The most important factor in improving the fired density of the ceramic was the milling time after the powder is calcined. These samples also showed higher dielectric constant (as would be expected) and lower dielectric loss at room temperature.

The presence of second phase was not well documented in this study perhaps because some difficulty was encountered in etching pellet samples (reason unknown). Second phase was noted only in one powder prepared using Cabot optical grade Nb_2O_5. This is inconsistent with the report on Phase I microstructures which found second phase to be quite common.

Grain size improvements were documented as a function of improved milling of post calcine powder. It was also ascertained that grain size could be controlled by varying the time and temperature of the sintering cycle.

Insulation resistance and breakdown testing could not be performed on pellet samples; however, qualitative evaluation of slurries indicated that exotic raw materials (carbonates and hydroxides) did not yield the expected improvements in raw material dispersion in water-based slurries. It was decided not to include these in Task 1-C parts.

Three tape lots of CPN-17 were made by ATC and processed into T-case MLC's. The lots were supposed to be identical except for the Nb_2O_5 source. Table IV-8 shows the tape designated as 6-1 was equal to the best tape produced in the entire program.

ATC at that point was not keeping tight control and consistency in their batching methods so not all relevant information about the processing is available. The tape labeled 5-3 and 5-4 was older tape made in 1985 and may have lost water before it was processed. There were also some calcining and milling differences among all three tape lots and lots 5-3 and 5-4 were screen-printed under different conditions from lot 6-1. The lack of controls and the large number of variables among these lots hindered evaluation of the importance of different batch processing parameters.

Beyond these problems, the green MLC's groups made from each tape lot were divided into groups to test the effects of other process variations. In particular, the results of two tests are important. First, bisque dicing of the parts was much better than green dicing which produced serious delaminations. Second, silver frit terminations hand-dipped at Biggers, Inc. and terminations applied with automated equipment at ATC were equally good in that they showed none of the burn-marks that occurred after breakdown of Phase I MLC's.

From the studies on pellets, a temperature of 1200°C was chosen as the optimum sintering temperature. Parts from each of the three MLC groups were sintered at this temperature at 30, 120 and 240 minutes. Samples of each subgroup were tested for IR resistance, dielectric constant and breakdown at room temperature and a microstructural study was made of each subgroup.

There was some tendency for the room temperature dielectric constant to peak for parts fired for 120 min. The insulation resistance was always higher at shorter sintering times and was significantly better in the 6-1 groups than in the other two groups. This latter result agrees qualitatively with the results found in the previous E-case MLC's where devices made from Cabot and Stark optical grade Nb_2O_5 were conductive at room temperature. The comparable groups here, 5-3 and 5-4 (see Table IV-8) were not conductive at room temperature, but were still not as good as the 6-1 group which used TWC standard grade Nb_2O_5.

At room temperature there is a slight tendency in the 5-3

Table IV-8 CPN17 T-Case Multilayer Capacitors Green Tape Batching

BI Desig.	ATC Designation Sheet Batch No. Eng. Block No.	Lead Oxide - PbO			Cadmium Oxide - CdO			Niobium Oxide - Nb$_2$O$_5$		
		Source	Grade	Lot	Source	Grade	Lot	Source	Grade	Lot
5-3	5-E-CPN17-003 (86-0164)	Hammond	100Y	1309	Baker	Reag.	343331	Cabot	Opt.	P-3765-10
5-4	5-E-CPN17-004 (86-0166)	Hammond	100Y	1309	Baker	Reag.	343331	Stark	Opt.	S6299
6-1	6-E-CPN17-001 (86-0215)	Hammond	100Y	1309	Baker	Reag.	345331	TWC	Std.	138

Note: All are T-case MLC's with 20 prints. Groups 0164 and 0215 bisque fired 850°C prior to dice at ATC-FL. Group 0166 diced green and burned out at ATC/MRG-SC.

Table IV-9 Breakdown Field Versus 1200°C Firing Time for CPN17,
T-Case Capacitors With Laboratory Terminations

Ceramic Type	Dicing Tech.	Firing Time (min)	N #	Breakdown Field				S.D. %	Ins. Res. at 125°C ohms
				Volts/Mil		KV/cm			
				Mean	S.D.	Mean	S.D.		
5-3	Bisque	30	15	869	69	342	27	8.0	3.2×10^9
		120	15	845	35	333	14	4.2	2.3×10^9
		240	15	813	48	320	19	5.9	1.4×10^9
		Mean	45	842	(28)	332	(11)	(3.3)	2.3×10^9
5-4	Green	30	15	933	34	367	13	3.5	2.8×10^9
		120	14	888	28	350	11	3.1	2.1×10^9
		240	14	888	49	350	19	5.4	1.3×10^9
		Mean	43	903	(26)	356	(10)	(2.9)	2.1×10^9
6-1	Bisque	30	15	1821	368	717	145	20.2	3.2×10^{11}
		120	14	1370	176	539	69	12.8	1.0×10^{11}
		240	15	1156	144	455	57	12.5	6.8×10^{10}
		Mean	44	1449	(339)	570	(134)	(23.4)	1.6×10^{11}

TABLE IV-10 Microstructural Analysis of CPN17, T-Case Capacitors Fired for Various Times at 1200°C

Ceramic Type	Firing Time (min)	Grain Size		Second Phase		Porosity	
		Feat. #	$\overline{D}$ (μm)	Feat. #	Vol. %	Feat. #	Vol. %
5-3	30	276	2.4	15	1.2	71	5.5
	120	218	3.2	14	1.1	21	1.6
	240	118	6.3	22	1.7	28	2.2
	Mean				1.3		3.1
5-4	30	288	3.0	45	3.2	13	0.9
	120	178	4.0	54	3.8	25	1.8
	240	108	6.6	28	2.0	24	1.7
	Mean				3.0		1.3
6-1	30	238	2.6	25	1.9	39	3.0
	120	146	4.1	21	1.6	47	3.5
	240	94	7.6	18	1.3	51	3.6
	Mean				1.6		3.4

and 5-4 MLC's for the shorter sintering time devices to have larger breakdown fields. In the 6-1 MLC's. the average breakdown field improved markedly as the sintering decreased. The mean breakdown field at 30 min sintering time for the 6-1 group was 717 kV/cm compared to 455 at 240 min, and the former value was double the largest breakdown field of any of the 5-3 or 5-4 subgroups as shown in Table IV-9. This huge increase in breakdown field does not correlate with either grain size, the presence of the second phase, or porosity. These values are tabulated in Table IV-10.

Dielectric measurements and breakdown studies at 77 K correlated well with the room temperature studies. There was typically a slight peak in maximum dielectric constant at 120 min sintering time and the MLC's of the 5-3 and 5-4 group had larger peak dielectric constants than MLC's of the 6-1 group. In fact the peak dielectric constant of this latter group was disappointingly low ($\sim$ 5700) at 30 min sintering time. The 6-1 group of MLC's had excellent breakdown characteristics, with the 30 min subgroup being the best by far as shown in Table IV-11.

Table IV-11

T-case MLC's Breakdown Parameters

Group	Total MLC's	$\langle \epsilon \rangle$ at E=0	$\langle E_b \rangle$ (kV/cm)	$\langle \Delta F(max) \rangle$ (J/cm^3)
5-E-003, 30	6	7068	254	0.84
5-E-003, 120	5	8240	232	0.77
5-E-003, 240	5	8170	221	0.71
5-E-004, 30	5	7079	280	0.98
5-E-004, 120	5	7820	252	0.81
5-E-004, 240	6	4493	268	0.56
6-E-001, 30	7	5618	596	2.87
6-E-001, 120	7	7412	298	1.08
6-E-001, 240	7	7502	297	1.04

In this group the average breakdown field was ~ 600 kV/cm and the average stored energy density was 2.9 J/cm^3. One device in this group broke down at over 1000 kV/cm with a stored energy density of 5.8 J/cm^3 (0.89 J/gm).

It is not clear why the MLC's of group 6-1 are so superior to any other previous group. The Nb_2O_5 source powder for this group had somewhat larger impurity concentrations than the other two groups, but this correlation is not consistent with the results for the E-case MLC's studied above. The most important difference with the 6-1 group appears to be in the batch preparation stage where it might have undergone different milling and/or slurry preparation compared to the other two groups. However, this preparation would be expected to show up as a noticeable difference in either grain size, the extent of the second phase, or porosity, and Table IV-10 indicates there was nothing unusual in the 6-1, 30 min subgroup. The last clue is the large difference in breakdown field based on sintering times within the 6-1 group. This suggests that the sintering step is critical, but either the correct parameter has not been measured to correlate with the large breakdown field, or that one of the parameters in Table IV-10 would normally correlate better with E_b (e.g. grain diameter), but other factors (e.g. excessive delams) have ruined this correlation.

None of these T-case MLC's went into the switched state observed in the E-case MLC's even though they met two of the three geometric conditions which correlated to switching, i.e. the ratio of the transverse electrode pullback to cover thickness was less than 1.0 and the dielectric layer thickness was less than 30 microns. The absence of the switched state in these devices will be discussed later in this report.

E. Intermediate MLC's

After completion of all of the above testing, Task I-D of the research proposal called for manufacture of at least four sets of MLC's with variations based on the results discovered to

-89-

date. After evaluation of the T-case testing, the following MLC's were manufactured for Task I-D. These variations are divided into two groups based on the dimensions of the electrode artwork.

Variation A-1: This is the "standard" variation using the same artwork employed for the Phase I E-case MLC's, i.e.,

electrode active area = 325 x 325 mils^2

19 active layers (20 electrodes)

side margin = pullback = cover plate thickness = 30 mils

1.0 mil nominal layer thickness

30 min. sintering time at 1200°C

heating rate of 3.3°C/min.

bisque firing before dicing

TWC Nb_2O_5

A-2: Same as A-1 except devices were green-diced

A-3: Same as A-1 except 240 min. sintering time

A-4: Same as A-1 except 60 mil cover plate thickness

A-5: Same as A-1 except a heating rate of 20°C/min. This variation was originally not scheduled, but was included when a few devices were accidentally fired at a much faster heating rate.

B-1: Used a new artwork for the electrode active area, but also changed the number of layers to keep the total active area the same as A-1.

electrode active area = 265 x 265 mils^2

29 active layers (30 electrodes)

side margin = pullback = 60 mils

cover plate = 30 mils

1.0 mil nominal layer thickness

heating rate of 3.3°C/min.

green diced

B-2: Same as B-1 except side margins = 30 mils

B-3: Same as B-1 except pullback = 30 mils

C-1: Same as B-1 but with a different tape lot (explained below in the section on processing parameters)

Most of the "A" variations were chosen to check on parameters which had been found previously to cause differences in the breakdown voltages. The "B" variations plus the "A-4" variation were chosen not only for the same reason, but to test the geometry correlations for state-switching.

The processing information below was reported by ATC. All of the E-case parts made for Task I-D were made from two new tape lots. The first lot, 7-E-CPN17-001, was significantly different from previous lots in that increased precalcine and post calcine milling was performed to radically decrease the particle size. For instance this latter batch had an area of 3.45 m^2/gm compared to ~2.2-2.4 m^2/gm for previous batches. This preparation should have reduced settling and enhanced sinterability. However, no new sinterability studies were conducted after this time. The caster temperature was decreased and the binder level was increased to compensate for the increased surface area. The dispersing agent was changed from one containing sodium to a very high purity organic.

The second lot, 7-E-CPN17-002, was identical to the first except for the binder formulation. All previous lots had excess plasticizer removed prior to cutting the tape for electrode printing. Lot 002 was cast without the excess plasticizer. Also, due to a mistake, lot 002 had ~10% more binder than lot 001.

Although the processing details reported above presented a picture that implied the processing procedure was known and controlled, in fact later events showed that this was not the

case. Up to this point, one technician at ATC had processed most of the MLC's himself and the variations in processing parameters which he introduced and recognized and those which he did not recognize contribute to the absence of consistent correlations in some (but not all) parameters. This problem will be discussed later in section IV-F.

Variations A-1 through A-5 were made from tape lot 001 shortly after the lot was made in the spring of 1987. After the new artwork was received in the early fall of 1987, initial sets of variations B-1 through B-3 were made. These proved to have severe delaminations which were probably due to drying and aging of the tape batch; moisture content in May was 0.78% compared to 0.32% in November.

The small amount of remaining tape from lot 001 was put in a moisture chamber overnight and a few devices were made following the specifications for variation B-1 and this variation was named C-1. A new tape lot (002) was then made and used for variations B-1 through B-3. All four of these variations had small delams consistent with the A variations. These defects are discussed more below. The C-1 variation, which was identical to B-1 except for the tape lot, allowed a direct comparison between tape lots with no other variations involved. The remainder of the lot 002 tape was stored in a humidity chamber.

All of the A, B, and C variation devices from Task I-D were taken to breakdown using the computer-controlled program and equipment described previously. Table IV-12 lists all the breakdown information for all the groups including the number of devices tested, the average E-field and standard deviations at which breakdown occurred along with the average stored energy densites and standard deviation at breakdown. There is also a column showing the derated stored energy, i.e., the energy density averaged over the entire MLC volume, not just over the active volume. It should be noted that no attempt has been made to maximize the derated energy density through minimization of the inactive volume, so the best comparison number is still the active volume energy density. Minimization of the inactive

volume is dependent upon possible geometry variations which will affect the "switching" effect at high fields. This tradeoff will be discussed further below. No "switching" has been observed in any Phase II devices (T-case or E-case).

Destructive physical analysis was performed on selected devices from these groups. Different flaw types were enumerated and there seemed to be no correlation between these types and variations in breakdown fields. Flaw studies were performed on post-breakdown devices. It would have been preferable to perform these studies on separate MLC's, but the manufacturer did not provide enough MLC's to give statistically meaningful results for both types of testing separately, so it was necessary to double up and use some devices for both testing.

The porosities were no greater than ~1.5% in volume and the amount of "second phase" ranged from 0.6% to 1.05%, which was higher than the amount of second phase in the groups which switched in Phase I. This second phase is unidentified as to composition, but may play a role in the switching phenomenon. Finally, insulation resistance measurements on Task I-D parts were lower than those made on T-case parts from tape 6-E-001 and there is no explanation at present for these lower values.

As seen in Table IV-12, none of the geometry variations (B-1, B-2, B-3, C-1, and A-4) showed differences in E_b which could be correlated with geometry. Instead, the differences among these groups correlate well with differences in tape lot processing as described above.

None of the A variations were significantly different from each other except for A-3 (240 min sintering time) which had a significantly lower breakdown voltage compared to the others. This finding is consistent with previous results. Interestingly, the green-diced MLC's (A-2) were no worse and maybe slightly better than bisque-diced MLC's in contrast to the findings for T-case parts. However, this variation was included because ATC had changed its dicing equipment and techniques since the T-case parts had been made, and because in ATC's experience, the flaws introduced by dicing could change because of device size alone.

TABLE IV-12 Breakdown Fields and Stored Energy Densities
of Task I-D MLC's

Group	No. Tested	Breakdown Field (kV/cm)	Stand. Dev. (kV/cm)	Active Vol. Stored Energy (J/cm^3)	Stan. Dev. (J/cm^3)	Derated Stored Energy (J/cm^3)
A-1	16	433.3	91.4	2.04	.48	0.3427
A-2	22	447.5	79.9	2.22	.48	0.3729
A-3	16	299.9	27.3	1.42	.14	0.2385
A-4	16	415.4	94.1	1.87	.49	0.1795
A-5	10	425.9	66.3	1.94	.34	0.3259
B-1	27	284.0	23.8	1.17	.11	0.1627
B-2	20	284.5	17.5	1.17	.08	0.1962
B-3	17	271.3	12.9	1.11	.06	0.1862
C-1	23	313.5	56.3	1.41	.26	0.1993

In general, there was a trend toward improvement in breakdown voltage in these devices compared to previous devices. As a group, the T-case 6-1 MLC's were still the best, but the average for these latter groups was higher than previously.

F. Production of the Final Set of MLC's

Task IV of the Research Proposal called for production of two lots of MLC's, one lot of E-case size and one lot of larger devices. The larger size lot was eliminated because it is likely that each size MLC has breakdown characteristics which are closely tied to processing parameters and each significant dimension change may introduce problems which were not predictable from previous measurements on smaller devices. Changes in size sometimes require changes in processing parameters because of effects which are size dependent. An example of such an effect is the time needed for escape of evolving gases at the electrode/dielectric interface. In general, the larger the area of the interface, the harder it is for these gases to escape. For these reasons it was decided to make all of the final set of MLC's in an E-case size.

As mentioned above, the technician at ATC who had been making CPN-17 MLC's left their employment. As ATC attempted to produce the final set of MLC's for this project using the notes of the former technician, they found the parts had severe delaminations. It became apparent to them quickly that the manufacturing process was not under control, i.e. there were a number of steps in the batching process which were being done either haphazardly or incorrectly. Over the summer of 1988, ATC personnel were able to work out all of the problems, eliminate the delamination problem and produce quantities of E-case MLC's that were the best quality of this size yet produced. At the end of the program, ATC sent a report giving details of the manufacturing process. This report is presented in whole as Appendix B. In addition, at the end of this Appendix are additional comments which were ATC's answers to specific

questions from CPI about the report.

The final set of MLC's were manufactured by ATC in two batches derived from two different tape lots made at ATC. The first batch (8E-CPN17-002) consisted of 42 devices fired at 1200°C for 30 minutes and 9 devices fired at 1200°C for 240 minutes. The second batch (8E-CPN17-003) consisted of 61 devices all fired at 1200°C for 30 minutes.

The 30 minute soak time had previously yielded the best results and the 240 minute soak time yielded the worst, even though the peak capacitance of the device went up at the longer soak time. This result is not well understood since longer soak times should lead to lower porosity (and higher capacitance) and therefore to fewer macroflaws. It is possible that the increased grain growth accompanying the longer soak time lowers the breakdown threshold either directly by lowering the intrinsic breakdown voltage, or indirectly by lowering the strength of the material. In the most recent batch a few devices were soaked at the longer time in order to confirm that this anomalous behavior still occurs.

Tables IV-13 to IV-15 below give the average dielectric constant at 77 K, the average E-field at breakdown and the average stored energy at breakdown along with standard deviations for each of these quantities for each of the three groups of devices. The averages are based on the measured quantities for only five devices from each group and are therefore meaningful only when there are large differences among groups. In the -003 group, there was one device which broke down at an anomalously low value, and is probably an oddity not representative of the group. Therefore, in Tables IV-14 and IV-15, two averages are presented for this group, one with and one without the anomalous device.

Examining the above tables, tape lot -002 behaved as expected in that an increased soak time increased the dielectric constant by about 10% and decreased by about 40% the breakdown field and stored energy at breakdown. The devices with a 30 min. soak time were as good as any E-case devices that previously been

examined in terms of stored energy, and they were somewhat higher in dielectric constant compared to recent groups of E-case MLC's, which had $\epsilon \sim 5500-6000$.

Table IV-13

Average dielectric constants at 77K and E=0 and standard deviations

Group	$\langle\epsilon\rangle$	σ
8E-CPN17-002(30 min)	6386	245
8E-CPN17-002(240 min)	6951	139
8E-CPN17-003	8864	302

Table IV-14

Average E-field at breakdown and standard deviation

Group	$\langle E\rangle$ kV/cm	σ	
8E-CPN17-002(30 min)	302	39	
8E-CPN17-002(240 min)	180	62	
8E-CPN17-003	237	68	(5 devices)
8E-CPN17-003	269	27	(4 devices)

Table IV-15

Average energy at breakdown and standard deviation

Group	$\langle\Delta F\rangle$ J/cm^3	σ	
8E-CPN17-002(30 min)	1.29	.16	
8E-CPN17-002(240 min)	.74	.26	
8E-CPN17-003	1.05	.30	(5 devices)
8E-CPN17-003	1.19	.13	(4 devices)

Interestingly, the device with the largest stored energy in this group was also the device with the smallest ϵ (1.58 J/cm^3 and 5950 respectively). Note that both of these values are about 2σ

above the respective means for this group.

Batch -003 was a surprise. The dielectric constant is larger than for any previous multilayers. Without the one anomalous device in this group, the stored energy was less than one standard deviation below the best group (-002 at 30 min), recalling however, that the statistics are limited by the small number of devices tested. Note that the average breakdown field is significantly below that of the best group, and the only reason that the average stored energy is high is because of the larger dielectric constant. The dielectric constant as a function of temperature is shown in Fig. IV-7 for a single MLC from each main group.

There is presently no definite explanation for these anomalies. Verbal communication with ATC indicates that the two batches were processed identically, from the same lot of source powders, except for the milling step before calcining. This was performed in two different machines in different types of jars, but for identical times. Unless there was another unidentified difference between the batches, this knowledge provides the first solid clue to differences in dielectric constant, i.e. differences in milling the batched source powders might be expected to affect the homogeneity and stoichimetry of small regions within the CPN-17 ceramic. In the future, samples may need to be prepared from jet-milled source powders in order to achieve minimum powder size and maximum homogeneity.

Obviously, the best of worlds would combine the large ϵ of batch -003 with the large breakdown field of batch -002 (30 min soak time). As stated above however, the relationship among these factors is not well understood. The best group is still the -002 group with an average stored energy of ~1.3 J/cm^3 = 21 J/in^3 and a breakdown field of ~ 300 kV/cm.

G. Duty Cycle Test Equipment Set-up

The equipment and computer program set-up for the duty cycle testing phase of the capacitive energy storage contract serves
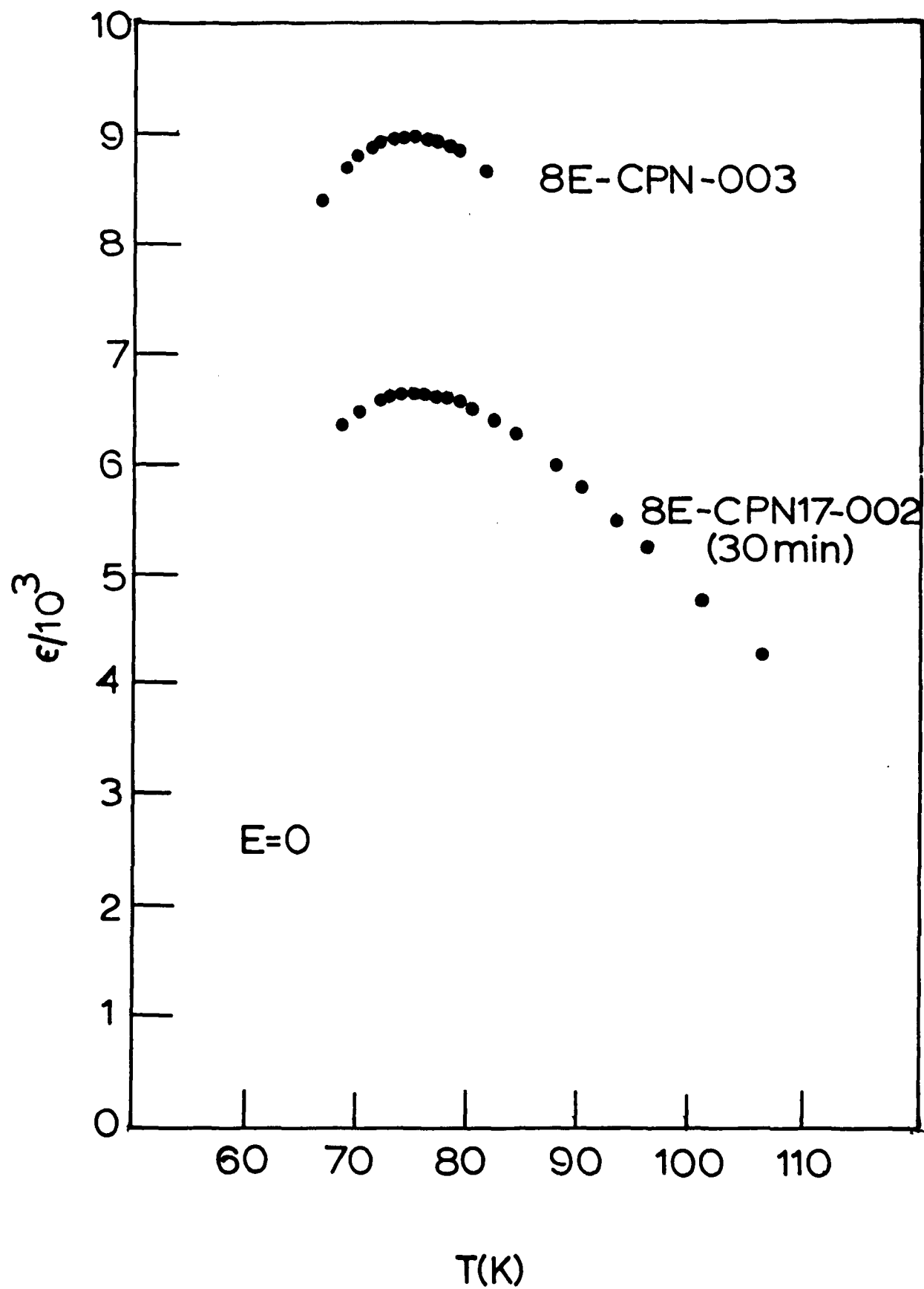
Figure IV-7 Dielectric Constant for CPN-17 MLC's of the
Final Test Group   -99-

two purposes. The first is to do extensive duty cycle testing of banks of capacitors produced during the program. The second purpose is to measure the energy put into charging the capacitor bank and the energy loss to the bath. From these measurements the mechanism for heat lost from the capacitor bank can be determined, whether it is heating upon charging, heat outflow upon discharge, or a combination of the two.

The capacitor charging/discharging system (Fig. IV-8) consists of a Bertan Associates Model 200-C488 IEEE-488 computer interfacing unit, a Bertan Associates Model 210-05R High Voltage Power Supply, a series of Clarostat variable resistors, and a Ross Engineering Company Model E-12-DT high voltage relay. The computer program sends an IEEE command to the interfacing unit which in turn relays the voltage requirement to the high voltage power supply via a remote control command. The series of resistors serves the purpose of protecting the charging system from accidental high current demand since the power supply current self-limits at 40 mA. For a charging voltage of 400 volts, the variable resistors are set at a minimum of $10^4 \Omega$ which means that the time constant for charging is ~ 0.3 sec ($10^4 \Omega$ x 10 capacitors x 3 μF/capacitor). At this point the high voltage relay is energized under computer control. The current flows from the power supply thru the series of adjustable resistors into the high voltage relay and on to the bank of capacitors (which is immersed in a dewar of liquid nitrogen) with a feedback line to the power supply. The voltage remains on even after the bank is charged, until the moment of discharge. When the bank is discharged, the computer sends a command to the Erbtec Model 200C IEEE interfacing system which controls the relay panel. A relay on the panel de-energizes the high voltage relay which shorts across the capacitor bank. The computer then sends an IEEE command to the Bertan IEEE interface (which controls the power supply) to set the voltage output back to zero. The charging system is kept in the discharge mode until the end of the duty cycle.

The charging system is only part of the overall system,

there is also the system monitoring equipment consists of three
Keithley Model 181 Digital Voltmeters (DVM), a Bertan Model
HVD-10 High Voltage Divider, two Hewlett Packard Model 62613
Power Supplies, a MKS Model 258B Mass Flowmeter, and several
Omega thermocouples.

The first DVM monitors the sample voltage through the high
voltage divider (Fig. IV-8). The high voltage divider has a
large input impedance and allows for the direct measurement of
the voltage across the bank of capacitors. The computer monitors
this DVM during the charging portion of the duty cycle to watch
for signs of sample breakdown, so that the system can
automatically shut down in case of such a failure.

The dewar that contains the sample probe is completely
sealed except for one exit portal for the nitrogen gas blowoff.
This blowoff hole is connected via a 10 ft hose to the mass
flowmeter. The length of the hose allows the gas to warm so it
is at room temperature. The mass flowmeter is powered by the two
HP power supplies. The second DVM reads the output from the
flowmeter. This is also monitored throughout the duty cycle by
the computer. The third DVM reads the voltage across a
thermocouple mounted with silicone rubber cement between two
consecutive capacitors in the bank of capacitors and this allows
the computer to watch for any temperature rise during duty cycle
testing. The entire system, charging and monitoring, is
completely and safely computer controlled.

The bank of capacitors consists of 10 capacitors wired in
parallel. The capacitors are supported between two slotted
blocks of nylon (Fig. IV-9). The capacitors are connected with
silver wire that has been attached with fired-on silver paste.
The free ends of the voltage wires are anchored to posts at
either ends of the slotted blocks. The voltage and DVM leads
from the top of the probe are also anchored to the posts running
through the sample holder. The connections on the outside of the
probe are high voltage BNC connectors, which safely insulate the
voltage leads coming from the power supply. The sample holder is
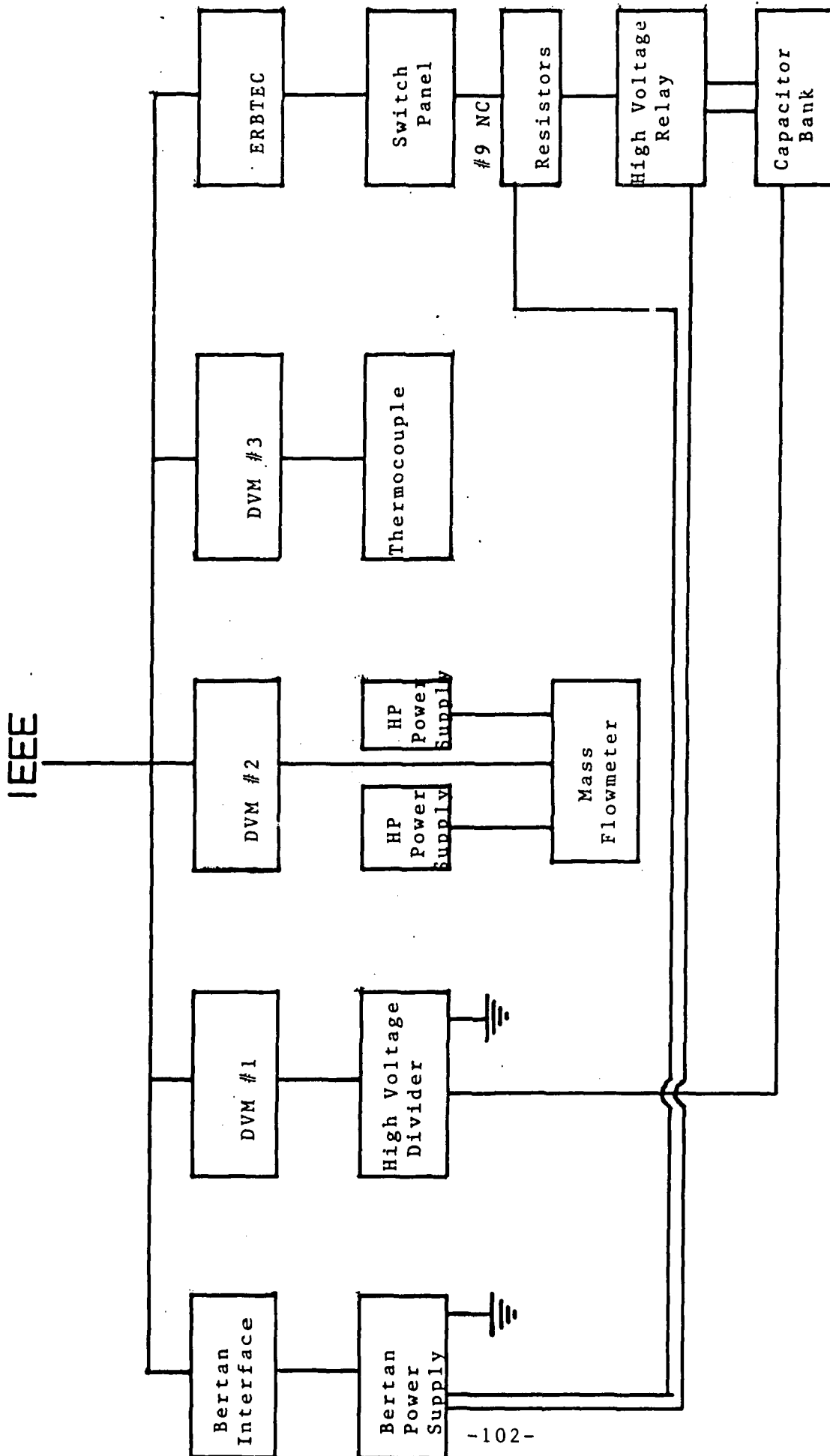attached to the bottom platform of the probe which allows for

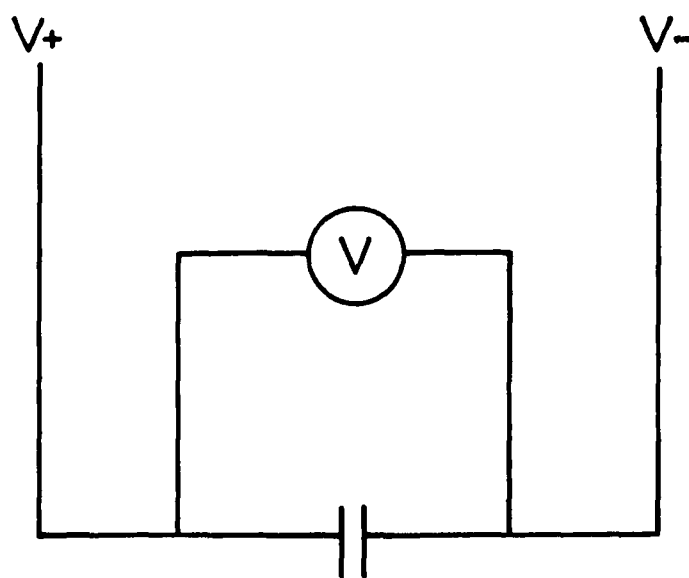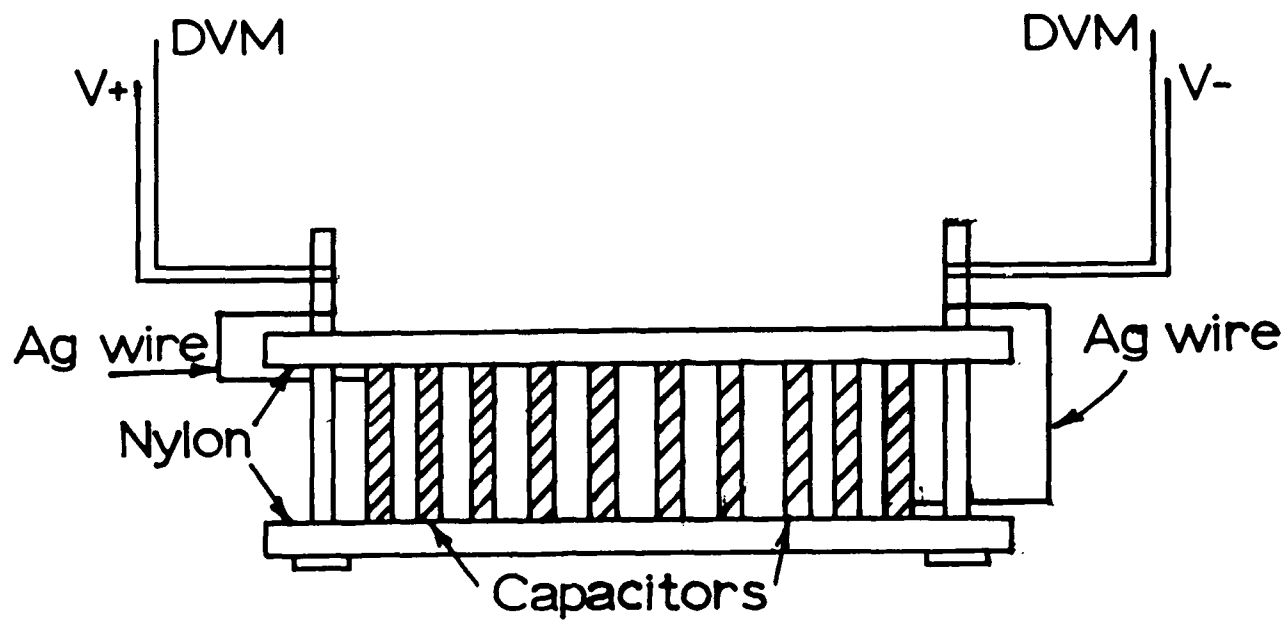Figure IV-8 Equipment Schematic for Duty-Cycle Testing

Figure IV-9 Capacitor Bank for Duty-Cycle Testing

free and unobstructed circulation of the liquid nitrogen about the capacitors. The lower platform is connected to the top platform of the probe with three small hollow rods. The main structure of the probe is constructed with stainless steel to impede the flow heat into the dewar. The voltage leads from the top of the probe to the sample stage are Belden 36 AWG magnet wire. These leads are insulated with Teflon sleeving and conduct very little heat. The probe was built to be sturdy and to restrict the flow of heat into the dewar. When the heat leak in is limited, very small temperature changes can be seen and related to the particular time in the duty cycle during which they occurred. In order to further insulate the system from the surroundings, a second dewar was placed around the first and filled with liquid nitrogen. With this system the effect of the surroundings is minimized and reasonably sensitive measurements can be taken.

The computer program makes it possible to do the duty cycle testing under a variety of conditions by changing the input parameters. The program can pe-form two different tests, duty cycle testing or background checking of the boil-off rate of the nitrogen surrounding the capacitor bank. Within the duty cycle testing the boil-off rate is also checked. There are several parameters that can be varied at the beginning of the program. They include: the charging voltage, the charging hold time, the discharging time, the number of duty cycles, and the interval at which the flow is measured. Only a few restrictions apply; the voltmeters cannot be read faster than one second intervals, and the length of the duty cycle must be a multiple of the flow measurement interval.

The output from the program is composed of very basic information which includes the cycle number, the voltage across the capacitor bank, the mass-flow out of the dewar, the thermocouple voltage, and the temperature change, at the capacitors, from the previous cycle. The output can be eliminated for a long duty cycle test where outputs are not needed, except for keeping track of the number of successful

cycles.

All of the instruments used are either directly or indirectly computer controlled with IEEE commands. However, the IEEE lines do become corrupted occasionally and for this reason some special safety features have been built into the program. When a capacitor breaks down, the capacitor bank is unable to charge completely. In the program, if the bank does not fully charge for three successive duty cycles the system is automatically shut down. The reason for waiting through three cycles is that the DVM's sometimes take incorrect readings which could lead to an unnecessary shutdown if only one cycle was used to judge the stability of the system. The other safety feature is a keyboard interrupt, which shuts down the system after receiving a command from the keyboard. This signals the program to short across the capacitor bank and reduce the voltage to zero and to stop the program. The result of these safety features is a program that can be left running unattended indefinitely except for the occasional attention to the level of liquid nitrogen in the dewar. The capacitors must remain immersed in liquid nitrogen for the duration of any single test run. The system is otherwise entirely self sufficient.

H. Duty-Cycle Testing

With the equipment described in the last section and 10 MLC's randomly selected from the -003 group described in Section IV-F above, duty-cycle testing could be completed. There were two main questions that needed answering at the beginning of these tests. First, how much energy was lost per MLC per cycle under various conditions and what was the source of that loss. Second, how well would the capacitors hold up under multiple charge-discharge duty-cycles, and were there limits to the number of cycles due to either charging voltage or cycle time.

With all the equipment assembled, initial tests were made to determine the background boil-off rate of the liquid nitrogen with no power input to the capacitors. Tests were run under a

variety of conditions of waiting times after LN_2 fill and liquid
level difference and it was found that within reasonable limits
the boil-off rate was variable and it could not especially be
predicted, but it did stay constant or change very slowly over
reasonably long (~ 1 hr) times. Therefore when duty-cycle tests
were run to measure energy loss, background losses were always
measured for ~ 20 min before and after the test. Furthermore,
there was a short-term (~ seconds) noise level associated with
the boiling itself, not with the instruments. This noise level
determined the lower limit of detectable energy losses in the
capacitor bank. This noise level was equivalent to detecting a
change of .039 J/sec in the boil-off rate. For 10 MLC's at one
duty-cycle every six seconds, the noise level was equivalent to
an energy loss of 0.023 J/MLC/cycle. In practice an energy loss
of ~ .01 J/MLC/cycle could be detected using averaging over
several closely spaced readings of this flow rate.

In direct contradiction to expectations, no change in
boil-off rate was detected under any duty-cycle conditions,
including the harshest condition of a charging time of three
seconds, and a discharge time of three seconds with a charging
voltage of 400 volts applied to the capacitor bank in each
duty-cycle. Furthermore, there was no detectable long-term
temperature rise within the MLC's under any duty-cycle
conditions. Electrocaloric heating and cooling was detected
during each duty cycle and will be discussed below. Temperature
rises within the MLC's were detected by sealing a thermocouple
between two MLC's in the capacitor with silicon caulking material
so that the thermocouple was totally isolated from direct contact
with the liquid nitrogen bath (refer to Fig. IV-9).

These results mean that under the testing conditions
employed here, there is no limit to the number of cycles due to
internal heating of the capacitors as predicted as a possibility
from the heat-flow studies of Section III above. The combination
of low energy losses and efficient heat flow from the ends and
sides of the MLC's preve t any temperature increases. In the
future, if the breakdown fields can be increased further, the

thermal analysis of Section III will again be relevant and valuable.

The temperature rise due to the electrocaloric effect was easily identified because of its reversible nature, i.e. the temperature change was in opposite directions during the charge/discharge cycle. All other sources of heat within an MLC are irreversible. The temperature change after charging was averaged over 40-50 cycles as a function of charging field. The results are plotted in Fig. IV-10 and compared to a typical temperature change from electrocaloric measurements on thermally isolated single devices (solid line on Fig. IV-10). The temperature change is significantly smaller for the duty-cycle MLC's than for the isolated MLC because the thermometer was located on one face of the MLC and heat could therefore escape through the other five sides. This comparison again demonstrates how comparatively easy it is for heat to be removed from an MLC.

An approximate measurement of the leakage current through the capacitors was made by measuring the voltage as a function of time. The equipment as shown in Fig. IV-8 had to be modified slightly because during normal duty-cycle testing, the charged voltage supply remained connected to the capacitor bank during the full charging part of the cycle and the MLC's were shorted during the discharge. The connections were changed in Fig. IV-8 so that during the discharge, the leads to the bank were opened and therefore the voltage drop across the capacitors was due to leakage currents.

The voltage could not be read continuously during this discharge cycle since the voltmeter circuit would also provide a discharge path. The highest input impedance instrument available was the high voltage divider in Fig. IV-8, with an input impedance of $\sim 10^8$ Ω. Furthermore, measurements were complicated because the voltage drop is not a simple exponential with a single time constant $\tau = RC$. Here R is the internal resistance of an MLC and C is its capacitance, but C is a strong function of the applied voltage. In the analysis below, however, the voltage drop is measured over short enough times, so that the capacitance
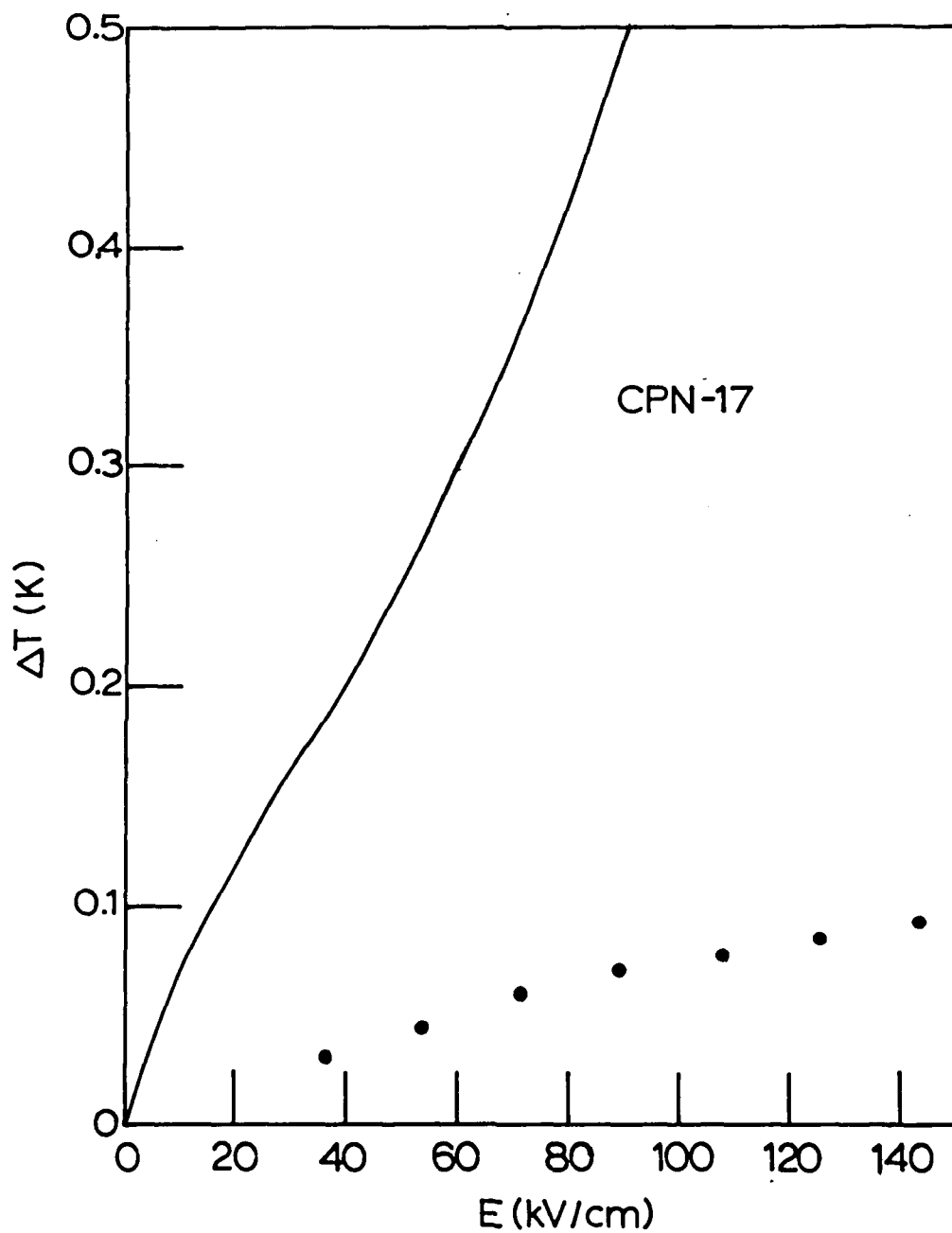
Figure IV-10   Electrocaloric Heating of CPN17 MLC's in LN_2 bath (solid circles) compared to the electrocaloric heating of an isolated MLC.

-108-

does not change too radically, and the analysis assumes a single τ a constant C.

The entire experiment was done under computer control, where the bank was first charged to a known voltage for 10 sec and the voltage across the MLC's was measured at the end of this period. Then both the high voltage relay was opened and the DVM was removed from the circuit. After a time period of 100, 200 or 500 seconds, the DVM was again added to the circuit and the voltage across the bank was measured. The initial charging voltage was 100 volts and the lowest voltage (after 500 sec) was ~ 50 volts. The average value for the time constant was $\tau \cong 1.1 \times 10^3$ sec. Using an average value of C = 0.64 μF per device in the voltage range 50-100 volts, this implies that the internal resistance at 77 K per device is $R = 1.8 \times 10^9$ Ω, which is reasonably large.

The final duty-cycle tests were made on the same bank of 10 MLC's used in the above experiments and were made to measure the ruggedness of the capacitors over a large number of cycles. A duty-cycle was selected of a three-second charge to 400 volts and then a discharge by shorting the bank with a wait of three seconds before repeating the cycle. This duty-cycle was repeated over 100,000 cycles on the same capacitor bank. There were two failures during this test run. After about 8000 cycles completed during an overnight run, one MLC in the bank had undergone a breakdown. However the IEEE line from the computer to the test equipment was "hung-up" and had altered the measurement conditions. The capacitor was replaced and the tests continued.

A second failure occurred in a single MLC after ~ 30,000 cycles when after an electrical storm, the IEEE line again hung up and it was observed immediately before the breakdown that the computer was charging the bank excessively. Thus one, and maybe both breakdowns occurred because of an equipment failure, not related to the duty-cycle itself. After this second occurrence, the MLC was replaced, and there were no more incidents.

The entire set of 100,000 cycles was made in 14 separate runs over ~ 6 weeks and ranging in length from about 4000 cycles to 14,000 cycles. During this time, the MLC's were cycled from

room temperature to 77 K seven times. The large number of cycles successfully completed here appears to be an remarkably large number. For instance the Bendix Corporation[7] developed some room temperature, high-voltage, barium-titanate capacitors under a DOE contract which were required to survive only 100 discharges. The large number of duty-cycles and the multiple temperature cycles indicates that the material and construction is rugged and that breakdowns were not occurring because of accumulated stresses within the MLC's.

I. Dielectric Constant and Thermal Contraction Measurements

The primary emphasis in this program has been to improve the breakdown voltage of the ceramic MLC's. The dielectric constant at 77 K is known to be ~ 8000 and cannot be significantly improved, although as seen above, it can be degraded during processing. However, an understanding of the behavior of the dielectric constant as a function of both temperature and electric field is important to an overall understanding of the process of energy storage in these ceramic MLC's. Additionally, dielectric constant measurements can provide clues as to the underlying mechanisms which give CPN17 an unusually large dielectric constant.

At each stage of the Phase II contract, dielectric measurements have been made on selected MLC's to measure $\epsilon(E)$ at 77 K and $\epsilon(T,E)$ over a wider temperature range. Not all of the data will be presented below; instead enough data will be given to illustrate both the similarities and differences among measurements throughout the program.

Some of the data has been presented previously. In particular, Fig. II-2 shows the E-field dependence of a typical multilayer of CPN-17. Although $\epsilon(E=0)$ varies from group-to-group the general behavior remains identical for all groups. As can be seen in Fig. II-2, ϵ falls rapidly as the E-field is first increased, but then begins to plateau at higher fields. Between E=0 and E=200 kV/cm, ϵ drops by about a factor of 30, but

decreases much more slowly above this field. Although not shown in Fig. II-2, there is little or no hysteresis between increasing and decreasing fields.

The data in Fig. II-2 can be analyzed according to the Ginzburg-Landau formalism for the free energy:

$$A = A_0 + \frac{1}{2}\chi P^2 + \frac{1}{4}\xi P^4 + \frac{1}{6}\zeta P^6 + \ldots \qquad \text{IV-1}$$

where

$$E = \partial A/\partial P \text{ and } 4\pi/\varepsilon = \partial^2 A/\partial P^2$$

Solving for $1/\varepsilon$ in Eq. IV-1 and then performing a least-squares fit to data similar to the data in Fig. II-2 for MLC's from different groups of Phase II devices showed that χ_0 and ξ were reasonably uniform for all devices. For instance, for an MLC from variation A-2 of the "Intermediate MLC's", $\chi_0 = 2.21 \times 10^{-3}$ and $\xi = 7.39 \times 10^{-13}$. It was found that χ_0 would vary by ~ 50% mainly due to differences in $\varepsilon(E=0)$, but that ξ varied by no more than ± 10%. When $\xi > 0$ (as it was in all cases in this program), this indicates the ferroelectric transition is second order. There was a wider variation in ζ (a typical value was ~ 1.0 x 10^{-22}) and although the order of magnitude was constant, the sign of ζ could be either positive or negative. However, it was never clear that ε was measured to high enough values of E to accurately resolve this term (a typical upper limit was 200 kV/cm).

Data for $\varepsilon(T,T)$ over a wide range of temperatures at various constant values of E are shown in Figs. IV-11 thru IV-13. In each case, data for approximately the same six field levels are shown. At E=0, the data all show a ferroelectric transition near 77 K and ε decreases as the field is increased. There are differences among the three sets of data which may ultimately be related to the presence or absence of the switched-state, but at present there are no obvious correlations.

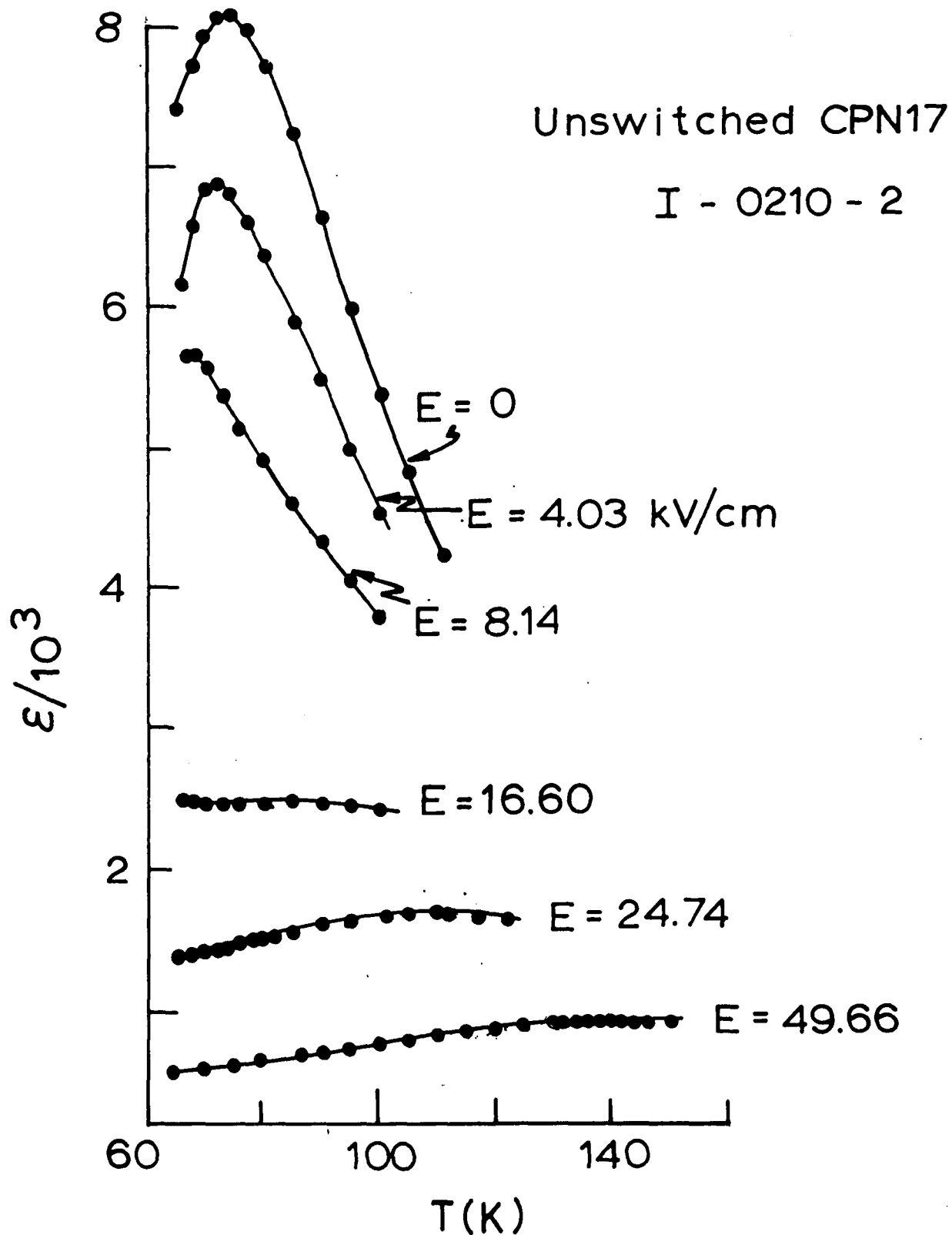Examining the differences among the three sets of data, note

Figure IV-11 $\epsilon(E,T)$ for CPN17 MLC, Group I of the Preliminary
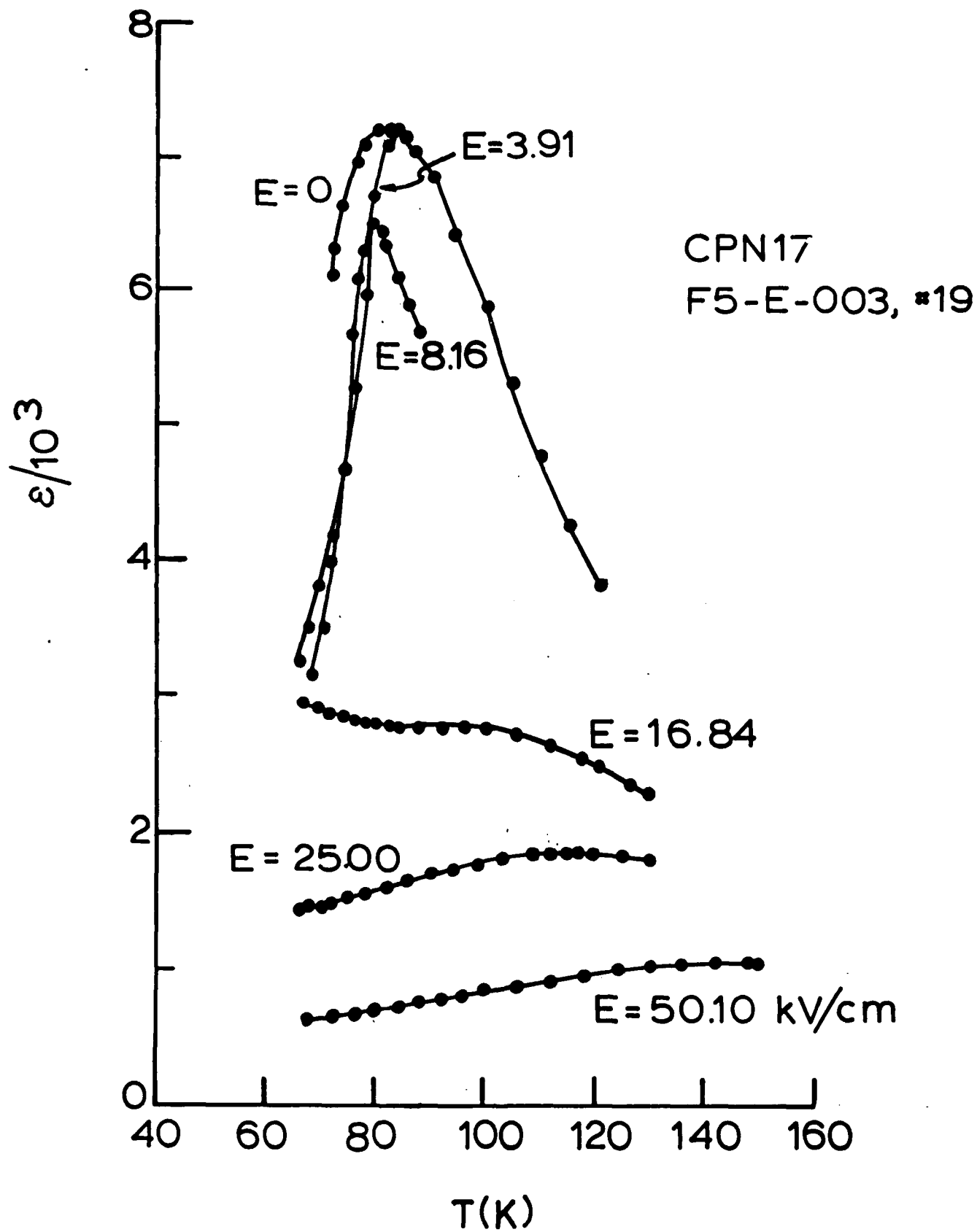E-case MLC's

Figure IV-12 $\epsilon(E,T)$ for CPN17 MLC from Group 5-003 of the Initial T-case MLC's
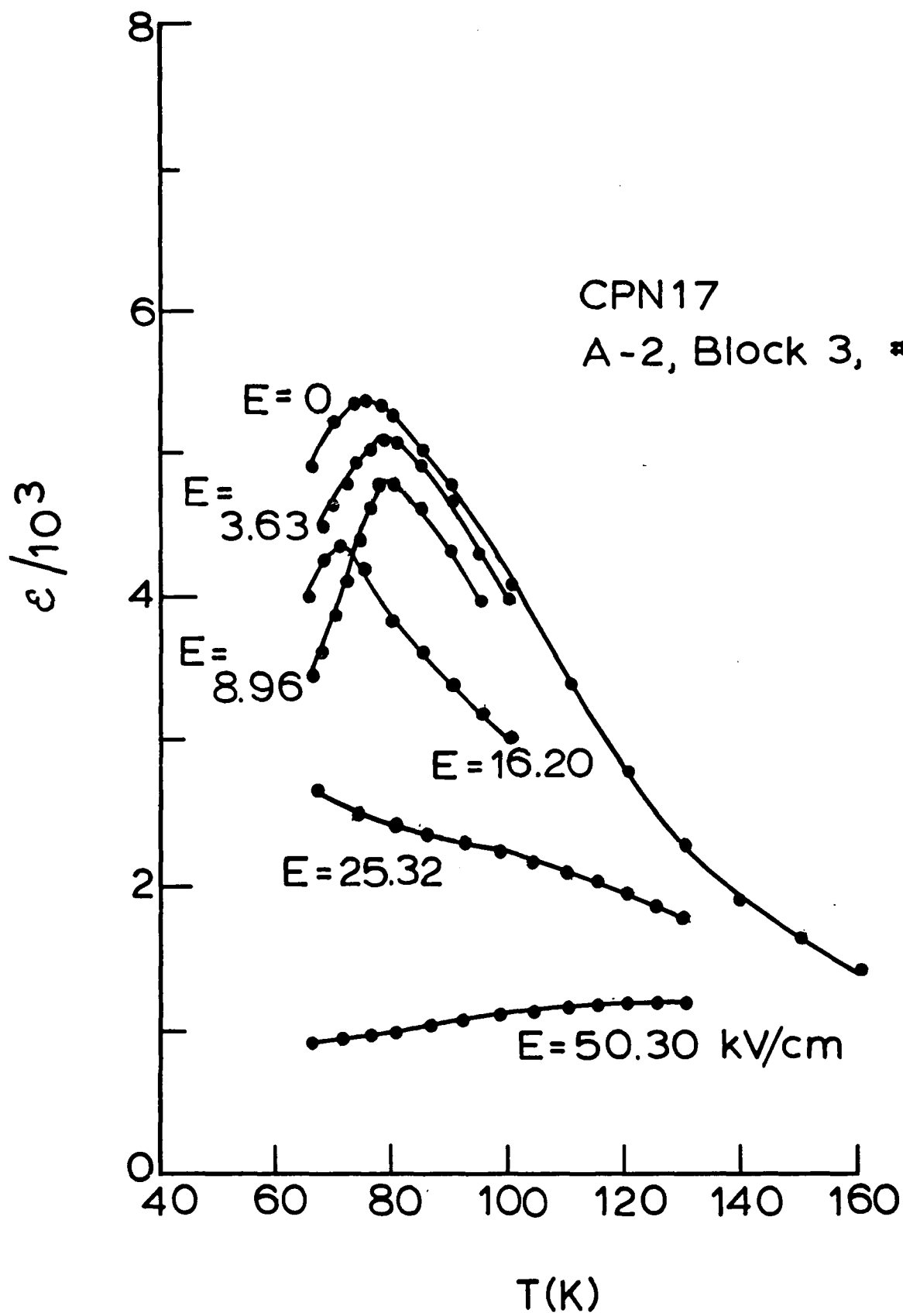
Figure IV-13   ε(E,T) for CPN17 MLC from Group A-2 of the Intermediate
E-case MLC's

-114-

the different behavior at E ≅ 16 kV/cm. Note also that in two
sets, (Figs. IV-12, IV-13) the peak first shifts up and then down
at low increasing fields, while in Fig. IV-11, at low fields the
peak shifts monotonically down. At large fields, the situation
is even more complicated because there are two peaks associated
with each large field (although one peak is often off the graph
at low temperatures).

These data can be explained if there are two mechanisms in
the material which give rise to ferroelectric transitions and
each of the two act differently in applied E-fields. One
component's peak would shift upward in temperature as E increase,
while the other would shift downward, thus creating a double peak
at high fields. Slight differences from device to device would
dictate the movement of the peak at low fields. Although it is
not clear that this explanation can also account for the
switched-state, the data does show that the material is complex
and is not a simple ferroelectric.

Further evidence for two ferroelectric mechanisms comes from
studies of related materials (differing by the amount of Pb
doping) which show two different peaks in ϵ at E=0. Also studies
of $\epsilon(T)$ for E=0 at large values of T indicate the possibility of
complex Curie-Weiss behavior which might well be explained by the
sum of two Curie-Weiss components.

As the final data presented in this program, Fig. IV-14
shows the thermal contraction of a CPN-17 multilayer between room
temperature contraction of a CPN-17 multilayer between room
temperature and 77 K compared to pure copper. This contraction
data would be useful in system design and in evaluating stresses
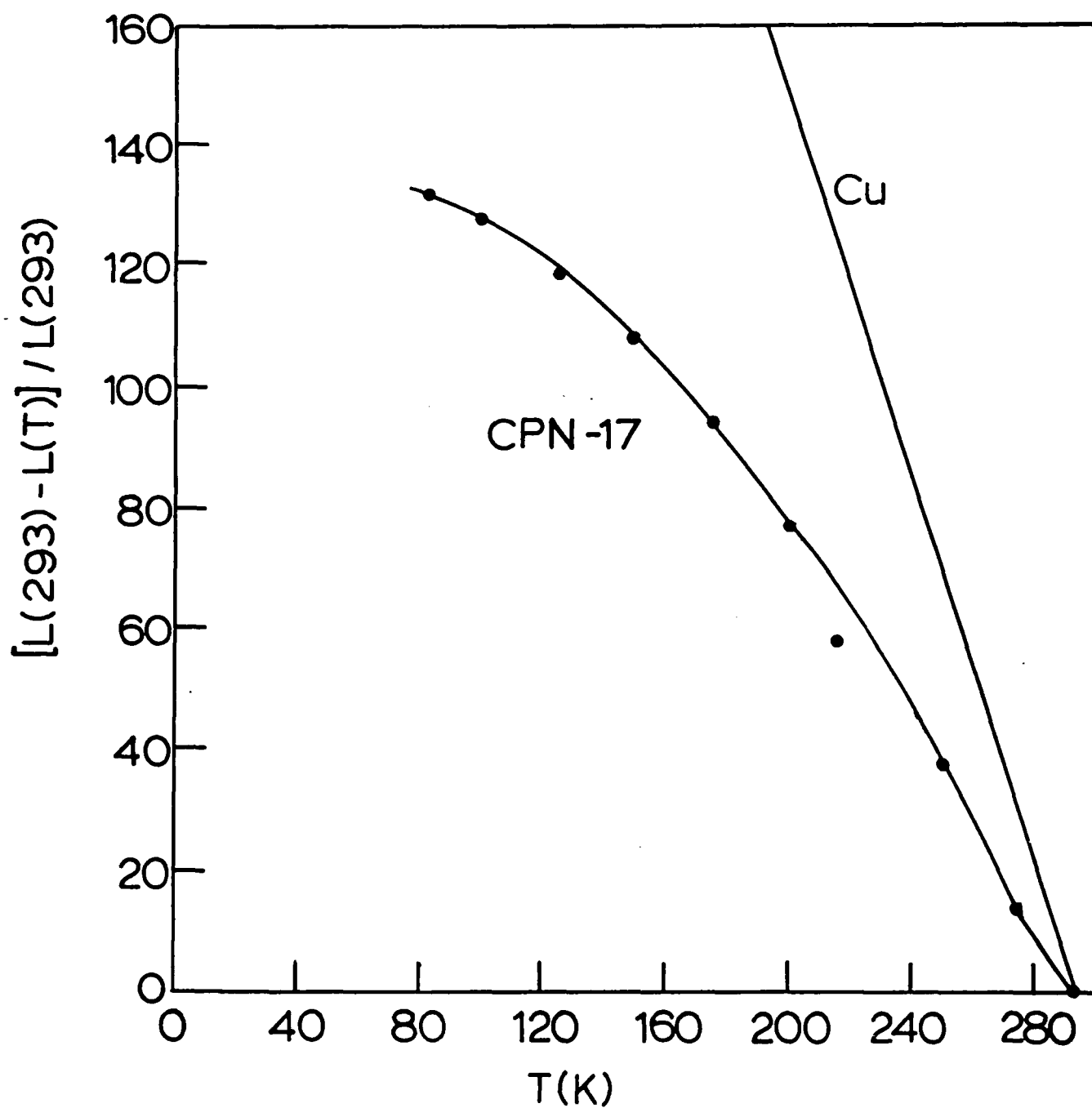within the material.

Figure IV-14   Thermal Contraction of a CPN17 MLC compared to ETP copper
(from NBS Monograph 29, "Thermal Expansion of Technical
Solids at Low Temperatures")

V. Conclusions and Discussions

In the final part of this program, large numbers of uniform, rugged CPN-17 MLC's were produced with stored energy densities at breakdown of ~ 1.3 J/cm^3. An individual MLC from earlier in the program had a measured stored energy density of 5.8 J/cm^3 and the group which included this individual MLC had an average stored energy density of 2.9 J/cm^3. A bank of ten MLC's withstood over 10^5 duty-cycles of a slow (3 sec) charge to 400 V and then a rapid discharge, with the total duty cycle being 6 sec long. There were no energy losses within the limits of measurement during these duty-cycle tests and there was therefore no average temperature rise within the MLC's which would limit the number of duty cycles.

The upper limit to the breakdown field has not yet been reached, nor is there an indication of how much higher it might be. The "switched-state" has not been reproduced, although there remain intriguing clues as to its origin. Not all the processing parameters which affect the breakdown field have been identified or properly quantified. The role of other factors such as internal stresses and geometry variations in affecting the breakdown are also not yet understood because processing and the effects of processing (e.g. porosity, macroflaws, etc.) appear to dominate the breakdown process for the MLC's made so far.

The two paragraphs above summarize both the successes and the unanswered questions at the end of this Phase II program. These conclusions will be discussed in further detail below and areas for future research and improvements will be identified.

In retrospect, it was not realized how dominant the processing parameters would be in affecting breakdown fields and therefore the manufacturer did not always keep adequate records until late in the program. Thus the importance of some parameters was recognized only in hindsight and some are still problematic. The simplest way to discuss these parameters is to outline the processing procedure and discuss each step as it occurs.

Different source powders for Nb_2O_5, the dominant component, were considered early in the program and the results were inconsistent in that some high purity powders produced effects normally related to impurities. A source powder for Nb_2O_5 from TWC was finally chosen because it produced consistently good results. Different source powders for the other components were not investigated. It is not clear if impurities have any effect, let alone which impurities might be important. It is also highly likely that particle size distribution (PSD) of the source powders is very important because it affects the small-scale homogeneity (stoichiometry) of the final product. No data is available on this particle size distribution.

Also for reasons of homogeneity, the mixing and milling steps before calcining may be critical, as is the PSD after this stage of the process. These conclusions were reached from several indirect clues, and have not been tested directly in a controlled manner.

The calcining schedule was established early at 900°C for 8 hours. Although there was little or no measurable weight loss at this schedule, the effects of a longer time at a lower temperature were not explored. It is possible that a different schedule may affect the local homogeneity and stoichimetry and therefore affect the growth of the second phase and acicular grains during the sintering step.

The batch formulation, slurry preparation and tape-casting procedures were all recognized as possible important processes to control, and the final procedure outlined in Appendix B seems to give satisfactory results. Certainly it is important to control PSD after calcining, settling within the slurry, slurry viscosity, and moisture content of the dried tape among others, because these items will ultimately affect the optimum sintering schedule. The specific binder system used probably does not affect results as long as the sintering schedule is tailored to the particular binder system.

At one point, there was concern that the platinum ink used to print electrodes was causing a catalytic reaction during

binder burnout which in turn was producing excessive delaminations from evolved gases. This problem was solved not by changing inks, but by changing the binder burn-out schedule.

At another point in the program, dicing technique variations produced large differences in breakdown field when it was clearly shown that green-dicing was inferior to bisque-dicing. However, the manufacturer later improved the dicing techniques and green-dicing was then better. In each case, the better result occurred when the dicing did the least damage to each device. If the damage is excessive, dicing in the bisque state will do the least harm. With better techniques, small damage in the green-state dicing will be "healed" during the sintering process.

The sintering schedule was investigated in both Phase I and early in Phase II, primarily by firing pellets under different schedules and using fired density as the criterion on which to judge results. The minimum porosity of 1.5% was found in Task I-D E-case MLC's. Throughout the program, it was always found that shorter sintering times at temperature produced better results than longer times. While the result is clear, the reasons are not. On one hand, longer sintering times should reduce porosity and therefore should lead to increased breakdown strength. On the other hand, longer times promote larger grain growth and may affect stoichimetry because of Cd and Pb volatility. It is not clear what the relation is between these effects and breakdown field.

It is clear that the sintering schedule is probably not optimized with respect to increasing the breakdown strength, although the schedule used was probably as good as could be found given the resources available during this program. It is also clear that there are complex interrelationships among the factors mentioned above which affect stoichimetry, the porosity, the grain size, other macroflaws, and the sintering schedule. It is possible for instance, that a sintering schedule which minimizes porosity will not simultaneously maximize breakdown strength.

The magnitude of the dielectric constant of CPN-17 appears to be affected dramatically by these same interrelationships. It

was consistently found in the program that a lower value of ϵ at E=0 was better than a higher value.

A central conclusion to this study is that the interrelationships listed above are the immediate causes of the limitation which presently exists in the stored energy density. In order to improve the energy storage to the point where other factors come into play, it will be necessary to understand these interrelationships and control the processes better.

Geometry factors were extensively investigated in this program and some of these factors clearly affected the stored energy density while others clearly did not. One motivation for looking at geometry factors were the strong correlations between the switched-state and geometries discovered in early MLC groups. Although no further switching was found, perhaps because it was swamped by other effects, the geometry correlations may still hold clues to the effect for future studies. Certainly the geometry variations which might have affected stresses in the MLC's (margin variations, cover plate thicknesses, and number of active layers) produced no differences in breakdown strength.

There were two geometry changes which did affect the results. The first was dielectric layer thickness where thinner layers were better, i.e. they had a higher breakdown E-field. In the future it would therefore be important to minimize the layer thickness consistent with not introducing fatal flows in the tape. Since the best MLC's in this program were made of tape $\sim$ .001" thick and this is about the limit of the tape-casting process, perhaps there would be other methods of making thin, multiple layers of CPN-17 which could be explored in the future.

The other geometry change which affected the results was the difference between T-case ($0.27 \times 0.3 \times 0.167$ cm^3) and E-case ($1.0 \times 1.0 \times 0.2$ cm^3) MLC's. The largest energy storage densities were achieved in the smaller T-case devices. While it is possible that this was a random result related to lack of proper controls in other processing parameters, it is also possible, for instance, that the binder burnout schedule was better suited to the T-case rather than the E-case.

The above results of the research to date clearly show that further advances in this technology will come from improved ceramic processing and will require a radical departure from state-of-the-art processing. Fortunately, such improved processing is now possible and embraces two complementary aspects:

1. The commercial availability of ultrafine monosized ceramic powders; and

2. The development of rate-controlled-sintering techniques that have the proven capability of producing ceramic microstructures of extremely high sintered densities with uniform size-distributions of the sintered grains.

Neither development by itself would be sufficient to produce the microstructure required to increase the energy storage density by increasing the dielectric breakdown strength. If small, mono-sized particles are improperly sintered, uncontrolled grain growth can occur leading to a large particle-size distribution. On the other hand, the rate-controlled-sintering techniques cannot produce a sintered grain-size-distribution that is finer or more uniform than the starting powder.

The implications here for energy storage are illustrated in Fig. IV-1 below which schematically represents a ceramic multi-layer capacitor, and it is important to realize that in this tapecasting technology the dielectric layer is quite thin, typically 0.003 cm. The exploded views in Fig. IV-1 show two different microstructures -- a coarse microstructure on the left, a fine microstructure on the right. Since grain boundaries form direct, easy paths for dielectric breakdown between the electrodes, it is clear that the fine microstructure on the right presents a multitude of tortuous breakdown paths whereas the microstructure on the left presents only a small number of easy paths. Moreover, in the case of the fine microstructure, if one grain boundary does fail, there are a large number of other boundaries in series with it that inhibit further breakdown. These qualititative arguments are widely accepted as the limiting reasons for dielectric breakdown in state-of-the-art ceramic

capacitors.

MULTILAYER
CERAMIC
CAPACITOR

ELECTRODE
GRAIN
BOUNDARY
DIELECTRIC
ELECTRODE

ELECTRODE
ELECTRODE
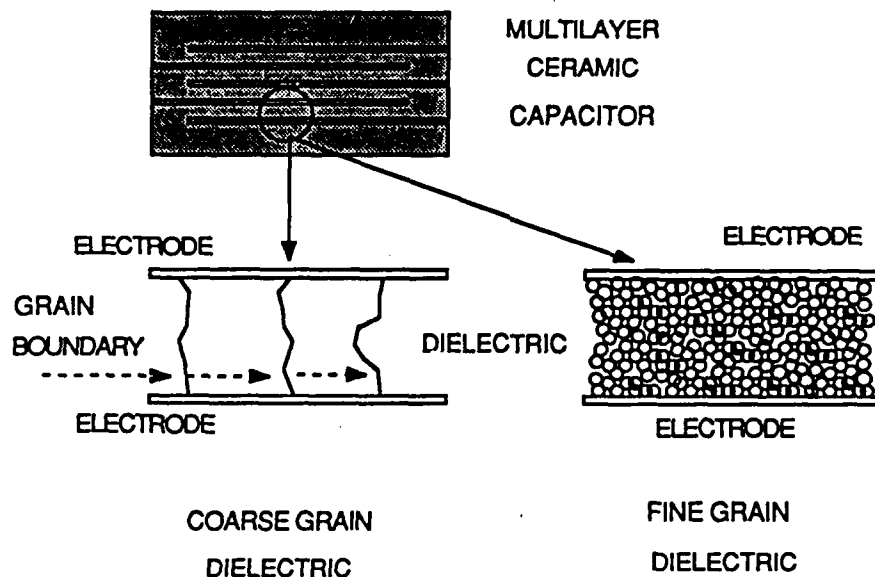
COARSE GRAIN
DIELECTRIC

FINE GRAIN
DIELECTRIC

Figure IV-1. Schematic drawing of a multilayer ceramic
capacitor, and the two exploded views show the microstructures of
a coarse grain dielectric (left) and a fine-grain dielectric
(right).

Even starting with ultrafine monosized powders, it is very
difficult to produce a uniform microstructure of fine-grain
material because large grains tend to grow at the expense of
small grains producing a large distribution of particle sizes.
The sintering of powders involve complex, interrelated mechan-
isms, and these mechanisms must occur in the proper sequence to
produce the desired microstructure. And this is precisely where
the new techniques of rate-controlled-sintering (RCS) can be
fruitfully employed.

The RCS technique is based on the fact that the rate of
heating can favor one sintering mechanism over another, and it is
therefore possible to control the complex sintering mechanisms
(i.e., the sequence in which they occur, their degree of comple-
tion completion, and their relative rates of occurrence) by

controlling the heating rates throughout the sintering cycle.

The RCS technique is a proven method for optimizing sintering mechanisms. The RCS instrument can specify and control the heating rate during sintering through closed-loop feedback control, and, in addition, it can measure the actual amount of sintering that is occurring at a given heating rate and temperature. By controlling the sintering rate throughout the temperature range over which sintering occurs, it is possible to control the sintering mechanisms occurring and thereby optimize the final properties of the ceramic.

As a final summary, the program was successful in its primary goal of improving the breakdown strength and energy storage density of CPN-17 MLC's. Furthermore, the program demonstrates that this material is capable of further improvements and has pointed the way toward making these improvements.

References

(1) K.N. Mathes and S.H. Minnich, Cryogenic Capacitor
Investigation, General Electric Co., Final Report S-67-1095, May,
1965.

(2) W.N. Lawless, Proc XIII International Congress of
Refrigeration, Washington, D.C. 1971, Vol. 1, p. 599.

(3) Phase I, AFOSR-SBIR Contract F49620-84-C-0089.

(4) W.N. Lawless, Phys Rev B14, 134(1976).

(5) A.F. Devonshire, Adv. in Phys. 3, 85(1954).

(6) W.N. Lawless, J. Phys. Chem. Solids 30, 1161 (1969).

(7) R.R. Honig, Report for Department of Energy contract
DE-A04-76-DP00613, March 1983.

Appendix A - Thermal Model of Heat Flow Within an MLC

In Section III of this report we documented thermal conductivity measurements, both longitudinal and transverse, in CPN17 MLC's (70-100 K). Analyses of these measured data yielded a separation of the thermal conductances of the ceramic and the metal electrodes, and both platinum and ternary electrodes were examined. Two central results were found: (1) Thermal conductances parallel to the electrode sheets are significantly larger than the conductance of the ceramic alone; and (2) The thermal conductance of the platinum electrodes is 2-3 times larger than that of the ternary electrodes (same thickness).

These results lead directly to the thermal modeling of the energy-storage MLC under charge/discharge conditions, and the purpose of this Appendix is to establish the thermal model, to present closed-form solutions of the nonlinear heat-flow problem, and to establish a code for solving this problem numerically. Section III of this Final Report presents numerical solutions under various, practical conditions.

THERMAL MODEL

We begin with the exploded view of an MLC shown in Fig. A-1 and consisting of blocks 1,2, and 3. The entire MLC is constructed from the remaining three quadrants. Block 1 is the heart of the MLC where all ceramic layers (except for the cover plates) are electroded. Block 2 is the "pullback" region where approximately half of the electrodes are exposed for termination [e.g., all the (+) or all the (-) electrodes]. Finally, block 3 is the "margin" ceramic containing no electrodes. All electrocaloric phenomena (e.g., polarization heating, depolarization cooling, joule heating, etc.) occur in block 1. The thermal problem reduces to considering how the electrocaloric heating/cooling in block 1 communicates to the surrounding liquid nitrogen bath. Specifically, how long does it take for the center of block 1 (i.e., the geometric center) to decay back to the bath temperature following an electrocaloric event?
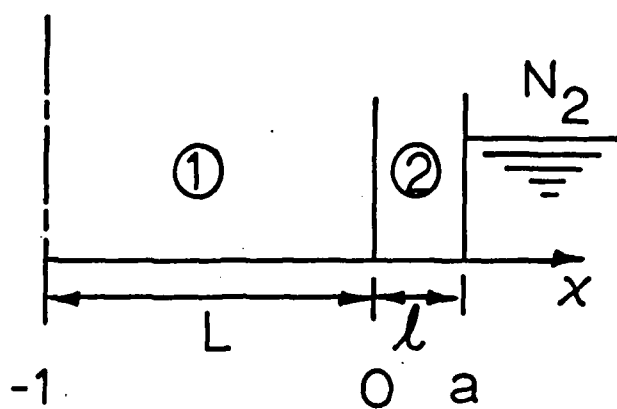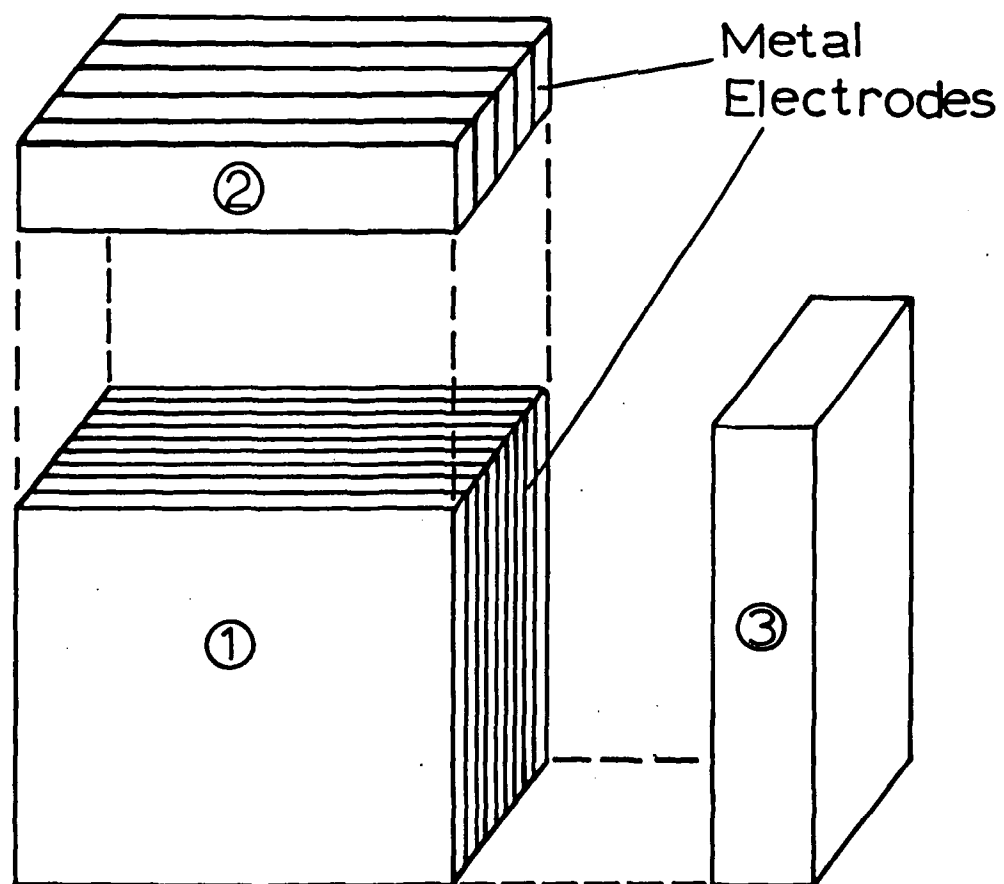
Figure A-1

In the ideal thermodynamic case, one is faced with solving the three-dimensional, heat-flow problem in blocks 1,2, and 3; symmetry considerations dictate that only one of the four quadrants need be considered. This is a monumental undertaking; however, certain simplifications are suggested.

First, since the metal electrodes have such large thermal conductances compared to the ceramic, only the electroded blocks 1 and 2 need be considered, to a first approximation.

Second, this approximation is improved considerably by practical considerations. Namely, it is anticipated that the termination face of block 2 in Fig. A-1 will be bonded to a copper or aluminum busbar, whereas all the remaining faces of the MLC are immersed in liquid nitrogen. The point here is that at relatively modest heat-flux levels, nucleate boiling may occur at these faces, which then thermally isolates these MLC faces. Thus, even if the ceramic material had the dominant thermal conductance (which it doesn't), nucleate boiling would constrain the major heat flow along the electroded blocks 1 and 2 into the termination busbars.

Therefore, the heat-flow problem justifiably reduces to the convenient, one-dimensional case through blocks 1 and 2, as shown at the bottom of Fig. A-1. Specifically, we consider the case of block 1 of half-length L bonded to block 2 of width ℓ where the surface of block 2 is maintained at the liquid nitrogen reservoir temperature.

FOURIER SERIES TRANSFORMATION

The basis for the following derivation of the Fourier series transformation is that this is a case of transient heat transfer in a one dimensional model. See Fig. A-1 for a representation of an example of a multi-layer capacitor.

The following equations represent the temperatures in regions 1 and 2 respectively. These are the equations that must ultimately be solved for a temperature profile across the MLC.

$$\frac{1}{\alpha_1} \frac{\partial T_1'}{\partial t} = \frac{\partial^2 T_1'}{\partial x'^2} + \frac{U'''}{K_1} \qquad (A-1)$$

$$\frac{1}{\alpha_2} \frac{\partial T_2'}{\partial t} = \frac{\partial^2 T_2'}{\partial x'^2} \qquad (A-2)$$

From this point the derivation is carried out in transformed coordinates to make the derivation more clear and easier to follow. The following are the transformations used:

$$T_1 = \frac{T_1' - T_\infty'}{U''' L^2 / K_1} \quad ; \quad T_1' = T_1 \left(U''' \frac{L^2}{K_1} \right) + T_\infty \quad ; \quad \partial^2 T_1' = \frac{U''' L^2}{K_1} \partial^2 T_1$$

$$T_2 = \frac{T_2' - T_\infty'}{U''' L^2 / K_1} \quad ; \quad T_2' = T_2 \left(U''' \frac{L^2}{K_1} \right) + T_\infty \quad ; \quad \partial^2 T_2' = \frac{U''' L^2}{K_1} \partial^2 T_2$$

$$t = \frac{t' \alpha_1}{L^2} \quad ; \quad t' \frac{t L^2}{\alpha_1} \quad ; \quad dt' = \frac{L^2}{\alpha_1} dt$$

$$X = \frac{X'}{L} \quad ; \quad X' = \frac{X}{L} \quad ; \quad dx'^2 = L^2 dx^2$$

$$\alpha_1 = \frac{K_1}{(\rho c)_1} \qquad \alpha_2 = \frac{K_2}{(\rho c)_2} \qquad \alpha = \frac{\alpha_2}{\alpha_1}$$

$$K = \frac{K_2}{K_1} \qquad \alpha = \sqrt{\frac{(\rho c)_2 K_2}{(\rho c)_1 K_1}} \qquad a = \frac{\ell}{L}$$

$$b = \sqrt{\frac{\alpha_1}{\alpha_2}} \frac{\ell}{L}$$

Substituting transformed coordinates back into Eq.(A-1) and
(A-2);

$$\frac{\partial T_1}{\partial t} = \frac{\partial^2 T_1}{\partial x^2} + 1 \tag{A-3}$$

$$\frac{1}{\alpha} \frac{\partial T_2}{\partial t} = \frac{\partial^2 T_2}{\partial x^2} \tag{A-4}$$

In order to solve these equations the following boundary
conditions are needed.

$$\frac{\partial T_1}{\partial x}(-1, t) = 0$$ — This is a center condition.

$$T(a, t) = 0$$ — At the outer edge (a), the temperature should remain constant at all times.

$$T_1(0, t) = T_2(0, t)$$ — The temperatures on either side of the interface between the two regions should be equal at all times.

$$\frac{\partial T}{\partial x}(0, t) = K \frac{\partial^2 T_2}{\partial x}(0, t)$$ — An interface boundary condition.

$$T_1(x, 0) = T_2(x, 0) = 0$$ — At time = 0 for any x, the temperature is uniform across the block.

At steady state, it is assumed that constant heating is
taking place across the block.

$$\frac{\partial^2 T_{1S}}{\partial x^2} + 1 = 0 \tag{A-5}$$ — At steady state, T_1 does not change with respect to time; this comes from Eq.(A-3).

$$\frac{d^2 T_{2S}}{dx^2} = 0 \tag{A-6}$$ — At steady state, T_2 does not change with respect to time; this comes from Eq.(A-4).

A-5

Integrating Eq.(A-5) with respect to distance x, we find

$$T_{1s} = \frac{-x^2}{2} + c_1 x + c_2$$

Applying the center condition $\frac{dT_{1s}}{dx}(-1) = 0$, we find $c_1 = -1$

$$T_{1s} = \frac{-x^2}{2} - x + c_2 \tag{A-7}$$

Integrating Eq.(A-6) with respect to distance, x

$$T_{2s} = c_3 x + c_4$$

Using the edge condition $T_{2s}(a) = 0 \therefore c_4 = -c_3 a$

$$T_{2s} = c_3 x - c_3 a = c_3 (x - a) \tag{A-8}$$

Using the interface boundary condition $T_1s(0) = T_2s(0)$

$$c_2 = -c_3 a$$

Substitution into (A-7) and (A-8) yields the following

$$T_{1s} = -\left(\frac{x^2}{2} + x + c_3 a\right) \tag{A-9}$$

$$T_{2s} = c_3 (x - a) \tag{A-10}$$

Using the interface condition $\frac{dT_1s}{dx}(0) = K\frac{dT_{2s}}{dx}(0)$;

$$c_3 = \frac{-1}{K}$$

Substitution back into Eqs.(A-9) and (A-10) yields

$$T_{1s} = \frac{a}{K} - x - \frac{1}{2}x^2 \tag{A-11}$$

$$T_{2s} = \frac{1}{K}(a - x) \tag{A-12}$$

At steady state at the center of the block

$$T_{1s} = \frac{a}{K} - \frac{1}{2} .$$

This takes care of the steady state part of the differential equation used for modeling. Now the unsteady state portion must be solved.

The unsteady state solution requires the use of Laplace transforms to solve the differential equation.

$$F(p) = \int_0^\infty f(t) e^{-pt}\, dt$$

This is the Laplace in the time domain.

$$F(t) = \frac{1}{2\pi i} \int_{\gamma - i\infty}^{\gamma + i\infty} \overline{F}(p) e^{pT}\, dp$$

This is the inverse transform, known as the Bromwich integral (also known as the Fourier-Mellin integral). It is used for integration in a complex plane, and is evaluated by contour integration. This is used rather than the Fourier transform, because the tables of Fourier transform are inadequate for our situation.

Multiplying Eqs.(A-3) and (A-4) by this transform, we find the following:

$$p\overline{T_1} = \frac{d^2 \overline{T_1}}{dx^2} + \frac{1}{p}\left(1 - e^{-p\tau}\right) \tag{A-13}$$

$$\frac{p}{\alpha}\overline{T_2} = \frac{d^2 \overline{T_2}}{dx^2} \tag{A-14}$$

Then taking the Laplace transform of the derivative of each equation.

$$\overline{T_1} = A \cosh \sqrt{p}\,(x+1) + \frac{1}{p^2}\left(1 - e^{-p\tau}\right) \tag{A-15}$$

$$\overline{T_2} = D \sinh \sqrt{\frac{p}{\alpha}}\,(x-a) \tag{A-16}$$

Using the interface boundary condition $\overline{T_1}(0) = \overline{T_2}(0)$

$$A \cosh \sqrt{p} + \frac{1}{p^2}\left(1 - e^{-p\tau}\right) = -D \sinh \sqrt{p}\,b \tag{A-17}$$

Taking the derivative we find

$$A \sinh \sqrt{\rho} - D \sigma \cosh \sqrt{\rho} \, b = 0 \qquad \text{(A-18)}$$

From this equation we can find A and D by substitution into the original equation (A-17)

$$A = \frac{-1}{\rho^2} \frac{(1-e^{-\rho\gamma}) \, \sigma \cosh \sqrt{\rho} \, b}{[\sinh \sqrt{\rho} \, \sinh \sqrt{\rho} \, b + \sigma \cosh \sqrt{\rho} \, b \, \cosh \sqrt{\rho}]} \qquad \text{(A-19)}$$

$$D = \frac{-1}{\rho^2} \frac{\sinh \sqrt{\rho} \, (1-e^{-\rho\gamma})}{[\sigma \cosh \sqrt{\rho} \, b \, \cosh \sqrt{\rho} + \sinh \sqrt{\rho} \, b \, \sinh \sqrt{\rho}]} \qquad \text{(A-20)}$$

Substituting A into Eq.(A-15) and D in to Eq.(A-16)

$$T_1 = \frac{(1-e^{-\rho\gamma})}{\rho^2} \left[1 - \frac{\sigma \cosh \sqrt{\rho} \, b \, \cosh \sqrt{\rho} \, (x+1)}{\sinh \sqrt{\rho} \, \sinh \sqrt{\rho} \, b + \sigma \cosh \sqrt{\rho} \, b \, \cosh \sqrt{\rho}} \right] \qquad \text{(A-21)}$$

$$T_2 = \frac{-(1-e^{-\rho\gamma})}{\rho^2} \left[\frac{\sinh \sqrt{\rho} \, \sinh \sqrt{\frac{\rho}{\alpha}} \, (x-a)}{\sigma \cosh \sqrt{\rho} \, b \, \cosh \sqrt{\rho} + \sinh \sqrt{\rho} \, b \, \sinh \sqrt{\rho}} \right] \qquad \text{(A-22)}$$

Recast these equations using the following

$$F(\rho) = \frac{1}{\rho^2} \left[1 - \frac{\sigma \cosh \sqrt{\rho} \, h \, \cosh \sqrt{\rho} \, (x+1)}{[\sinh \sqrt{\rho} \, \sinh \sqrt{\rho} \, b + \sigma \cosh \sqrt{\rho} \, b \, \cosh \sqrt{\rho}]} \right]$$

$$T_1 = F(\rho) - F(\rho) e^{-\rho\gamma} \qquad \text{(A-23)}$$

$$G(\rho) = \frac{-\sinh \sqrt{\rho} \, \sinh \sqrt{\frac{\rho}{\alpha}} \, (x-a)}{\rho^2 [\sigma \cosh \sqrt{\rho} \, b \, \cosh \sqrt{\rho} + \sinh \sqrt{\rho} \, b \, \sinh \sqrt{\rho}]}$$

$$T_2 = G(\rho) - G(\rho) e^{-\rho\gamma} \qquad \text{(A-24)}$$

To solve the equations we need to find the poles of G(p) and F(p). Poles are in the denominator of the equation. These poles are at P = 0 and P = $-\beta m^2$ where the equations we need to find the poles of G(p) and F(p). Poles are in the denominator of the equation. These poles are at P = 0 and P = $-\beta m^2$ where βm's are roots of

$$\tan \beta m = \sigma \cot \beta m b \qquad \text{(A-25)}$$
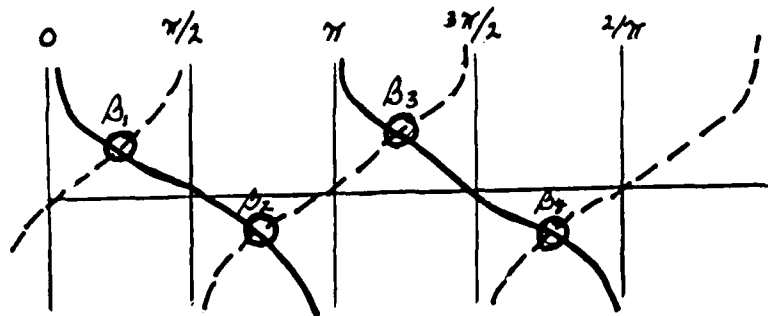
To complete the solution we need to find the residue at $\sqrt{p} = i\beta m$, the pole at $P = 0$ gives a steady state solution.

$$r = \frac{P(z_0)}{Q(z_0)}$$

$$\rho^2 \frac{d}{d\rho}\left\{ \sinh\sqrt{p}\, \sinh\sqrt{p}b + \sigma\cosh\sqrt{p}\,b\cosh\sqrt{p} \right\} =$$

$$\frac{\beta m^3}{2}\left[(\sigma+b)\sin\beta m\cosh\beta mb + (\sigma b+1)\sin\beta mb\cos\beta m\right]$$

Using this for $t<\tau$ and combining Eqs.(A-11),(A-12),(A-21), and (A-22), we find

$$T_1(x,t) = \frac{a}{K} - x - \frac{1}{2}x^2 - 2\sum_{m=1}^{\infty} \frac{1}{\beta m^3}\, \frac{\sigma\cos\beta mb\,\cos(\beta m(x+1))\,e^{-\beta m^2 t}}{\left[(\sigma+b)\sin\beta m\cos\beta mb + (\sigma b+1)\sin\beta mb\cos\beta m\right]} \tag{A-26}$$

$$T_2(x,t) = \frac{1}{K}(a-x) - 2\sum_{m=1}^{\infty}\frac{1}{\beta m^3}\,\frac{\sin\beta m\,\sin\beta m(b-\frac{x}{a})e^{-\beta m^2 t}}{\left[(\sigma+b)\sin\beta m\cos\beta mb + (\sigma b+1)\sin\beta mb\cos\beta m\right]} \tag{A-27}$$

The summation term comes from the definition

$$F(t) = \sum(\text{residues included for } R(s) < 8).$$
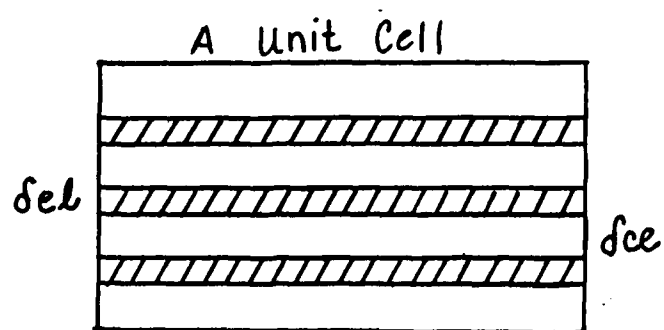
At $t > \tau$ the factors $e^{-p\tau}F(p)$ and $e^{-p\tau}G(p)$ have to be subtracted out since they have no contribution.

$$T_1(t) = 2\sum\frac{1}{\beta m^3}\frac{\sigma\cos\beta mb\cos(\beta m(x+1))e^{-\beta m^2 t}(e^{\beta m^2\tau}-1)}{\left[(\sigma+b)\sin\beta m\cos\beta mb + (\sigma b+1)\sin\beta mb\cos\beta m\right]} \tag{A-28}$$

$$T_2(t) = 2\sum\frac{1}{\beta m^3}\frac{\sin\beta m\,\sin\beta m(b-\frac{x}{a})\,e^{-\beta m^2}+(e^{\beta m^2\tau}-1)}{\left[(\sigma+b)\sin\beta m\cos\beta mb + (\sigma b+1)\sin\beta mb\cos\beta m\right]} \tag{A-29}$$

Calculation of Thermal Properties

The following is the origin of the thermal properties used in the Fourier transform derivation:

$$A \quad Unit \quad Cell$$

$$K = K_{el} \frac{\delta el}{\delta el + \delta ce} + K_{ce} \frac{\delta ce}{\delta el + \delta ce}$$

$$\rho c = (\rho c)_{el} \frac{\delta el}{\delta el + \delta ce} + (\rho c)_{ce} \frac{\delta ce}{\delta el + \delta ce}$$

$$\alpha = \frac{K}{\rho c}$$

$$U''' = \frac{U'''_{el} \delta el}{\delta el + \delta ce}$$

$$U'''_{el} = power \ density$$

Method of Solution

The computer code utilizes the above derivation to mathematically model a MLC for a given set of conditions. To generate the Beta eigenvalues table, Eq.(A-25) is solved iteratively for the number of terms desired. There are two sets of equations for use in finding the temperature at nodes within regions 1 and 2 of the MLC. For a time less than the length of the pulse, Eq.(A-26) is used for region 1 and Eq.(A-27) is used for region 2. For a time greater than the length of the pulse, Eq.(A-28) is used for region 1 and Eq.(A-29) is used for region 2. These equations are solved iteratively using the Beta eigenvalue table, and the temperature for nodes within the MLC are output. The code for the MLC modeling program is attached below.

THERMAL CONDUCTIVITIES

Referring to Fig. A-2, our thermal model of an MLC consists of two blocks: Block #1 containing N_1 metal electrodes and Block #2 containing N_2 electrodes. Correspondingly, the blocks have thermal conductivities K_1 and K_2, respectively, and these conductivities enter Eqs.(A-1)-(A-4) as α_1 and α_2. In this section we will develop explicit expressions for K_1 and K_2.

Since the electrodes and the ceramic material form <u>parallel</u> conduction paths in both blocks, the thermal conductances <u>add</u>, so that

Figure A-2. Thermal model of an MLC.

$$K_1 Wd = K_c Wd + K_e t_e N_1 W$$
$$K_2 Wd = K_c Wd + K_e t_e N_2 W \tag{A-30}$$

using the dimensions given in Fig. A-2. Here the subscripts "c" and "e" refer to the ceramic and electrode, respectively, and t_e is the electrode thickness. For a large number of electrodes,
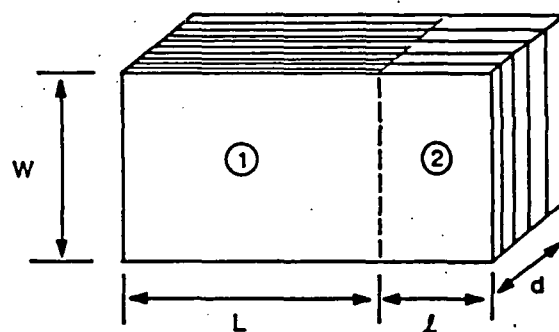
$N_2 = \frac{1}{2}N_1$, and Eqs.(A-30) become

$$K_1 = K_c + K_e t_e (N_1/d)$$
$$K_2 = K_c + \frac{1}{2}K_e t_e (N_1/d).$$
(A-31)

Finally we note that N_1/d is the number of electrodes per cm in block #1, and $N_1/d = 1/t_c$ where t_c is ceramic layer thickness (i.e., dielectric thickness). Therefore, we have the convenient result that

$$K_1 = K_c + K_e (t_e/t_c)$$
$$K_2 = K_c + \frac{1}{2}K_e (t_e/t_c).$$
(A-32)

In conclusion, we have established here the thermal model of an MLC including the computer code, and future reports will be devoted to numerical solutions.

Appendix B: Final CPN-17 Manufacturing Process Procedure

The following report was received from ATC late in December 1988 and gives details of the manufacturing process for the final MLC's used for the duty-cycle testing. There are additional comments after the report which expand and explain certain items in more detail. These comments are based on replies to written questions from CPI to ATC.

CPN-17 MANUFACTURING PROCESS PROCEDURE

I. SAFETY PRECAUTIONS

CPN-17 and its components possess certain characteristics which could be hazardous if proper steps are not taken.

A. EQUIPMENT

1. Unimaster dust control unit.

B. PERSONAL PROTECTION

1. Safety glasses
2. Rubber gloves
3. Dust respirator
4. Full protective suit
5. Bonnet
6. Shoe covers
7. Plastic gloves
8. Lab coat

C. PROCEDURE

1. Full safety gear is to be put on prior to beginning CPN-17 processing and must be worn during calcining and batch formulation.

2. Dust respirator and plastic gloves must be worn along with lab coat during processing from casting to binder burn out.

3. Loose powders are to be handled in dust control hood only.

II. MATERIAL PREPARATION

A. EQUIPMENT

1. Premier dispersator
2. Sweco grinding mill (M-18) w/zirconia grinding media
3. Blue-M gravity oven
4. PDH box kiln
5. Kadymill vacuum mixer
6. Scale
7. Brookfield viscometer
8. Sedigraph 5000D
9. Monosorb (Quantachrome)
10. Computrac Max 50
11. Casting table
12. Blue-M oven, MP-206F-1
13. Blue-M oven
14. Light-box

B. **MATERIALS**
1. Cadmium oxide
2. Lead oxide
3. Niobium oxide
4. Deionized water
5. Dispersant (Tamol)
6. Defoamer (Surfynol SE)
7. Plastic scoops
8. Plastic spatulas
9. Pyrex baking dishes 9" x 13"
10. Alumina crucibles w/lids, I.D.- 9 3/4" x 4" x 2 1/2"
11. Screen
12. Mortar and pestle
13. Pyrex glass beakers, 600 ml
14. Tin cups
15. Plastic buckets
16. Casting bucket (stainless steel)
17. Sethco filter (15 micron)

C. **CALCINING PROCESS**
The CPM-17 powder is derived by the calcination of Cadmium Oxide, Lead Oxide and Niobium Oxide powders.

1. Powders and water are weighed according to specific weight percentages of the formulation, and placed in individual plastic buckets with lids.

COMPONENT	WEIGHT %
CdO	38.416
PbO	13.677
NB_2O_5	47.908
H_2O	32.193

2. Water is weighed in a plastic bucket which will be used to mix slurry.

3. Bucket with water is placed on dispersator on medium speed.

4. Powders are added one at a time to water with plastic scoop. Powder is 'sprinkled' to eliminated clumping. Small amounts of dispersant added when necessary to ease mixing.

5. After all powders are added, mixture is run on dispersator for approximately 10 min.

6. Mixture is poured into Sweco and milled for 10 hours with recirculation.

7. Slurry is poured into Pyrex dishes and dried in Blue-M ovens for 6-8 hours at 80°C.

8. Dried slurry is crushed into powder using mortar and pestle and sifted through screen.

9. Powder is packed into saggers and covered.

10. Calcine for 8 hours at 900°C in PDH kiln.

11. CPN-17 powder is crushed and sifted into plastic storage bucket and covered.

D. BATCH FORMULATION
    1. CPN-17 powder, D.I. water, and Tamol dispersant are weighed according to formulation weight percentages.

COMPONENT	WEIGHT %
CPN-17	65.0
Tamol	0.056
H_2O	35.0

2. Mix water and dispersant on dispersator for approximately 5 minutes at medium speed.

3. Slowly sprinkle CPN-17 into water with scoop. Dispersator speed may need to be increased to allow even mixing.

4. After all powder is added, mixture is run on dispersator for approximately 10 minutes.

5. Mixture is poured into Sweco and milled for 20 hours with a recirculation rate of 1.5.

6. Slurry is down-loaded into plastic buckets.

7. A 450 ml sample is drawn into a 600 ml beaker for viscosity, pH, and density tests. If μ = 3950-4300 cps procedure may continue. If not, additional dispersant and milling may be required.

8. Three small samples of approximately 10 grams are drawn into tin pans and dried in Blue-M oven for approximately 30 minutes. Dried slurry is used for solids content, surface area, and particle size analysis tests.

9. Bucket(s) of slurry are then weighed to determine exact amount of slurry.

10. Slurry is poured into Kadymill and deaired.

11. An aqueous compatible binder system is added to slurry in accordance with formulation to achieve a slip solids content of approximately 50%.

12. Run Kadymill 30 minutes.

13. Completely deair slip. Defoamer may be necessary.

14. Pump slip out of Kadymill into stainless steel casting bucket.

E. CASTING
1. Casting bucket with slip is mounted on mixing stand of casting table.

2. Slip flows by plastic tubing through filter onto stainless steel belt of table.

Operating conditions:

Belt speed - 6 fpm
Water Temp - 60°C
Air Temp - 65°C
Cast Thickness - 1.8 mils

3. Tape is cut into 6" x 8" sheets.

4. Tape moisture content is determined from a sample of tape.

F. TAPE PROCESSING
1. Each sheet of CPN-17 tape is inspected on a boxed-light apparatus for pinholes and foreign particles.

2. Sheets are placed on oven drying paper, and hung on drying racks.

3. Racks are placed in Blue-M oven and dried for 45 minutes at 140°C.

4. Tape is then stored in humidity chamber at 23°C, 65% R. H.

III. BLOCK MANUFACTURING

A. EQUIPMENT
1. Slitting machine
2. Screen printer: ETP P-400
3. Screen: 218-328 emulsion
4. Blue-M drying oven
5. Queens hydraulic press
6. Die set, 1.5"
7. Dake arbor press
8. L & R Transistor/Ultrasonic cleaner T-14

B. **MATERIALS**
1. CPN-17 tape sheets
2. Platinum electrode ink – AEP 2050
3. Ink cleaner (Varsol-1)
4. Stainless steel spatula (curved)
5. Brush
6. Foam print boards
7. 1,1,1 – Trichloroethane
8. Strathmore paper

C. **SLITTING**
1. Each sheet of CPN-17 is slit to specification size.

2. Slit squares are placed on strathmore paper and stored in humidity chamber.

D. **SCREEN PRINTING**
1. Sheets are printed automatically with electrode ink in 1 1/2" pattern.

2. Prints are placed on foam print boards and dried in Blue-M oven.

85°C	1.5 Hours
85-125°C	10 Minutes
125°C	2.0 Hours

E. **BLOCK DESIGN**
1. Laminated block design

Top covers	31
Bottom covers	30
Standard electrodes	19

   a. Slit squares are arranged in sets on the print boards. One group consists of 30 stacked sheets, the other 31 sheets. Each set makes up one block.

   b. Prints are arranged in groups of 19 squares each on print boards.

2. E-case block specifications

Case length	380 mils
Case width	380 mils
Electrode length	312 mils
Electrode width	312 mils
Side margin	34 mils
End margin	34 mils
Cover	31 mils
Active layers	19

F. LAMINATION
1. Bottom punch is inserted into die set approximately 1/4" below top of die.

2. One stack of bottom covers is loaded into the die set. Each of the 19 prints are loaded one at a time with print design facing in opposite direction every other print. Load one stack of top covers.

3. Insert top punch into die set.

4. Die set is placed in hydraulic press and laminated at a pressure and cycle appropriate to binder system.

5. Block is ejected from die set on Dake press.

IV. CAPACITOR MANUFACTURING

A. EQUIPMENT
1. Dicer
2. Blue-M oven, CW5580-F
3. CM furnace
4. Zicar type B Silicon Carbide oven

B. MATERIALS
1. Laminated blocks
2. Zirconia setters
3. MLC termination ink-Dupont 7095
4. Screen
5. Squeege

C. DICING
Blocks are diced green under the following conditions:

Blade size	-	15 mil
Speed	-	5,000 rpm
Feed rate	-	300 mil/sec
Initial cut	-	58 mils
Index distance	-	462.2 mils

D. BINDER BURNOUT
1. Diced blocks or chips are placed on setters cork-side up

2. Chip elements are processed in Blue-M oven

20°C – 500°C	68:00
500°C	0:20
500°C –20°C	2:37

3. Chips are removed from Blue-M and dust is removed

4. Chip elements are processed in CM furnace

20-800°C	6:30
800	0:35
800-20°C	2:36

5. Chips are removed from CM and cleaned in 1,1,1-Trichloroethane for 2 minutes in Ultrasonic.

6. Let dry.

E. SINTERING
1. Chips are placed in 1 1/2" platinum boat w/cover

2. Boat is placed in a cylindrical crucible and covered with CPN-17 powder. Crucible is covered

3. Process in Silicon carbide furnace

20-1200°C	6:00
1200°C	0:30
1200 - 20°C	4:00

F. TERMINATION
1. Furnace is pre-heated to 600°C.
2. Chips are terminated using thick film termination process.
3. Terminated chips or capacitors are placed in furnace for 10 minutes.

4. Capacitors are removed from oven and allowed to cool.
5. Electrical characteristics are tested.

The following comments are additions and explanations to the previous report.

1. The source materials are as follows:

CdO: J.T. Baker Lot #625331, Reagent Grade R-1234, 99.4% pure, amorphous

PbO: Hammond Lead Products Lot 1-19-34, Electronic Grade 100Y, >99% pure

Nb_2O_5: Teledyne-Wah Chang Lot #34, >99% pure

No particle size distribution information was available at ATC for these materials.

2. After calcining there was occasionally a discoloration of the alumina saggers indicating a reaction between the materials (either Pb or Cd) and the vessels. When the discoloration occurred, the material was discarded and not used in CPN-17 batch formulation.

3. The pre-calcined slurry had a surface area of 16.68 m^2/gm with the following particle size distribution.

54% < 1 μm	D25	D50	D75	D100
	0.56	0.93	1.55	26.0

4. The Tamol dispersant used in the calcining step was 901 which is an ammonium based salt.

5. The binder system used is an ATC exclusive binder and cannot be disclosed. Thus the binder burnout schedule and laminating temperature and pressure are also proprietary since they are dependent on the binder.

6. The termination ink was Dupont 7095, a pure silver, glass-fritted paste.